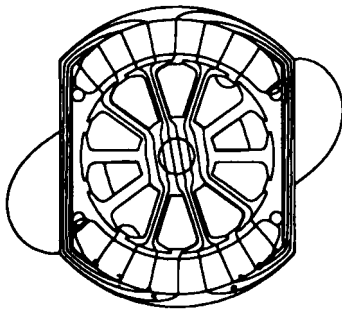
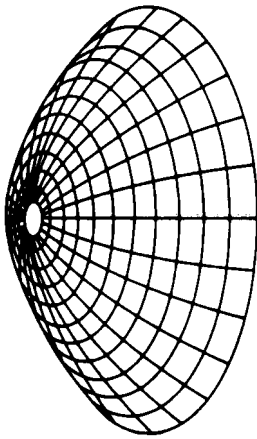


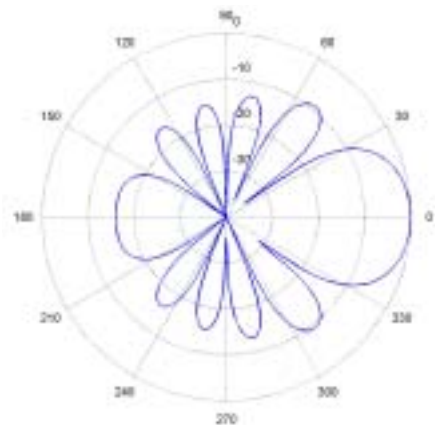
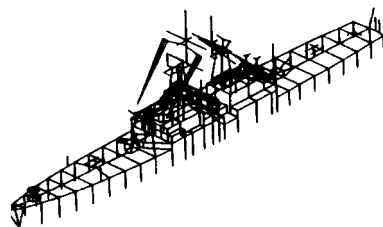
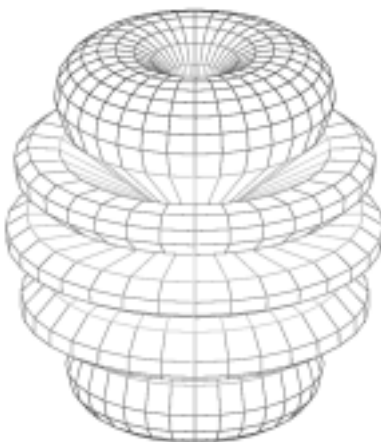
Applied Computational Electromagnetics Society Journal



Editor-in-Chief
Atef Z. Elsherbeni



November 2005
Vol. 20 No. 3
ISSN 1054-4887



GENERAL PURPOSE AND SCOPE: The Applied Computational Electromagnetics Society (*ACES*) Journal hereinafter known as the *ACES Journal* is devoted to the exchange of information in computational electromagnetics, to the advancement of the state-of-the art, and the promotion of related technical activities. A primary objective of the information exchange is the elimination of the need to “re-invent the wheel” to solve a previously-solved computational problem in electrical engineering, physics, or related fields of study. The technical activities promoted by this publication include code validation, performance analysis, and input/output standardization; code or technique optimization and error minimization; innovations in solution technique or in data input/output; identification of new applications for electromagnetics modeling codes and techniques; integration of computational electromagnetics techniques with new computer architectures; and correlation of computational parameters with physical mechanisms.

SUBMISSIONS: The *ACES Journal* welcomes original, previously unpublished papers, relating to applied computational electromagnetics. Typical papers will represent the computational electromagnetics aspects of research in electrical engineering, physics, or related disciplines. However, papers which represent research in applied computational electromagnetics itself are equally acceptable.

Manuscripts are to be submitted through the upload system of *ACES* web site <http://aces.ee.olemiss.edu> See “Information for Authors” on inside of back cover and at *ACES* web site. For additional information contact the Editor-in-Chief:

Dr. Atef Elsherbeni

Department of Electrical Engineering
The University of Mississippi
University, MS 386377 USA
Phone: 662-915-5382 Fax: 662-915-7231
Email: atef@olemiss.edu

SUBSCRIPTIONS: All members of the Applied Computational Electromagnetics Society who have paid their subscription fees are entitled to receive the *ACES Journal* with a minimum of three issues per calendar year and are entitled to download any published journal article available at <http://aces.ee.olemiss.edu>.

Back issues, when available, are \$15 each. Subscriptions to *ACES* are through the web site. Orders for back issues of the *ACES Journal* and changes of addresses should be sent directly to *ACES* Executive Officer:

Dr. Richard W. Adler

ECE Department, Code ECAB
Naval Postgraduate School
833 Dyer Road, Room 437
Monterey, CA 93943-5121 USA
Fax: 831-649-0300
Email: rwa@att.biz

Allow four week’s advance notice for change of address. Claims for missing issues will not be honored because of insufficient notice or address change or loss in mail unless the Executive Officer is notified within 60 days for USA and Canadian subscribers or 90 days for subscribers in other countries, from the last day of the month of publication. For information regarding reprints of individual papers or other materials, see “Information for Authors”.

LIABILITY. Neither *ACES*, nor the *ACES Journal* editors, are responsible for any consequence of misinformation or claims, express or implied, in any published material in an *ACES Journal* issue. This also applies to advertising, for which only camera-ready copies are accepted. Authors are responsible for information contained in their papers. If any material submitted for publication includes material that has already been published elsewhere, it is the author’s responsibility to obtain written permission to reproduce such material.

APPLIED COMPUTATIONAL ELECTROMAGNETICS SOCIETY JOURNAL

Editor-in-Chief
Atef Z. Elsherbeni

November 2005
Vol. 20 No. 3

ISSN 1054-4887

The ACES Journal is abstracted in INSPEC, in Engineering Index, and in DTIC.

The first, fourth, and sixth illustrations on the front cover have been obtained from the Department of Electrical Engineering at the University of Mississippi.

The third and fifth illustrations on the front cover have been obtained from Lawrence Livermore National Laboratory.

The second illustration on the front cover has been obtained from FLUX2D software, CEDRAT S.S. France, MAGSOFT Corporation, New York.

THE APPLIED COMPUTATIONAL ELECTROMAGNETICS SOCIETY

<http://aces.ee.olemiss.edu>

ACES JOURNAL EDITORS

EDITOR-IN-CHIEF/ACES/JOURNAL

Atef Elsherbeni

University of Mississippi, EE Dept.
University, MS 38677, USA

EDITORIAL ASSISTANT

Matthew J. Inman

University of Mississippi, EE Dept.
University, MS 38677, USA

EDITOR-IN-CHIEF, EMERITUS

David E. Stein

USAF Scientific Advisory Board
Washington, DC 20330, USA

ASSOCIATE EDITOR-IN-CHIEF

Alexander Yakovlev

University of Mississippi, EE Dept.
University, MS 38677, USA

EDITOR-IN-CHIEF, EMERITUS

Ducan C. Baker

EE Dept. U. of Pretoria
0002 Pretoria, South Africa

EDITOR-IN-CHIEF, EMERITUS

Allen Glisson

University of Mississippi, EE Dept.
University, MS 38677, USA

MANAGING EDITOR

Richard W. Adler

833 Dyer Rd, Rm 437 EC/AB
NPS, Monterey, CA 93943-5121, USA

EDITOR-IN-CHIEF, EMERITUS

Robert M. Bevensee

Box 812
Alamo, CA 94507-0516, USA

EDITOR-IN-CHIEF, EMERITUS

Ahmed Kishk

University of Mississippi, EE Dept.
University, MS 38677, USA

ACES JOURNAL ASSOCIATE EDITORS

Giandomenico Amendola

Universita' della Calabria
Rende , Italy

John Beggs

NASA Langley Research Center
Hampton, VA, USA

Malcolm Bibby

Gullwings
Weston, MA , US

John Brauer

Ansoft Corporation
Milwaukee, WI, USA

Magda El-Shenawee

University of Arkansas
Fayetteville AR, USA

Pat Foster

Microwave & Antenna Systems
Gt. Malvern, Worc. UK

Cynthia M. Furse

Utah State University
Logan UT, USA

Christian Hafner

Swiss Federal Inst. of Technology
Zurich, Switzerland

Michael Hamid

University of South Alabama,
Mobile, AL, USA

Andy Harrison

Radiance Technologies, Inc.
Huntsville, AL

Chun-Wen Paul Huang

Anadigics, Inc.
Warren, NJ, USA

Todd H. Hubing

University of Missouri-Rolla
Rolla, MO, USA

Nathan Ida

The University of Akron
Akron, OH, USA

Yasushi Kanai

Niigata Institute of Technology
Kashiwazaki, Japan

Leo C. Kempel

Michigan State University
East Lansing MI, USA

Andrzej Krawczyk

Institute of Electrical Engineering
Warszawa, Poland

Stanley Kubina

Concordia University
Montreal, Quebec, Canada

Samir F. Mahmoud

Kuwait University
Safat, Kuwait

Ronald Marhefka

Ohio State University
Columbus, OH, USA

Edmund K. Miller

LASL
Santa Fe, NM, USA

Krishna Naishadham

Wright State University
Dayton, OH, USA

Giuseppe Pelosi

University of Florence
Florence, Italy

Vicente Rodriguez

ETS-Lindgren
Cedar Park, TX, USA

Harold A. Sabbagh

Sabbagh Associates
Bloomington, IN, USA

John B. Schneider

Washington State University
Pullman, WA, USA

Amr M. Sharawee

American University
Cairo, Egypt

Norio Takahashi

Okayama University
Tsushima, Japan

THE APPLIED COMPUTATIONAL ELECTROMAGNETICS SOCIETY

JOURNAL

Vol. 20 No. 3

November 2005

TABLE OF CONTENTS

“The Complementary Roles of Analysis, Synthesis, Numerics, and Experiment in Electromagnetics” C. Baum.....	157
“Linear Triangles versus Biquadratic Quadrangles in RCS computations” A. Herschlein, J. von Hagen, D. Löffler, and W. Wiesbeck.....	169
“A Modified LU Recombination Technique for Improving the Performance of Boundary Element Methods at Low Frequencies” H. Ke and T. Hubing.....	178
“FVTD Characterization of Substrate Effects for Archimedean Spiral Antennas in Planar and Conformal Configurations” C. Fumeaux, D. Baumann, and R. Vahldieck.....	186
“High Accuracy Evaluation of the EFIE Matrix Entries on a Planar Patch” M. Bibby and A. Peterson.....	198
“PML Absorbing Boundary Conditions for the Multiresolution Time-Domain Techniques Based on the Discrete Wavelet Transform” C. Repra, C. Pereira, A.C.L. Cabeceira, I. Barba, and J. Repra.....	207
“Response Bounds Analysis for Transmission Lines Characterized by Uncertain Parameters” S. Barmada, A. Musolino, and M. Raugi	213
“Analysis of Band-Pass Filter Characteristics in a Ferrite Device with Carbon Nanotube Electrodes” T. Umegaki, M. Ogawa, and T. Miyoshi.....	221
“An Alternative Method for Determining the Antenna Factor of a Monopole” B. Türetken	231
“A Second-Order Symplectic Partitioned Runge-Kutta Scheme for Maxwell’s Equations H. Zhi-Xiang and W. Xian-Liang.....	235

The Complementary Roles of Analysis, Synthesis, Numerics, and Experiment in Electromagnetics

Carl E. Baum

University of New Mexico
Department of Electrical and Computer Engineering
Albuquerque New Mexico 87131

Abstract: The electromagnetic enterprise is now over a century old. In the modern world it has expanded in various directions. This paper summarizes electromagnetics under four headings: analysis, synthesis, numerics, and experiment. Each area is important, as are the relations between the areas.

I. Introduction

Electromagnetics has come a long way since its nineteenth century beginnings. Most notably with the discovery of the Maxwell equations (1864) and their experimental verification by Heinrich Hertz (1888), things were off and running, leading to today's state of the art. For more historical details the reader can consult [9, 20, 25].

In recent paper [7] I discussed the role of the electromagnetic theorist and how it fits in the general scientific/engineering enterprise:

People often think of dividing the basic and applied sides of the technological enterprise as between science and engineering, but this can lead to confusion.

This work was sponsored in part by the Air Force Office of Scientific Research, and in part by the Air Force Research Laboratory, Directed Energy Directorate. This was originally given as an invited paper for the 18th Annual Review of Progress in Applied Computational Electromagnetics, Monterey, CA, March 2002.

I think that there is a better three-part division, which can shed some light on where electromagnetic (EM) theory fits into the structure. First, there is the basic scientific side which has electromagnetics as part of physics, and the fundamental question concerns the replacement of the Maxwell equations by something more accurate, applying to extreme conditions not normally encountered.

This is not of what we think as electromagnetic theory in the usual sense. Second, we have what may be called applied science or basic engineering in which we explore the established physical laws (the Maxwell equations in this case) to see what they imply in the sense of discovering what is possible to analyze, synthesize, optimize, etc. This is distinct from the third category which might be termed applied engineering which concerns itself with the routine implementation of what is known from the second category in terms of technological products ("practicing" engineering), for example, by selection of antenna designs from a product catalog. Of course the reader might prefer some other "diagonalization" but this should suffice for the present.

Here we are not considering the first category, but the second and to some degree the third. Now take the Maxwell equations

$$\begin{aligned}\nabla \times \vec{E} &= -\frac{\partial \vec{B}}{\partial t} = \vec{J}_h^{(s)}, \\ \nabla \times \vec{H} &= -\frac{\partial \vec{D}}{\partial t} + \vec{J} + \vec{J}^{(s)}\end{aligned}\quad (1.1)$$

as given and see what useful things we can do with them. Note that we have separated out source terms and that material parameters (e.g., the constitutive parameters including boundary conditions) need to be specified.

There are various aspects of the electromagnetics enterprise undertaken by the scientific/engineering community since the fundamentals were first established. In this paper we divide modern electromagnetics into four categories: analysis, synthesis, numerics, and experiment. Each has its place in the overall subject, contributing its own important role.

II. Analysis

Initial investigations in electromagnetic theory were in a form which we can call analysis. Initially (for good and/or ill) people did not have the modern computers to directly solve the Maxwell equations in time and/or frequency domains. As such, various mathematical techniques were developed to find exact and approximate results for problems concerning antennas, scattering, and propagation. These are summarized in various classic texts, e.g., [10, 12, 14, 17, 18].

These results were key to the many advances in communications (radio, television), remote sensing (radar), and electric power.

Let us list some of the important analytic concepts and techniques:

1. Fourier/Laplace transforms
 - relating time and frequency domains,
 - consequence of linearity and time-invariance of common EM problems.

2. Separation of variables (spatial coordinates)
 - applies to certain coordinate systems.
3. Analytic properties in complex-frequency plane.
 - 3.1. Low-frequency method
 - expansions in powers of s ,
 - quasistatic leading term (separation into electrostatic and magnetostatic),
 - multipole expansions.
 - 3.2. Singularity expansion method (SEM)
 - expansion in terms of poles in the s -plane (plus other singularities in some cases),
 - factorization of poles in terms of natural frequencies, natural modes and coupling coefficients depending on different parameters of the problem,
 - damped sinusoids in time domain.
 - 3.3. High-frequency method
 - ray optics,
 - diffraction (GTD, UTD, etc.),
 - high frequency asymptotics,
 - asymptotic evaluation of integrals.
4. Conformal transformation of two-dimensional complex coordinates
 - capacitances, inductances of many shapes,
 - TEM modes on appropriate structures,
 - combination with stereographic transformation for conical structure.
5. Transmission-line theory
 - exact for TEM structures,
 - lumped-element transmission lines,
 - approximate application to wire antennas and scatterers,

- multiconductor transmission lines (including nonuniform).
6. Integral equations
 - special techniques, e.g., Wiener-Hopf,
 - approximate solution (variational techniques),
 - operator diagonalization (eigenvalues and eigenmodes).
 7. Electromagnetic topology
 - dividing electromagnetic systems into smaller pieces such that the solution for the smaller pieces can be recombined to represent the solution of the whole,
 - graph theory,
 - BLT equation, scattering matrices,
 - hybrid analytical/numerical.

In some cases these give the complete solution where at most one needs to evaluate a few special functions. In others one may have a solution in terms of an infinite series which needs to be numerically computed. In yet other cases the solution is only approximate.

Perhaps the greatest benefit of analytic solutions is the understanding they allow one to have concerning how the solution varies as a function of the various parameters of the problem. These include the various physical dimensions, direction of wave propagation, and frequency/time. This in turn allows one to see the possibilities of electromagnetic performance over the range of these variables—the engineering problem and the beginning of electromagnetic synthesis (or design).

III. Synthesis

3.1. Background

In contrast to analysis which is concerned with solving Maxwell equations for a specific set of conditions (geometry, constitutive parameters, sources),

synthesis begins with some desired performance and asks if an electromagnetic device can be designed to meet this performance. Then one may ask if there is more than one possible design, and which of these is optimal in some sense. This is a kind of inverse problem which may not always have a solution, or the solution may be nonunique.

By analogy it is instructive to recall circuit analysis. Circuit analysis is based on the Kirchoff laws:

Voltage law: The sum of the voltage drops around a loop in the network is zero.

Current law: The sum of the currents entering a node in the network is zero.

The network is a graph consisting of nodes and branches (a kind of topology or structure of connectedness). For a linear network (typically with branches containing inductances, capacitances, resistances, and voltage/current sources) one forms a matrix relating the response (voltages or currents) to the appropriate sources. Inverting this matrix gives the solution for the response.

Circuit synthesis goes beyond analysis to ask what such networks can be made to do, and to give procedures (algorithms) for synthesizing (designing) networks to meet such performances. This involves positive-real functions and matrices for the impedances and admittances of linear, passive, time-invariant networks. This becomes bounded-real functions and matrices for scattering parameters. Based on these one can decide if certain impedance (admittance) functions and transfer functions are realizable, and for the realizable ones the synthesis procedures. A common text is [11] and a collection of the basic papers is found in [13].

Electromagnetic synthesis is then first the determination of what kinds of electromagnetic devices (systems) with what performance parameters are

possible (within specified limitations such as linearity, reciprocity, time invariance, etc.). This is followed by the determination of the specific synthesis (design) procedure for realizing the desired performance.

A classic example of such synthesis is the Dolph-Tchebyscheff amplitude distribution for a uniform spaced array of antenna elements [16]. This finds the minimum achievable beam width for a specified sidelobe level. As this example shows, an important aspect of synthesis concerns how one asks the synthesis question. Problem formulation is key to obtaining useful results. Another notable antenna success concerns pattern synthesis for reflector antennas [21]. Note for these examples that they have been considered in a single-frequency (narrow-band) context. We also need to consider time-domain properties (large band ratios) of electromagnetic systems.

In order to extend the possibilities of electromagnetic synthesis, we need to extend the conceptual framework in which to pose the question. In electromagnetics we are dealing with distributed (continuous) systems, giving a more complicated problem than a comparatively simple LRC circuit. On the other hand the very complexity of the electromagnetic synthesis problem suggests that there may be many more possibilities. Not only do we have constitutive parameters and their frequency dependences to consider. We also have spatial distributions and shapes (geometry) to synthesize.

An approach to electromagnetic synthesis that has met with some success begins with a search for analytic concepts used in modern mathematics and physics, but not commonly used in electromagnetics. This is discussed in [3, 7] and summarized here.

3.2. Eigenimpedance synthesis

Let us first consider a synthesis technique which is an extension of circuit synthesis (discussed above) into the more general electromagnetic domain. This begins with an integral equation of the form

$$\left\langle \begin{matrix} \overleftrightarrow{Z}(\vec{r}, \vec{r}'; s); \vec{J}(\vec{r}, s) \end{matrix} \right\rangle = \begin{matrix} \vec{E}^{(inc)} \\ E \end{matrix}(\vec{r}, s) \quad (3.1)$$

(with integration over the common coordinate \vec{r}'). This could be a surface (S) or volume (V) integral equation over the body of interest (the support). Here, for convenience, we take the symmetric impedance (or E-field) kernel, based on the dyadic Green function of free space. As with matrices we can find eigenvalues and eigenvectors via

$$\begin{aligned} \left\langle \begin{matrix} \overleftrightarrow{Z}(\vec{r}, \vec{r}'; s); \vec{J}_\beta(\vec{r}, s) \end{matrix} \right\rangle &= \tilde{Z}_\beta(s) \vec{J}_\beta(\vec{r}, s) \\ &= \left\langle \begin{matrix} \vec{J}_\beta(\vec{r}, s); \overleftrightarrow{Z}(\vec{r}, \vec{r}'; s) \end{matrix} \right\rangle, \\ \vec{J}_\beta(\vec{r}, s) &\equiv \text{eigenmodes} \\ \tilde{Z}_\beta(s) &\equiv \text{eigenimpedances (eigenvalues)}, \\ \left\langle \begin{matrix} \vec{J}_{\beta_1}(\vec{r}, s); \vec{J}_{\beta_2}(\vec{r}, s) \end{matrix} \right\rangle &= 1_{\beta_1, \beta_2} = \begin{cases} 1 & \text{for } \beta_1 = \beta_2 \\ 0 & \text{for } \beta_1 \neq \beta_2. \end{cases} \end{aligned} \quad (3.2)$$

With this we have the eigenmode expansion method (EEM) as

$$\overleftrightarrow{Z}^v(\vec{r}, \vec{r}'; s) = \sum_{\beta} \tilde{Z}_\beta^v(s) \vec{J}_\beta(\vec{r}, s) \vec{J}_\beta(\vec{r}', s) \quad (3.3)$$

where v is an arbitrary power.

Note that the eigenvalues are dimensionally impedances (ohms) for a surface type body, and ohm-meters for a volume type body. For a passive, linear, reciprocal scatterer, the $\tilde{Z}_\beta(s)$ are positive real functions like the impedance functions considered in circuit synthesis discussed previously.

As discussed in [3] for a surface type body one can add a sheet impedance $\tilde{Z}_\ell(s)$ everywhere on S .

This gives new eigenvalues

$$\tilde{Z}_\beta(s) \rightarrow \tilde{Z}_\beta(s) + \tilde{Z}_\ell(s) \quad (3.4)$$

with no change in the eigenmodes. A similar result holds for volume type bodies [5]. Now knowing the behavior of some $\tilde{Z}_\beta(s)$ we have a circuit synthesis problem for $\tilde{Z}_\ell(s)$ to obtain the desired new eigenvalue. An application of this notes that the natural frequencies (SEM, Section 2) satisfy

$$\tilde{Z}_\beta(s_{\beta,\beta'}) = 0, \quad (3.5)$$

so one can change the natural frequencies of a target (important for identification) to other complex frequencies depending on the choice of $\tilde{Z}_\ell(s)$. An example of this is the thin wire [3] for which the lowest order natural frequency can be moved to the negative real axis of the s plane and even produce a second order pole (critically damped scatterer or antenna).

3.3. Symmetry and group theory

A branch of mathematics which has found much use in quantum mechanics is group theory, closely associated with symmetry. Group theory also has much application to symmetries in electromagnetics problems (antennas, scattering, propagation) [21]. Symmetries in antennas and scatterers are associated with symmetries in the electromagnetic waves, and can be used to design antennas and scatterers and identify radar targets.

The simple case of a 3×3 dyadic representation of a group has

$$G = \left\{ \overset{\leftrightarrow}{G}_\ell \mid \ell = 1, 2, \dots, \ell_0 \right\},$$

$$\ell_0 = \text{group order (finite or infinite)}, \quad (3.6)$$

$$\overset{\leftrightarrow}{G}_\ell \in G, \quad \overset{\leftrightarrow}{1} \equiv \text{identity} \in G,$$

$$\overset{\leftrightarrow}{G}_{\ell_1} \cdot \overset{\leftrightarrow}{G}_{\ell_2} \in G \text{ for all ordered pairs.}$$

This form is particularly suitable for the point symmetry groups (rotations and reflections) for which the dyadics are real and orthogonal. Other types of applicable symmetries include space groups (adding translation) and the linear group (dilation symmetry). Note that in addition to the geometrical symmetries, there are symmetries inherent in the Maxwell equations (reciprocity, duality, relativistic invariance) which need to be incorporated in the group structure.

All early application of symmetries to electromagnetics was the case of special waveguide junctions (magic T, etc.). Some of the recent symmetry results include [7]:

1. placement and orientation of EM sensors on an aircraft to minimize the influence of aircraft scattering on the measurement (reflection symmetry R),
2. high-frequency capacitors (dihedral symmetry D_N),
3. nondepolarizing axial backscatter (two-dimensional rotation symmetry C_N for $N \geq 3$, e.g., an N-bladed propeller),
4. generalized Babinet principle (for dyadic impedance sheets) and self-complementary structures (C_{Nc} symmetry),
5. vampire signature (zero backscatter cross polarization in h, v radar coordinates) for mine identification (continuous two-dimensional rotation/reflection symmetry $O_2 = C_{\infty a}$ [10],
6. separation of magnetic-polarizability dyadic

$$\overset{\leftrightarrow}{M}(s) = \vec{M}_z(s) \overset{\rightarrow}{1}_z \overset{\rightarrow}{1}_z + \overset{\leftrightarrow}{M}_t(s) \overset{\leftrightarrow}{1}_z$$

into distinct longitudinal and transverse parts, for

low-frequency magnetic singularity identification (diffusion dominated natural frequencies) of metallic targets (C_N symmetry for $N \geq 3$),

7. categorization of the scattering dyadic for the various point symmetries, including reciprocity and self dual case.

3.4. Differential geometry for transient lens synthesis.

We begin with some as yet unspecified (u_1, u_2, u_3) orthogonal curvilinear coordinate system with

$$h_n^2 = \left[\frac{\partial x}{\partial u_n} \right]^2 + \left[\frac{\partial y}{\partial u_n} \right]^2 + \left[\frac{\partial z}{\partial u_n} \right]^2, \quad (3.7)$$

where the scale factors $n = 1, 2, 3$, and the line element

$$[d\ell]^2 = \sum_{n=1}^3 h_n^2 [du_n]^2 = [dx]^2 + [dy]^2 + [dz]^2.$$

The electromagnetic field and constitutive parameters are described as real (indicating they can be measured) when expressed in the usual way in Cartesian coordinates. The formal fields and constitutive parameters are primed and denote these parameters expressed in the (u_1, u_2, u_3) system and thought of as though this were a Cartesian system.

The formal and real fields are related by

$$\begin{aligned} \vec{E}' &= (\alpha_{n,m}) \cdot \vec{E}, & \vec{H}' &= (\alpha_{n,m}) \cdot \vec{H}, \\ \vec{D}' &= (\beta_{n,m}) \cdot \vec{D}, & \vec{B}' &= (\beta_{n,m}) \cdot \vec{B}, \\ (\alpha_{n,m}) &= (1_{n,m} \ h_n) = \begin{pmatrix} h_1 & 0 & 0 \\ 0 & h_2 & 0 \\ 0 & 0 & h_3 \end{pmatrix}, \\ (\beta_{n,m}) &= \left(1_{n,m} \ \frac{h_1 h_2 h_3}{h_n} \right) = \begin{pmatrix} h_2 h_3 & 0 & 0 \\ 0 & h_3 h_1 & 0 \\ 0 & 0 & h_1 h_2 \end{pmatrix}. \end{aligned} \quad (3.8)$$

For the constitutive parameters we have for the special case of diagonal dyadics (in the u_n system)

$$\begin{aligned} \overleftrightarrow{\varepsilon}' &= (\gamma_{n,m}) \cdot \overleftrightarrow{\varepsilon}, & \overleftrightarrow{\mu}' &= (\gamma_{n,m}) \cdot \overleftrightarrow{\mu}, \\ (\gamma_{n,m}) &= (\beta_{n,m}) \cdot (\alpha_{n,m})^{-1} = \begin{bmatrix} \frac{h_2 h_3}{h_2} & 0 & 0 \\ 0 & \frac{h_3 h_1}{h_2} & 0 \\ 0 & 0 & \frac{h_1 h_2}{h_3} \end{bmatrix}. \end{aligned} \quad (3.9)$$

The synthesis procedure is to:

1. postulate waves (e.g., TEM wave propagating in the u_3 direction) with simple (e.g., uniform) $\overleftrightarrow{\varepsilon}'$ and $\overleftrightarrow{\mu}'$,
2. place some constraint on $\overleftrightarrow{\varepsilon}$ and $\overleftrightarrow{\mu}$ (e.g., nonuniform but isotropic),
3. ask what coordinate systems (μ_n) are able to satisfy the resulting constraints on the h_n ,
4. use solution to 3 to form the basis of a lens, the solution for the wave being given by the transformation equations.

With postulated frequency-independent constitutive parameters such lenses are dispersionless and are called transient lenses. For TEM waves guided by perfect conductors (as on TEM transmission lines) the conductors follow the curved coordinate lines through the lens.

Various results have been achieved [7, 19]:

1. all six components of \vec{E} and \vec{H} nonzero for inhomogeneous but isotropic $\varepsilon, \varepsilon', \mu,$ and μ' (only two possible coordinate systems),
2. TEM waves propagating in the u_3 direction, for inhomogeneous but isotropic $\varepsilon, \varepsilon', \mu,$

and μ' (coordinate systems constrained by constant u_3 surfaces being planes or spheres, examples including converging, diverging, and bending lenses),

3. two-dimensional lenses for TEM waves (only one component each of \vec{E}' and \vec{H}' nonzero) based on conformal transformations (resulting in only one of ε and μ being inhomogeneous, but both isotropic),
4. lenses with $\mu = \mu_0$ but ε anisotropic and inhomogeneous,
5. TEM waves propagating in the ϕ direction in a cylindrical (Ψ, ϕ, z) coordinate system (bending lens) with very general transmission-line cross sections (e.g., bent circular coax) with only ε variation ($\mu = \mu_0$).

3.5. *Electromagnetic topology for electromagnetic system design*

In section 2 (item 7) electromagnetic topology was considered as an analytic way of dividing a system into smaller parts in a way that the solution for the pieces can be recombined to form a mathematical description of the whole (BLT equation). However, the original conception was to have a way of quantitatively controlling electromagnetic interference, i.e., a method of system design [4].

In this design procedure one considers a set of closed surfaces called shields or subshields. (There can be a hierarchy of these). The object is to control all electromagnetic signals passing through such surfaces. By the electromagnetic uniqueness theorem, controlling tangential \vec{E} (or \vec{H}) on such a surface controls the fields inside (for sources outside). Unwanted signals are stopped at such shields. The realization of such

surfaces may include metal sheets, screens, etc. The important parts of the surfaces are the penetrations (apertures, conductors passing through), every one of which must be quantitatively described for purposes of control.

An important concept for such control is norms [4] (This is applied in the context of the good-shielding approximation.) These reduce the associated matrices (including convolution in time domain) to simple scalars which can be used to bound the penetrating signals. Not only linear protection devices (such as filters), but other types of simple nonlinear devices can also be included in the formalism.

There is a quantitative side of electromagnetic topology in which one writes the BLT equation [4, 26]

$$\begin{aligned} & \left[\left((I_{n,m})_{u,v} \right) - \left((\tilde{S}_{n,m}(s))_{u,v} \right) \circ \left((\tilde{\Gamma}_{n,m}(s))_{u,v} \right) \right] \circ \left((\tilde{V}_n^{(0,s)}(u)) \right) \\ & = \left((\tilde{S}_{n,m}(s))_{u,v} \right) \circ \left((\tilde{\Lambda}_{n,m}(z'_{u,s}(\cdot)))_{u,v} \right) \circ \left[\left((\tilde{V}_n^{(s)}(z'_{u,s})) \right)_u \right]. \end{aligned} \quad (3.10)$$

This involves supervectors and supermatrices. The outer indices (u and v) are topological in that they label waves propagating on tubes (multiconductor transmission lines) between junctions (or black boxes if one prefers). This corresponds to a graph called the interaction sequence diagram which is dual to the electromagnetic topology with tubes dual to surfaces and junctions dual to volumes. The inner indices (n and m) can be regarded as more “numerical” in nature, corresponding to the calculational details in constructing the solution to the individual “pieces” of the system problem (whether calculated or measured). The terms in the BLT equation are

$$\begin{aligned} \left((\tilde{S}_{n,m}(s))_{u,v} \right) & \equiv \text{scattering matrix from } v\text{th wave to } u\text{th} \\ & \text{wave,} \\ \left((\tilde{\Gamma}_{n,m}(s))_{u,u} \right) & \equiv \text{propagation matrix for } u\text{th wave} \\ & \text{(supermatrix being block diagonal),} \end{aligned}$$

$$\begin{aligned}
\left(\tilde{\Lambda}_{n,m}(z'_u, s; (\bullet))\right)_{u,u} &\equiv \text{integral operator operating on} \\
&\text{distributed sources} \\
&\left(\tilde{V}_n^{(s)'}(z'_u, s)\right)_{u,u}, \\
\left(\tilde{V}_n(0, s)\right)_u &\equiv \text{outgoing wave from junction combining} \\
&\text{voltages and currents.}
\end{aligned}
\tag{3.11}$$

The BLT equation is also generalized to cover more general cases, including nonuniform multiconductor transmission lines [27]. Special results hold for early and late times [28]. Work is proceeding to include more and more parts of the electromagnetic system in the general BLT formalism [29, 30]. In essence the BLT formalism is a way to take the solutions (and/or data) for the “pieces”, and concatenate them together to solve for the total system. A special issue of the journal *Electromagnetics* is in preparation concerning this general problem, based on an RF effects MURI sponsored by AFOSR.

IV. Numerics

This is not a discussion of how EM numerics are done, but rather where this part of electromagnetics fits into the larger picture.

4.1. Complement to analysis

One aspect of EM numerics is as a complement to analysis. This has the potential of extending the knowledge of basic electromagnetics processes by definitive calculations of canonical problems, particularly those beyond full analytic treatment. Of even greater significance is the use of a hybrid analytical/numerical treatment. By this is meant that analysis is used to partly solve the problem, including the division of the problem into analytical and numerical parts. For example, the electromagnetic

response can be viewed as an analytic function of the complex frequency (in various parts of the complex s -plane). One can use this fact to reduce the number of frequencies used in the computation, the response at other frequencies being implied by analytic continuation. This dovetails with item 3 in Section 2. Note, however, that this type of computation is still limited to structures of not-too-great complexity so that one can trust the accuracy of the numerical part of the solution. By this procedure one can extend the library of canonical solutions of antennas, scatterers, and other electromagnetic structures.

Various other examples of hybrid analytical/numerical solutions are also available. In the case of reflector impulse-radiating antennas (IRAs) [2] the impulsive part of the radiation has been reduced from a surface integral to a contour integral around the aperture. Stereographic transformation reduces the conical feed assembly to an equivalent cylindrical one, making the problem one of conformal transformation in two dimensions. While this has an analytic (closed form) solution for many interesting cases, more complicated feed geometries can be approached by a numerical computation of the potential function from an appropriate integral equation [2]. The low-frequency behavior of reflector IRAs depends on the electric and magnetic dipole moments. Not being analytically calculable the electric-dipole moment has been successfully treated in [1].

4.2. Role in synthesis

Synthesis (Section 3) defines the optimization conditions and develops realization algorithms. Sometimes there are steps which require numerical computation as part of the problem. See, e.g., Section 3.2. Eigenimpedances of the unloaded scatterer are needed to begin the synthesis. These may require

numerical computation. The role of EM numerics is then a hybrid one, similar to Section 4.1, in which numerical techniques play an essential role.

4.3. *Substitute for experiment in not – too - complicated geometries.*

One can think of an experiment as an *analog* computation or *physical* simulation, particularly if some electromagnetic scaling (scale model) is involved. Within the state of the art of numerical techniques, one can think of a numerical computation as a *digital* computation or *mathematical* simulation. One can think of such problems as semisimple: beyond analysis but within numerical capability. The scope of such problems will increase along with the numerical state of the art.

At this point we can also mention the role of numerics in teaching electromagnetics. It would seem that most students of the subject are headed for industry where they are expected to use general numerical EM computer codes to address problems like design of realistic antennas with various real-world compromises included. So, professors need to teach this (and write papers on it).

For semisimple problems numerical computation will likely replace much experiment, being even more accurate than experiment in some cases.

4.4. *Role in response of large complex systems*

For large, complex systems experiment is essential and both analysis and numerics play but a supporting role. For example, the maze of wiring and conductors in a modern aircraft, communication center, etc., is so large that even describing it is difficult, much less computing its electromagnetic response (especially at high frequencies). These large problems are too complex to reliably calculate. Even if one could

accurately calculate the response of such a system, the answer would still normally be incorrect because the system one calculates differs from the actual piece of hardware, the response of which one desires, in important ways. Wires are not always where they are supposed to be, additional wires have been added, seals have corroded, etc.

This is not to say that numerics has no role in modeling the response of such systems. Such computations can be used as an adjunct to EM experiments (system-level tests) to compare to the experimental results and discover what parts of the system are not being adequately modeled. This also gives insight into the important system features controlling important aspects of the system response, and aids in modifying (hardening) the system so as to reduce or remove undesirable responses.

For complex systems electromagnetic topology (Section 3.5) can play an important role in such computations. An important example of such a computer code is CRIPTE [23] which has made the largest system computations to date with some success. This and/or similar computer programs need to be further refined and expanded.

V. Experiment

5.1. *Simple structures*

As discussed in comparison with numerics (Section 4) measurements of the EM properties of simple structures is becoming replaced by numerical techniques (for cases that analysis is not sufficiently capable). Even the metal-shear school of antenna design is being replaced by the iterative-number-crunching school of antenna design. Experiment does, however, have some pedagogical benefits and as a demonstration to nonexperts in EM in the case of simple structures.

5.2. *Electromagnetic sensors*

In experiments various electromagnetic sensors (special antennas) are needed to measure electric and magnetic fields as well as voltages and currents. Much analysis and synthesis has gone into the design of such sensors [6, 15]. Numerical techniques can be applied here as well. The point is that EM experiments are strongly impacted by other aspects of electromagnetics (Sections 2-4).

5.3. *Measurement of electromagnetic properties of materials and scatterers*

One measures the constitutive parameters of materials by special kinds of experiments in which the measured voltage, current, etc., are used to infer these parameters. More generally remote sensing techniques (including radar) are used to locate various objects, characterize them, and even identify targets from their scattering properties. Fundamental to this are analytic concepts relating the scattering to the EM properties of a target (inverse scattering in the general case).

Target recognition (identification) is, of course, an experimental discipline. However, this has a strong dependence on analysis. One has some model of the scattering in which certain parameters are used for the discrimination. For example SEM (Section 3.2) uses the aspect-independent natural frequencies as target identifiers [8]. The scattering data needs to be processed, an inherently numerical procedure (hybrid analytical/numerical technique, Section 4.1), so as to be able to use these parameters. Various data-processing algorithms have been developed in this context [8].

5.4. *Demonstration of performance of products*

Another common occasion of experiment concerns the final performance characteristics of an EM system, particularly a commercial one. For example, a

radar system will be tested for its capability for detecting targets at various ranges. Note that in such tests not only are EM parameters measured but other (such as) mechanical parameters as well. An EM system has to operate in various environments.

5.5. *Measurement of response of large, complex systems*

As previously commented, the calculation of the response of large complex electronic systems to arbitrary incident electromagnetic environment is a daunting task. Here we are not concerned with the designed response to some communication or radar signal, but rather the more general out-of-band “back door” response (see Section 4.4).

The response of large complex electronic systems is primarily an experimental problem. It is, however, a difficult problem. How does one go about testing a system to the variety of waveforms and frequencies of interest, including full amplitudes, variation of polarization and angle of incidence, and system configuration as its intended operational environment? One can see that an adequate experiment to determine that a system will successfully operate in some environment (including appropriate variation of the parameters describing the environment) is itself a difficult task.

The primary reason for doing a full system test is that it is in some sense self diagnosing. The fact that we do not have a completely accurate description of the system is mitigated by having a real one in front of us. Of course, we still need to have it in its operational configuration, including especially, all electrical connections. Here one must be cautioned in that many tests done to various standards may be incomplete. I am reminded that during the Cold War very extensive (and expensive) testing was performed on some

military systems (way beyond any MIL standard), for the nuclear electromagnetic pulse (EMP). For large complex electronic systems these came quite close to reality. These are the kinds of tests about which I am talking.

Even so, real tests are limited and one must deal with various factors (discussed in more detail in a previous paper [6 (Section VI)]):

1. What does it mean for a system to survive a given environment?
2. How does one know that a system will survive a given environment?
3. Complete system test.
4. Extrapolation.
5. Influence of system design (topology) on ease of testing: penetration tests.
6. Low-level testing.
7. Characterization of failure-port response parameters.
8. Probabilistic estimates.

While analytical/numerical techniques cannot hope to make high-confidence predictions for the entire system before the test, they can help guide the experiment. Surprises can point to system features that were unknown or were assumed insignificant before the test. Making the model agree with the data (postdiction) sheds insight into what are important signal paths, and what one may need to do to reduce certain signals to acceptable levels. Theory with experiment in this case is better than either alone.

VI. Concluding remarks

Electromagnetics has expanded into a large intellectual edifice with many practical applications since the beginning of the electromagnetics age in the nineteenth century. Here we have summarized the

subjects under four main headings: analysis, synthesis, numerics, and experiments. Each area is important on its own, but the mutual support between each of these and the others is also important.

It would be interesting to know how the subject will advance in the next century. I expect the advancing speed of computers will allow considerably larger computation to be performed. I hope that at least some individuals will come up with whole new fundamental ideas in the analysis and synthesis areas.

VII. References

- [1] D. V. Giri and S. Y. Chu, "On the Low-Frequency Electric Dipole Moment of Impulse Radiating Antennas (IRAs)," *Sensor and Simulation Note* 346, October 1992.
- [2] J. S. Tyo, "Optimization of the Feed Impedance for an Arbitrary Cross-Feed-Arm Impulse Radiating Antenna," *Sensor and Simulation Note* 438, November 1999; "Optimization of the TEM Feed Structure for Four-Arm Reflector Impulse Radiating Antennas," *IEEE Trans. Antennas and Propagation*, pp. 607-614, 2001.
- [3] C. E. Baum, "Emerging Technology for Transient and Broad-Band Analysis of Antennas and Scatterers," *Interaction Note* 300, November 1976; *Proc. IEEE*, pp. 1598-1616, 1976.
- [4] C. E. Baum, "The Theory of Electromagnetic Interference Control," *Interaction Note* 478, December 1989; pp. 87-101 in J.B. Andersen (ed.), *Modern Radio Science 1990*, Oxford University Press, 1990.
- [5] G. W. Hanson and C. E. Baum, "A Volumetric Eigenmode Expansion Method for Dielectric Bodies," *Interaction Note* 517, August 1996.
- [6] C. E. Baum, "From the Electromagnetic Pulse to High Power Electromagnetics," *System Design and Assessment Note* 32, June 1992; *Proc. IEEE*, pp. 789-817, 1992.
- [7] C. E. Baum, "Application of Concepts of Advanced Mathematics and Physics to the Maxwell Equations," *Physics Note* 11, November 1999; in P.D. Smith et al (eds.), *Ultra-Wideband*,

- Short-Pulse Electromagnetics 5, Kluwer/Plenum Press, pp. 39-52, 2002.
- [8] C. E. Baum, E. J. Rothwell, K.M. Chen, and D.P. Nyquist, "The Singularity Expansion Method and Its Application to Target Identification," Proc. IEEE, 1991, pp. 1481-1492.
- [9] D. L. Sengupta and T. K. Sarkar, "Maxwell, Hertz, The Maxwellians and The Early History of Electromagnetic Waves," Proc. IEEE Antennas and Propagation Society International Symposium, July 2001, vol. 1, pp. 14-18.
- [10] J. A. Stratton, *Electromagnetic Theory*, McGraw Hill, 1941.
- [11] E. A. Guillemin, *Synthesis of Passive Networks*, Wiley, 1957.
- [12] L. B. Felson and N. Marcuvitz, *Radiation and Scattering of Waves*, Prentice Hall, 1974.
- [13] M. E. Van Valkenburg (ed.), *Circuit Theory: Foundations and Classical Contributions*, Dowden, Hutchinson and Ross, 1974.
- [14] J. Van Bladel, *Electromagnetic Fields*, Hemisphere Taylor and Francis, 1985.
- [15] C. E. Baum, "Electromagnetic Sensors and Measurement Techniques," in J. E. Thompson and L. H. Luessen (eds.), *Fast Electrical and Optical Measurements*, Martinus Nijhoff (Kluwer), pp. 73-144, 1986.
- [16] J. D. Krauss, *Antennas*, McGraw Hill, 2nd Ed., 1982.
- [17] W. R. Smythe, *Static and Dynamic Electricity*, 3rd Ed., Hemisphere Taylor and Francis, 1989.
- [18] R. E. Collin, *Field Theory of Guided Waves*, IEEE Press, Oxford University Press, 1991.
- [19] C. E. Baum and A. P. Stone, *Transient Lens Synthesis: Differential Geometry in Electromagnetic Theory*, Hemisphere Taylor and Francis, 1991.
- [20] R. S. Elliott, *Electromagnetics: History, Theory, and Applications*, IEEE press, 1993.
- [21] Y. Ramat-Samii, "Modern Concepts in Analysis, Synthesis and Measurements of Antennas," in H. Matsumoto (ed.), *Modern Radio Science* 1993, Oxford University Press, pp. 75-104, 1993.
- [22] C. E. Baum, and H. N. Kritikos, "Symmetry in Electromagnetics," ch. 1, in C. E. Baum and H. N. Kritikos (eds.), *Electromagnetic Symmetry*, Taylor and Francis, pp. 1-90, 1995.
- [23] J. P. Parmentier and P. Degauque, "Topology Based Modeling of Very Large Systems," in J. Hamelin (ed.), *Modern Radio Science* 1996, Oxford University Press, pp. 151-177, 1996.
- [24] C. E. Baum, E. G. Farr, and D. V. Giri, "Review of Impulse-Radiating Antennas," in W. R. Stone (ed.), *Review of Radio Science* 1996-1999, Oxford University Press, pp 403-439, 1999.
- [25] J. Van Bladel, "From Maxwell to Einstein," in P. D. Smith et al (eds.), *Ultra-Wideband, Short-Pulse Electromagnetics 5*, Kluwer/Plenum Press, pp. 1-9, 2002.
- [26] C. E. Baum, T. K. Liu, and F. M. Tesche, "On the Analysis of General Multiconductor Transmission-Line Networks," *Interaction Note* 350, November 1978; also in C. E. Baum, "Electromagnetic Topology for the Analysis and Design of Complex Electromagnetic Systems", in J. E. Thompson and L. H. Luessen, *Fast Electrical and Optical Measurements*, Martinus Nijhoff, Dordrecht, pp. 467-547, 1986.
- [27] C. E. Baum, "Extension of the BLT Equation into Time Domain," *Interaction Note* 553, March 1999; Proc. 14th EMC Symposium, Zurich, pp. 211-216, 2001.
- [28] C. E. Baum, "Generalization of the BLT Equation," *Interaction Note* 511, April 1995; Proc. 13th EMC Symposium, Zurich, pp. 131-136, 2001.
- [29] C. E. Baum, "Including Apertures and Cavities in the BLT Formalism," *Interaction Note* 581, January 2003.
- [30] F. M. Tesche, "On the Addition of EM Field Propagation and Coupling Effects in the BLT Equation," December 2003.

Linear Triangles versus Biquadratic Quadrangles in RCS computations

Alexander Herschlein, Jürgen von Hagen, Dietmar Löffler, Werner Wiesbeck
 Institut für Höchsthfrequenztechnik und Elektronik,
 Universität Karlsruhe (TH), Kaiserstr. 12, 76133 Karlsruhe, Germany

Abstract—The present contribution compares the geometric approximations of linear triangles and biquadratic quadrangles for Boundary Element Methods. The PMCHW formulation for electromagnetic problems is applied to three canonical problems: a flat plate, a perfect electric conducting sphere, and a sphere with a low dielectric contrast. The biquadratic quadrangles show to yield more accurate numerical results at less meshing expense. Also, the surface elements may be larger than the ones of linear triangles.

I. INTRODUCTION

Numerical methods that discretize the boundaries between media are summarized as Boundary Element Methods. The accuracy of the computations based on the discretized boundaries relies mainly on two conditions: first, the geometrical approximation of the curved surfaces by suitably chosen elements, and second, the mathematical approximation of the physical quantities on the curved surface. Both parts should be carefully taken into account in order to obtain fast and accurate results.

The Method of Moments [1] is one particular Boundary Element Method that uses the electric and magnetic surface current densities on interfaces between two regions as physical quantities to be computed. For the formulation on the surface, the boundary conditions for the electric fields (electric field integral equation EFIE), the magnetic fields (magnetic field integral equation MFIE), or both (the so-called PMCHW formulation, [2]) are commonly used. The comprehensive formulation of the three integral formulations is detailed in [3] and shall not be repeated here. Only the PMCHW formulation results in physically correct solutions and shows no spurious modes even for closed bodies. Also the results for dielectric bodies are more accurate compared to only EFIE or MFIE formulations [4]. Common to all integral equations is the enforcement of the boundary conditions at the interface by induced electric and/or magnetic surface currents. In general, the geometry is approximated by surface elements. The surface current basis functions are then approximating the unknown surface currents on these surface elements.

Linear triangles [5] have commonly been used in the past for the geometrical approximation. Linear triangles are able to discretize almost any arbitrary surface and, hence, offer a considerable advantage to other, purpose-designed elements. In recent publications, the need for better approximations has become apparent. Curvilinear, triangular patches have been used in addition to higher order Lagrange polynomials on metallic bodies to represent

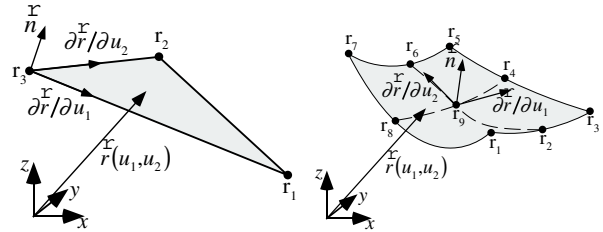


Fig. 1. Triangular (left) and biquadratic (right) surface patches for geometrical approximations.

the physical currents on the surface elements [6]. Considerable advantages have been shown [6] for the higher-order elements when applied to perfect conducting bodies.

In the present contribution, two basic shapes of surface elements are compared: the commonly used linear triangles [5] and biquadratic quadrangles [3], [7], [8]. The inherent shortcomings of triangles are identified based on physical considerations for the currents on simple canonical bodies, e.g., plates and spheres. The biquadratic quadrangles are shown to remedy the shortcomings while preserving the versatility of generally applicable surface elements. They are applied to the integral equations using the PMCHW formulation. The biquadratic elements result in smoother current distributions as well as physically correct current representations for scatterers with edges. The results obtained for the radar cross section of a metallic and a dielectric sphere are highly accurate even for a surface area larger than one hundredth of a squared wave length of each geometrical discretization element.

II. GEOMETRICAL APPROXIMATION OF ARBITRARY SHAPED SURFACES

A. Triangular Approximation

Linear triangles (see Fig. 1, left) offer two advantages. First, almost any geometry can be approximated by the linear triangles [5]. Second, the mathematical description of the surface representation is relatively simple.

Any point \vec{r}_n on the surface of a triangle n is parameterized by two local variables $u_1 \in [0 \dots 1]$ and $u_2 \in [0 \dots 1]$ by the equation

$$\vec{r}_n(u_1, u_2) = u_1 \vec{r}_{n1} + u_2 \vec{r}_{n2} + (1 - u_1 - u_2) \vec{r}_{n3}. \quad (1)$$

Here, \vec{r}_{nk} , $k = 1, 2, 3$ are the positions of the corners of the triangle n . As the surface of the triangle is planar, the object's surface is linearly interpolated.

B. Biquadratic Approximation

For an approximation of the surface of a body by biquadratic quadrangles, the surface of each element is approximating the scatterer's surface by two Lagrange interpolations using nine sample points: the four corners and, additionally, the four points on the center of the edges, and the center point of the surface element n [3], [7], [8], [9]

$$\vec{r}_n(u_1, u_2) = \sum_{k=1}^9 \alpha_{nk}(u_1, u_2) \cdot \vec{r}_{nk} \quad (2)$$

The form functions α_{nk} are obtained by the two-dimensional Lagrange interpolation and define any point on the surface of the element n :

$$\alpha_{n1}(u_1, u_2) = \frac{1}{4}u_1(u_1 - 1)u_2(u_2 - 1) \quad (3)$$

$$\alpha_{n2}(u_1, u_2) = \frac{1}{2}(1 - u_1^2)u_2(u_2 - 1) \quad (4)$$

$$\alpha_{n3}(u_1, u_2) = \frac{1}{4}u_1(u_1 + 1)u_2(u_2 - 1) \quad (5)$$

$$\alpha_{n4}(u_1, u_2) = \frac{1}{2}u_1(u_1 + 1)(1 - u_2^2) \quad (6)$$

$$\alpha_{n5}(u_1, u_2) = \frac{1}{4}u_1(u_1 + 1)u_2(u_2 + 1) \quad (7)$$

$$\alpha_{n6}(u_1, u_2) = \frac{1}{2}(1 - u_1^2)u_2(u_2 + 1) \quad (8)$$

$$\alpha_{n7}(u_1, u_2) = \frac{1}{4}u_1(u_1 - 1)u_2(u_2 + 1) \quad (9)$$

$$\alpha_{n8}(u_1, u_2) = \frac{1}{2}u_1(u_1 - 1)(1 - u_2^2) \quad (10)$$

$$\alpha_{n9}(u_1, u_2) = (1 - u_1^2)(1 - u_2^2) \quad (11)$$

where u_1 and u_2 take values between -1 and $+1$; they constitute the local coordinate system of each surface element. The sample points on the surface of the quadrangle are defined according to Fig. 1

$$\begin{aligned} \vec{r}_n(-1, -1) &= \vec{r}_1 & \vec{r}_n(0, -1) &= \vec{r}_2 & \vec{r}_n(1, -1) &= \vec{r}_3 \\ \vec{r}_n(-1, 0) &= \vec{r}_8 & \vec{r}_n(0, 0) &= \vec{r}_9 & \vec{r}_n(1, 0) &= \vec{r}_4 \\ \vec{r}_n(-1, 1) &= \vec{r}_7 & \vec{r}_n(0, 1) &= \vec{r}_6 & \vec{r}_n(1, 1) &= \vec{r}_5. \end{aligned}$$

As examples for the versatility of biquadratic quadrangles, Fig. 2 shows in each subfigure one single quadrangle. The corners r_1 , r_3 , r_5 , r_7 are highlighted by black points in Fig. 1. Each quadrangle approximates closely planar surfaces (a and c), curved surfaces with one (b and d), and two curvatures (g and h). A circle or a half-sphere are already closely represented by only one element, as seen in subfigure e and f, respectively. Note that each geometrical curve is approximated only by one biquadratic quadrangle.

C. Directional Derivatives

For any surface element n , the directional derivatives are necessary for the geometrical description and the sub-

sequent evaluation of the derivatives of the physical quantities on the surface elements [3], [7].

The directional derivatives are expressed in the local coordinates as

$$\frac{\partial \vec{r}_n(u_1, u_2)}{\partial u_1} \quad (12)$$

and

$$\frac{\partial \vec{r}_n(u_1, u_2)}{\partial u_2}. \quad (13)$$

The coefficients of the metric tensor are

$$g_{nij} = \frac{\partial \vec{r}_n(u_1, u_2)}{\partial u_i} \cdot \frac{\partial \vec{r}_n(u_1, u_2)}{\partial u_j} \quad (14)$$

with $i, j = 1, 2$ and obtained with the above directional derivatives. The determinant of the metric tensor for element n is

$$g_n = g_{n11}g_{n22} - g_{n12}^2. \quad (15)$$

The differential surface element is obtained by the differential coordinate system

$$d\vec{S}_n = \frac{\partial \vec{r}_n(u_1, u_2)}{\partial u_1} \times \frac{\partial \vec{r}_n(u_1, u_2)}{\partial u_2}. \quad (16)$$

The surface of the differential surface element is

$$dS_n = \sqrt{g_n} du_1 du_2. \quad (17)$$

The normal vector of the surface element is finally defined as

$$\vec{n}_n = \frac{1}{\sqrt{g_n}} \frac{\partial \vec{r}_n(u_1, u_2)}{\partial u_1} \times \frac{\partial \vec{r}_n(u_1, u_2)}{\partial u_2}. \quad (18)$$

The divergence of a physical quantity \vec{F} (later the electric or magnetic surface currents) acting in the surface is obtained by

$$\nabla_s \cdot \vec{F}_n(u_1, u_2) = \frac{1}{\sqrt{g_n}} \sum_{i=1}^2 \frac{\partial (f_{ui} \sqrt{g_n})}{\partial u_i}. \quad (19)$$

Here, the f_{ui} are the components of F in the two coordinate directions u_1 and u_2 .

III. PHYSICAL APPROXIMATION OF SURFACE CURRENTS: ROOF-TOP BASIS FUNCTIONS

Besides the geometrical approximation of the shape of a body, also the current densities on the surface elements need to be approximated. A physical representation of the currents is compulsory, furthermore, the representation should be as close as possible to the solution. Therefore, the following requirements should be fulfilled:

- no current flow orthogonal to an outer edge
- the normal component of a current at a common edge is constant and continuous. This ensures that no line charges are generated.

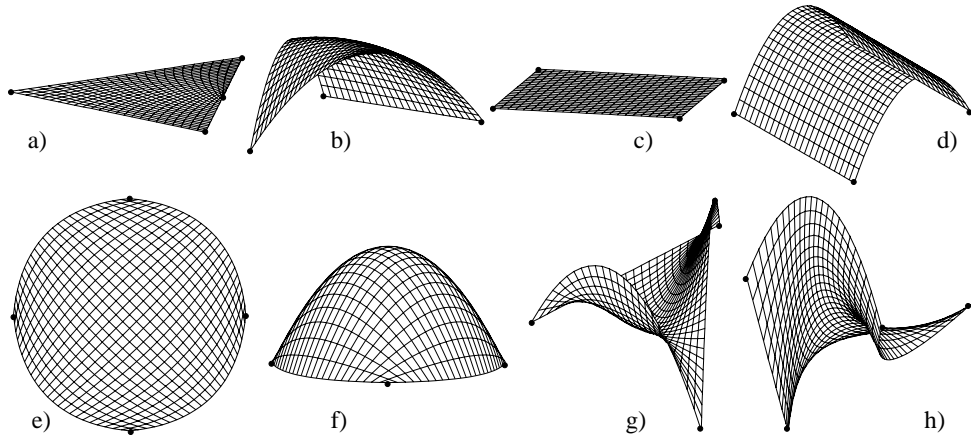


Fig. 2. One biquadratic quadrangle approximates various shapes.

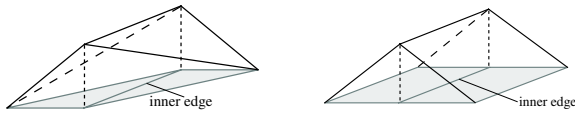


Fig. 3. Roof-top function across the common edge of two triangular (left) and rectangular (right) surface elements.

One common current representation is the Roof-Top representation which fulfills the above requirements and will be used in this contribution.

The currents on the surfaces are represented by linear functions in the local u_1, u_2 -system combining the current densities on two neighboring surface elements by placing the maximum of the current orthogonal to a common edge at the position of the common edge. Thus, the currents are approximated by linear basis functions and given by the directional derivatives of the corresponding surface element n at the position \vec{r}_n

$$\vec{F}_n(u_1, u_2) = f_{u_1} \frac{\delta \vec{r}_n}{\delta u_1} + f_{u_2} \frac{\delta \vec{r}_n}{\delta u_2}. \quad (20)$$

Here, f_{u_1} and f_{u_2} define the shape of the basis function, in the present case roof-top functions. Roof-top functions are constant in one coordinate direction (orthogonal to the current density flow) and linear triangular in the second coordinate direction. One roof-top function in the local u_1, u_2 -system is shown in Fig. 3 across the common edge of two triangular and rectangular surface elements.

In the following, only electrical surface currents are itemized, magnetic surface currents are analogous.

A. Linear Triangles and Roof-Top Basis Functions

Two linear triangles T_m^+ and T_m^- for a surface approximation are shown in Fig. 4 [5]. Their common edge is denoted m , the source positions on the triangles are \vec{r}_m^+ and \vec{r}_m^- in the global coordinate system and $\vec{\rho}_m^+$ and $\vec{\rho}_m^-$ in the local coordinate systems. The basis function \vec{j}_m' for a current

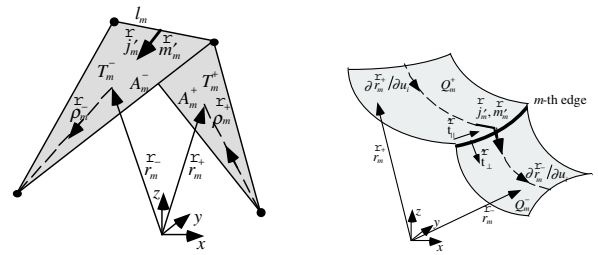


Fig. 4. Roof-Top basis functions on neighbouring surface elements: left linear triangles, and right biquadratic quadrangles.

that flows from T_m^+ to T_m^- is then

$$\vec{j}_m = \begin{cases} \frac{l_m}{2A_m^+} \vec{\rho}_m^+ & \vec{r}_m \text{ in } T_m^+ \\ \frac{l_m}{2A_m^-} \vec{\rho}_m^- & \vec{r}_m \text{ in } T_m^- \\ 0 & \text{else.} \end{cases} \quad (21)$$

The surface divergence is

$$\nabla'_S \cdot \vec{j}_m = \begin{cases} \frac{l_m}{A_m^+} & \vec{r}_m \text{ in } T_m^+ \\ -\frac{l_m}{A_m^-} & \vec{r}_m \text{ in } T_m^- \\ 0 & \text{else.} \end{cases} \quad (22)$$

B. Biquadratic Quadrangles and Roof-Top Functions

In Fig. 4 (right) the roof-top functions are shown for two neighbouring biquadratic surface elements Q_m^+ and Q_m^- . The basis functions are given for the surface current on the surface elements

$$\vec{j}_{u_1 m} = \sqrt{\frac{g_{22}(u_{1m}, u_{2m})}{g(u_1, u_2)}} T_{u_1}(u_1) P_{u_2}(u_2) \frac{\delta \vec{r}}{\delta u_1} \quad (23)$$

$$\vec{j}_{u_2 m} = \sqrt{\frac{g_{11}(u_{1m}, u_{2m})}{g(u_1, u_2)}} T_{u_2}(u_2) P_{u_1}(u_1) \frac{\delta \vec{r}}{\delta u_2}. \quad (24)$$

Here, $P_{u_{1,2}}(u_{1,2})$ is the constant function in one dimension, $T_{u_{1,2}}(u_{1,2})$ the triangular function in the other dimension

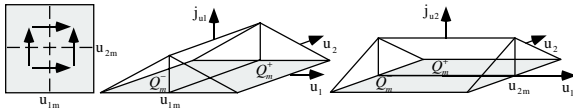


Fig. 5. Roof-Top basis functions on quadrangles in the parameter space.

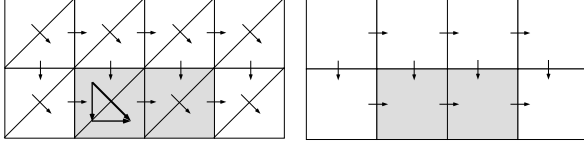


Fig. 6. Surface discretization of a rectangular plate by triangular surface elements and biquadratic rectangles.

(see Fig. 5) defined by

$$T_{u_{1,2}}(u_{1,2}) = \begin{cases} \frac{1}{2} + \frac{1}{2}u_{1,2} & \text{for } u_{1,2m} = +1 \\ \frac{1}{2} - \frac{1}{2}u_{1,2} & \text{for } u_{1,2m} = -1 \end{cases} \quad (25)$$

This ensures that no normal component is present at outer edges.

C. Comparison of linear triangles and biquadratic quadrangles

Fig. 6 shows the discretization and possible currents on a rectangular plate discretized by triangular and rectangular surface elements. Gray surface elements are situated at the border of the plate being a discontinuity of the plate. The physical current normal to the border has to vanish, hence, the current must be oriented parallel to the edge.

The current on triangular functions yields two components that are oriented orthogonally and parallel to the edge, hence an unphysical surface current close to the border exists. In other words, a constant current along the border is not accessible to linear triangles. To remedy this, the biquadratic approximation accurately models a constant current parallel to an outer edge as well as the normal component.

This will be shown with the following example. Consider a flat rectangular plate with size $1.5\lambda \times 0.7\lambda$ along the x -axis and the y -axis, respectively. A plane wave at $f = 150$ MHz is incident normally with the \vec{E} -vector along the longer side of the plate or the x -direction.

Fig. 7 shows the x -polarized current density $\|J_x\|$, or co-polarized in the direction of the E vector. The figure on the left shows the current modeled by linear triangles, and the figure on the right shows the the biquadratic quadrangles. Both approximations seem to model quite closely the physical current densities.

A different picture is seen for the y -polarized, or cross-polarized, surface current densities $\|J_y\|$ in Fig. 8. The differences between the results for the triangular and the biquadratic surface elements are clearly seen at the borders of the plate at $y = \pm 0.7$ m. The triangles cause a current

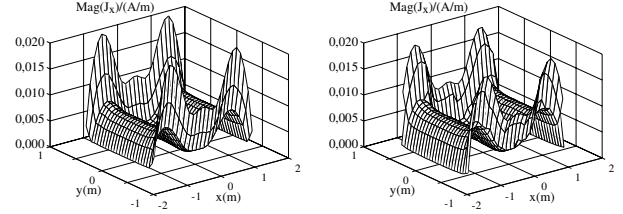


Fig. 7. x -polarized surface current densities of a rectangular plate by triangular surface elements (left) and biquadratic rectangles (right).

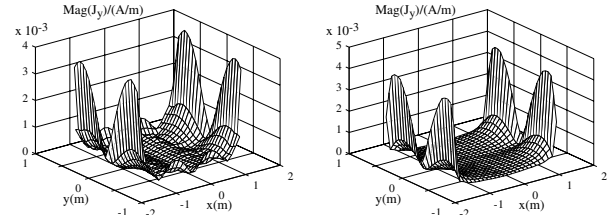


Fig. 8. y -polarized surface current densities of a rectangular plate by triangular surface elements (left) and biquadratic rectangles (right).

density orthogonal close to the edges ± 0.7 m. Even though the current magnitude only reaches approximately 25 %, these currents are nonphysical and result in a higher than physical reflection. As discussed above, the linear triangles are not able to model the correct physical current densities (see Fig. 6).

Figure 9 shows the phase of the y -polarized surface current densities (orthogonally polarized to the incident wave). The figure on the left shows the phase obtained by the linear triangular approximation. The phase exhibits large steps that are no multiple phase shifts of 360° . The figure on the right shows the smooth phase obtained by the biquadratic quadrangles with the correct physical phase

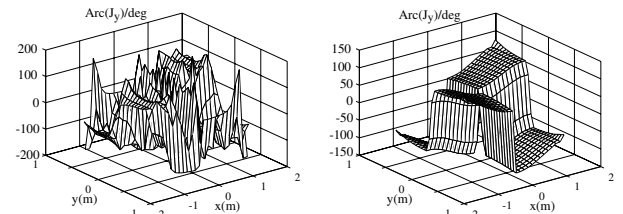


Fig. 9. Phase of the y -polarized surface current densities of a rectangular plate by triangular surface elements (left) and biquadratic rectangles (right).

TABLE I
SPURIOUS MODES AT FREQUENCY f IN MHz OF A SPHERE WITH
RADIUS $r = 1$ m. MODES ARE DENOTED BY p AND n .

p							
n	1	2	3	4	5	6	7
1	214	275	333	390	446	502	556
2	369	434	497	558	619	678	736
3	520	587	654	...			

behavior over the complete plate. Biquadratic quadrangles are, hence, much better suited to model edges of scatterers than linear triangles. This holds for both flat objects as well as three-dimensional objects with a non-negligible thickness.

In the following, the radar cross section of a smooth 3D scatterer is computed, and the results of different approximations will be compared.

IV. MONOSTATIC RADAR CROSS SECTION OF A SPHERE

A. Canonical Problem: Sphere

The canonical shape “sphere” has been chosen to analyze the capabilities of the discretization schemes. The specific advantage of the sphere is the fact that an analytical solution exists for the radar cross section. By comparing the numerical results to the results of the Mie solution [10] a simple and accurate benchmark exists.

For the present contribution, a sphere with radius 1 m is chosen, the geometrical surface area of the sphere is hence 4π m². The origin of the sphere is at the origin of the spherical co-ordinate system.

Numerical solutions by the EFIE or MFIE solely are known to suffer from spurious modes. These spurious modes occur at frequencies where the interior problem (the hollow sphere) exhibits eigen modes. For the sphere with a radius of 1 m, some of the frequencies are shown in table I. At these frequencies, the solution of EFIE or MFIE methods may show erroneous results.

B. Possible Meshing Schemes

Linear triangles linearly interpolate the scatterer’s surface which is modelled by flat surface elements. For an accurate surface modelling, very small discretization elements should be chosen. For comparison purposes, three different discretization schemes for linear triangles are used in the remainder.

A first discretization scheme is obtained by discretizing the sphere directly. No symmetry or any other special property of the sphere is taken into account. Two discretization levels produce two meshes, denoted by $a1$ and $a2$, with 288 and 2586 triangles and 432 and 3879 unknowns, respectively.

One possibility to improve the accuracy especially for symmetric objects as spheres is to impose a symmetric mesh for the object. For one particular incidence and a given co-ordinate system, an electric and magnetic symmetry according to the symmetry of both the object and

the incident field with respect to the co-ordinate system helps to increase the accuracy. However, for a general application, electric and/or magnetic symmetries are not available as the symmetry changes with direction of incidence. In this paper, a geometrical symmetry for the object is observed, hence the mesh was modified to include this symmetry by meshing one eighth of the sphere and using symmetry for the remaining seven eighths of the sphere (scheme b). Again, two meshes are produced, the first (scheme $b1$) with 352 triangles and 528 unknowns for the complete sphere, the finer mesh (scheme $b2$) with 2688 triangles and 4032 unknowns.

The third scheme follows a common way to improve results obtained by linear triangles: the surface areas of the model (e.g. the surface of all triangles) and the geometrical body are compared. Then the triangles are scaled to obtain an area that is as close as possible to the original one. This is only possible for canonical shapes as e.g. spheres, cylinders, or rectangular bodies as usually the surface of the geometrical body is not accessible to the modeller. In the present case, the two meshes $c1$ and $c2$ have 352 and 2688 triangles with 528 and 4032 unknowns, respectively.

In the case of biquadratic quadrangles, the reference points for each discretization element are chosen on the surface of the scatterer. Due to the inherent conformal shape of the discretization elements, the surface is very closely modelled. Only one mesh, scheme d , will be represented here. No attempt was made to include symmetry. This mesh uses 216 mesh elements with an average surface of 0.0582 m² or $\lambda^2/69$ for each surface patch. The mesh results in 432 unknowns that represent the electric current densities on the scatterer.

The meshing schemes are summarized in Table II.

C. Angle of Incidence Sweep for PEC Sphere

At first, the monostatic radar cross section of a perfect electric conducting sphere is computed. A plane wave with $f = 150$ MHz, $\lambda = 2$ m is incident, at this frequency the sphere’s diameter is one wavelength. The computed frequency is well below the first eigen frequency, the EFIE computation does, hence, not suffer from any discernable contributions of a spurious mode. The analytical value of the monostatic radar cross section $RCS_{\text{Mie}} = 3.7894$ dBsm is calculated by the Mie-series [10]. In all figures, the analytical value is represented by a straight line with no markers.

The angle of incidence is computed at 46 discrete angles of $\theta = 0^\circ$ to $\theta = 90^\circ$ with an increment of $\delta\theta = 2^\circ$. The first incidence is with $\vec{k} = -\vec{e}_x$, the last with $\vec{k} = -\vec{e}_y$. After having meshed the sphere, neither the mesh is modified, nor is the sphere rotated. This is to test the accuracy of the computation when the wave is incident in different directions with respect to the vertices of the mesh. Of course, the result should not change with the incident angle.

In Fig. 10, the monostatic radar cross section is shown for the discretizations $a1$ and $a2$. The marked lines show

TABLE II
MESHING SCHEMES USED FOR THE COMPUTATIONS.

scheme	surface elements	property
<i>a</i>	triangular	mesh points are chosen on geometrical surface
<i>b</i>	triangular	mesh as <i>a</i> , but also includes geometrical symmetry
<i>c</i>	triangular	mesh as <i>b</i> , additionally the total surface area of triangles is scaled to match the surface area of the sphere
<i>d</i>	biquadratic	mesh points are chosen on geometrical surface without taking into account symmetry

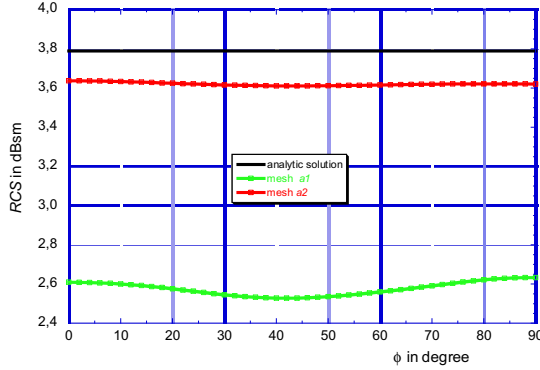


Fig. 10. Monostatic RCS of a PEC sphere computed for different angles of incidence. The sphere is meshed by 288 and 2586 linear triangles according scheme *a*.

the computed radar cross section for the two meshes. For mesh *a1*, the computed radar cross section has a minimum and maximum value of $RCS_{\min,a1} = 2.5282$ dBsm and $RCS_{\max,a1} = 2.6335$ dBsm for an average level of $RCS_{\text{ave},a1} = 2.5766$ dBsm. The amplitude $RCS_{\max,a1} - RCS_{\min,a1}$ is $\Delta RCS_{a1} = 0.105$ or 4.1 %. The absolute deviation from the analytical value is 32 %. Mesh *a2* yields more accurate values of $RCS_{\min,a2} = 3.611$ dBsm, $RCS_{\max,a2} = 3.637$ dBsm, $RCS_{\text{ave},a2} = 3.621$ dBsm, and $\Delta RCS_{a2} = 0.026$ or 0.72 %, respectively. The absolute error to the analytical value is 4.45 %. At a frequency of $f = 150$ MHz, each triangle has a surface of at most $\lambda^2/90$.

Fig. 11 shows the results for meshes *b1* and *b2*. For *b1*, the radar cross section has a minimum and maximum value of $RCS_{\min,b1} = 2.664$ dBsm and $RCS_{\max,b1} = 2.848$ dBsm, respectively, for an average of $RCS_{\text{ave},b1} = 2.750$ dBsm. The amplitude is $\Delta RCS_{b1} = 0.184$ or 6.7 %, the absolute deviation to the analytical value is only 27 %. Mesh *b2* yields $RCS_{\min,b2} = 3.643$ dBsm, $RCS_{\max,b2} = 3.660$ dBsm, $RCS_{\text{ave},b2} = 3.649$ dBsm, and $\Delta RCS_{b2} = 0.018$ or 0.48 %, respectively. The absolute error compared to the analytical value is 3.7 %. In conclusion, taking the symmetry of the scatterer into account increases slightly the accuracy of the computation. Still, many triangles and, hence, unknowns are necessary to obtain results that appear acceptable.

The meshes *c1* and *c2* yield results that are shown in Fig.

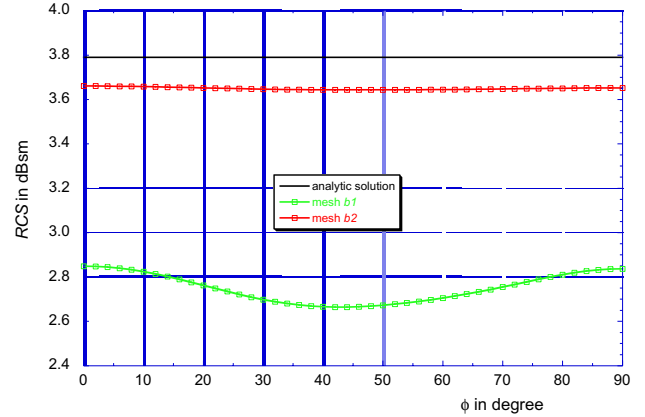


Fig. 11. Monostatic RCS of a PEC sphere computed for different angles of incidence. The sphere is meshed by 352 and 2688 linear triangles, the mesh includes the symmetry of the sphere according to scheme *b*.

12. They are found to be of much better agreement with the analytical value than the above results. In particular, mesh *c1* yields in a computed radar cross section with a minimum value and a maximum value of $RCS_{\min,c1} = 3.535$ dBsm and $RCS_{\max,c1} = 3.709$ dBsm, respectively, for a mean level of $RCS_{\text{ave},c1} = 3.611$ dBsm. The difference $RCS_{\max,c1} - RCS_{\min,c1}$ is hence $\Delta RCS_{c1} = 0.174$ or 4.8 %. The absolute deviation to the analytical value is only 4.7 % indicating that the accurate representation of the actual surface of the scatterer is important. Mesh *c2* yields slightly more accurate values of $RCS_{\min,c2} = 3.763$ dBsm, $RCS_{\max,c2} = 3.780$ dBsm, $RCS_{\text{ave},c2} = 3.769$ dBsm, and $\Delta RCS_{c2} = 0.017$ or 0.46 %, respectively. Again, the absolute error to the analytical value is 0.54 %. It is, hence, obvious from the data that an accurate geometrical approximation including symmetry and surface of the scatterer is necessary for good computational results, especially when highly accurate radar cross sections are computed.

Finally, the sphere is meshed by the biquadratic surface elements according to scheme *d*. The computed radar cross section, also shown in Fig. 12, is with a very good agreement with the analytical value with an error of only 1.5 %. The computed RCS has minimum and maximum values, average and error are $RCS_{\min,d} = 3.721$ dBsm, $RCS_{\max,d} = 3.743$ dBsm, $RCS_{\text{ave},d} = 3.733$ dBsm, and $\Delta RCS_d = 0.0213$ or 0.57 %, respectively. It is noted that for the triangular meshes only the one with symmetry and

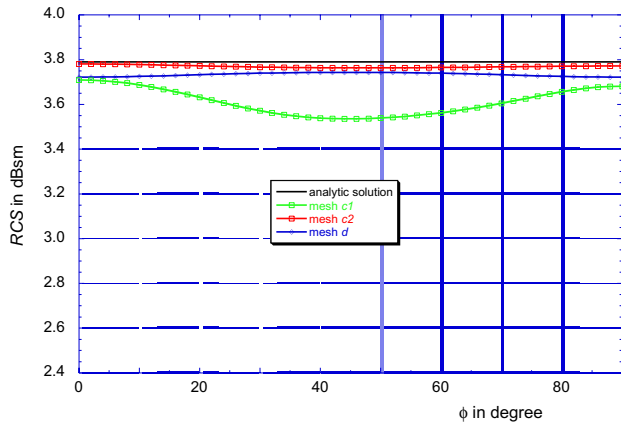


Fig. 12. Monostatic RCS of a PEC sphere computed for different angles of incidence. The sphere is meshed by 352 and 2688 linear triangles with a mesh that includes symmetry, the total surface of the triangles corresponds to the sphere's surface according to scheme c. Additionally, the sphere is meshed by a biquadratic mesh that has 216 biquadratic rectangles according to scheme d.

a geometric scaling for the actual surface yields better results, with a high cost of 4032 unknowns.

Table III concludes of the meshing schemes, the amplitudes of the computed *RCS* values, the average *RCS*-values and the errors.

D. Frequency Sweep for a PEC Sphere

Next is a frequency sweep of the above sphere for a plane wave incident with $\vec{k} = -\vec{e}_x$. The mesh is left unmodified for the frequencies from $f_1 = 100$ MHz to $f_u = 500$ MHz. The results for meshes *c1*, *c2* and *d* are reproduced. The sizes of the surface elements in terms of squared wavelengths for the frequencies $f = 300$ MHz and $f = 500$ MHz are shown in Tab. IV together with the absolute values..

Fig. 13 shows the radar cross section of the three numerical schemes in comparison with the analytical MIE solution. It is seen that the coarse mesh *c1* yields, over the complete frequency range, results that do not correspond well to the analytical values. The fine mesh *c2* with 4032 unknowns results in radar cross section values that are still far away from the analytical solution, but better than the smaller mesh for frequencies of up to $f \approx 250$ MHz. Starting from $f \approx 300$ MHz, the two curves deviate from each other. The triangular mesh shows erroneous results at frequencies around $f \approx 390$ MHz which is close to the inner resonance frequency $p = 1, m = 4$ of the sphere. The mesh with the biquadratic quadrangles is on the analytical curve for frequencies up to $f \approx 500$ MHz.

The mesh using triangular discretization cells yields accurate results only for cell sizes areas that are smaller than $\lambda^2/90$. In contrast, the biquadratic quadrangles yield still accurate results for large cells comparable to $\lambda^2/10$. Hence, less cells can be used to discretize a scatterer resulting in smaller problem sizes with higher accuracy.

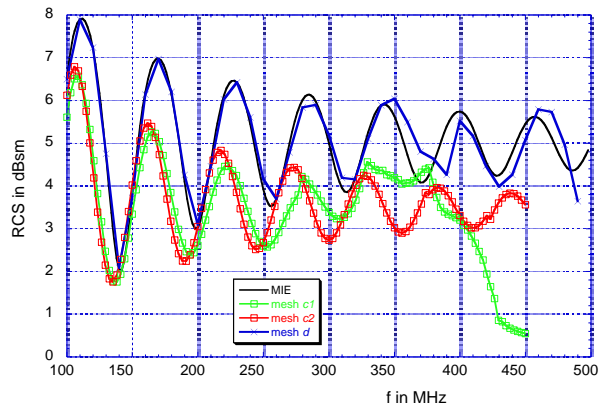


Fig. 13. RCS of a perfect conducting sphere. Triangular mesh with 352 and 2688 elements in comparison with 216 biquadratic quadrangles and the theoretical values.

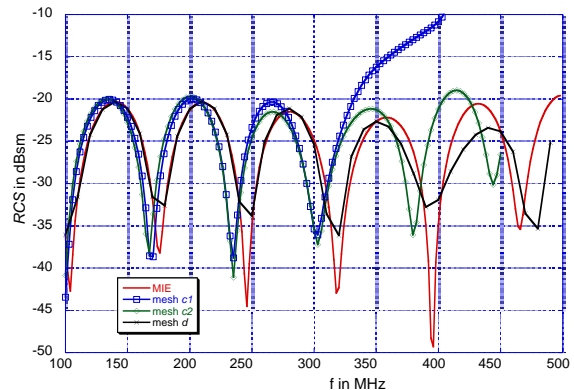


Fig. 14. RCS of a sphere with a low dielectric contrast, $\epsilon_r = 1.1$.

E. Frequency Sweep for a Low Contrast Sphere

With the same meshes as previously, the radar cross section of a dielectric sphere with a very low contrast of $\epsilon_r = 1.1$ is computed. This case is especially difficult to model numerically as the contrast is very low.

Mesh *c1* and *c2* yield both results that are not accurately modelling the zeros of the frequency response. The average level still corresponds to the average level of the analytic Mie results. Mesh *c1* yields completely wrong results starting at 300 MHz, whereas mesh *c2* somewhat follows the analytic values up to a frequency of 400 MHz.

Mesh *d* together with the complete PMCHW formulation yields the results in Fig. 14 compared to the analytic results. The numerical solution follows the analytic solution up to a frequency of about 350 MHz.

V. CONCLUSIONS

For accurate numerical solutions by boundary element methods applied to scattering problems, two main issues should be considered carefully: the geometrical approximation of the surface of the scatterer and the numerical approximation of the physical quantity on the boundary.

TABLE III

AMPLITUDE AND AVERAGE RCS COMPUTED BY THE MESHING SCHEMES IDENTIFIED IN TABLE II FOR A SPHERE OF RADIUS 1 m. ANALYTICAL VALUE IS $RCS_{MIE} = 3.789$ dBsm.

Mesh	# unknowns	Amplitude ΔRCS /dBsm	Average RCS_{ave} /dBsm	error in %
<i>a</i> 1	432	0.105	2.58	32
<i>a</i> 2	3879	0.026	3.62	4.5
<i>b</i> 1	528	0.184	2.75	27
<i>b</i> 2	4032	0.018	3.49	3.7
<i>c</i> 1	528	0.174	3.61	4.7
<i>c</i> 2	4032	0.017	3.77	0.5
<i>d</i>	432	0.021	3.73	1.5

TABLE IV

AVERAGE DISCRETIZATION CELL SIZES NORMALIZED TO SQUARED WAVELENGTH FOR THE THREE MESHING SCHEMES.

scheme	type	no. of cells	average size in m^2	$f = 300$ MHz	$f = 500$ MHz
<i>c</i> 1	triangular	352	$a_{c1} = 38.7 \cdot 10^{-3}$	$\lambda^2/26$	$\lambda^2/9$
<i>c</i> 2	triangular	2688	$a_{c2} = 5.14 \cdot 10^{-3}$	$\lambda^2/194$	$\lambda^2/70$
<i>d</i>	biquadratic	216	$a_d = 58.2 \cdot 10^{-3}$	$\lambda^2/34$	$\lambda^2/6$

Utilizing linear triangles has the advantage of simple meshing algorithms, the ability to model almost any surface and the relatively simple mathematical formulation. The limits of the linear triangles show up when currents close to edges or borders must be computed: a non-physical solution may result. Also, as it is necessary to mesh the geometrical surface area as close as possible by the approximation, accurate results may only be obtained when the surface area of the numerical model is scaled to match the surface area of the physical problem.

Biquadratic quadrangles are somewhat more difficult to be described mathematically. They need more surface points for discretization, but yield a much more accurate description of the physical problem. This results in fewer surface elements and consequently less unknowns in the numerical formulation. The present contribution also has shown that a formulation founded on biquadratic quadrangles may use considerably larger elements compared to a formulation based on linear triangles with the same numerical accuracy.

REFERENCES

- [1] R. F. Harrington, *Field Computation by Moment Methods*. New York: The Macmillan Company, 1968.
- [2] A. J. Poggio and E. K. Miller, "Integral equation solutions of three-dimensional scattering problems," in *Computer Techniques for Electromagnetics* (R. Mittra, ed.), New York, NY, USA: Pergamon Press, 1973.
- [3] A. Herschlein, *Entwicklung numerischer Verfahren zur Feldberechnung konformer Antennen auf Oberflächen höherer Ordnung* (in German). PhD thesis, Institut für Höchstfrequenztechnik und Elektronik, Universität Karlsruhe, 2002.
- [4] A. Herschlein, J. von Hagen, and W. Wiesbeck, "A generalized integral equation formulation for mixed-dielectric-PEC-scatterers," *Radio Science*, vol. 37, no. 4, pp. 11-1 - 11-15, 2002.
- [5] S. M. Rao, D. R. Wilton, and A. W. Glisson, "Electromagnetic

scattering from surfaces of arbitrary shape," *IEEE Trans. on Ant. and Prop.*, vol. 30, pp. 409-418, May 1982.

- [6] G. Kang, J. Song, W. C. Chew, K. C. Donepudi, and J.-M. Jin, "A novel grid-robust higher order vector basis function for the method of moments," *IEEE Trans. on Ant. and Prop.*, vol. 49, pp. 908-915, June 2001.
- [7] J. M. Song and W. C. Chew, "Moment method solutions using parametric geometry," *J of Electromagnetic Waves and Applications*, pp. 71-83, Jan. 1995.
- [8] J. Dominguez, *Boundary Elements in Dynamics*. London: Computational Mechanics Publications, Elsevier Applied Science, 1993.
- [9] A. Herschlein, J. von Hagen, and W. Wiesbeck, "Methods for the evaluation of regular, weakly singular and strongly singular surface reaction integrals arising in method of moments," *ACES Journal*, vol. 17, *Special Issue on: Approaches on better Accuracy/Resolution in CEM*, pp. 63-73, Mar. 2002.
- [10] G. Mie, "Beiträge zur Optik trüber Medien, speziell kolloidaler Metallösungen," *Annalen der Physik*, vol. 4, no. 25, 1908.



Alexander Herschlein received the Dipl.-Ing. (M.S.E.E.) and the Dr.-Ing. (Ph.D.E.E.) degrees from the University of Karlsruhe, Germany, in 1993 and 2002, respectively. From 1994 to 2002, he was with the Institut für Höchstfrequenztechnik und Elektronik (IHE), University of Karlsruhe. As a research assistant at the IHE, he was responsible for lectures in antennas and antenna systems. His research responsibilities during this period included field theory, numerical methods, optimisations, wave propagation, antennas and EMC. 1998 and 1999, he also worked for the DaimlerChrysler AG, Research Center Ulm, Germany.

Since 2003, he has been with EADS-Astrium in Friedrichshafen, Germany, engaged in microwave system engineering. He is the head of the antenna laboratory, responsible for antenna designs and optimisations, RF test definitions and RF measurements. His main topic is the optimisation of the active TerraSAR-X antenna and he is the leader of the measurement campaign of this phased array.



Jürgen v. Hagen received the Dipl.-Ing. (M.S.E.E) and the Dr.-Ing. (Ph.D.E.E.) degrees from the University of Karlsruhe (TH) in 1994 and 1997, respectively. From 1994 to 1997 he was working with the CNRS (Comité National de la Recherche Scientifique), France on electromagnetic compatibility. In 1998 he held a postdoctoral position at the Electromagnetics Research Laboratory at the Pennsylvania State University, in State College, PA, USA. 1999 until 2001 he was with the Institut für Höchstfrequenztechnik und Elektronik (IHE) at the Universität Karlsruhe (TH), Germany where he was lecturer responsible for planar and conformal antennas as well as numerical techniques in electromagnetics and research assistant for industrial applications of microwaves, microwave heating processes, and EMC. He is now with DaimlerChrysler AG, Sindelfingen, responsible for broadcast reception systems, and continues to teach microstrip and planar antennas at the University of Karlsruhe.

His research interests other than his current professional area are electromagnetic theory, numerical techniques including frequency and time domain techniques, planar and conformal antennas, industrial applications of microwave power, and automotive sensors.

Dr. v. Hagen is member of IEEE, ACES, and VDE.

Carl Cranz Series for Scientific Education he serves as a permanent lecturer for radar system engineering, wave propagation and mobile communication network planning. He is a member of an Advisory Committee of the EU - Joint Research Centre (Ispra/Italy), and he is an advisor to the German Research Council (DFG), to the Federal German Ministry for Research (BMBF), and to industry in Germany. He is recipient of a number of awards, lately the IEEE Millennium Award, and the IEEE GRS Distinguished Achievement Award. He is a Fellow of IEEE, a Member of the Heidelberger Academy of Sciences and a Member of acatech (German Academy of Engineering and Technology).



Dietmar Löffler received the Dipl.-Ing. (M.S.E.E.) and the Dr.-Ing. (Ph.D. E.E.) degrees from the University of Karlsruhe (TH), Germany in 1995 and 2001, respectively. From 1995 to 2001 he was working with the Institut für Höchstfrequenztechnik und Elektronik (IHE) at the University of Karlsruhe, Germany on wave propagation, microstrip circuits and conformal antennas used for radar and communication applications. For the Carl-Cranz-Gesellschaft (CCG), Germany, he served as a lecturer of the courses "Radar System Engineering" and "Smart Antennas".

In 2001 he joined the LS Telcom AG, Lichtenau, Germany, where he currently is the head of the broadcasting department. His research interests are digital broadcast systems in the short wave range, digital television system in the VHF/UHF bands as well as wave propagation within the broadcasting bands.

Dr. Löffler is a member of VDE.



Werner Wiesbeck received the Dipl.-Ing. (M.S.E.E.) and the Dr.-Ing. (Ph.D.E.E.) degrees from the Technical University Munich in 1969 and 1972, respectively. From 1972 to 1983 he was with AEG-Telefunken in various positions including that of head of R&D of the Microwave Division in Flensburg and marketing director Receiver and Direction Finder Division, Ulm. During this period he had product responsibility for mm-wave radars, receivers, direction finders and electronic warfare systems. Since 1983 he has been director of the Institut für Höchstfrequenztechnik und Elektronik (IHE) at the University of Karlsruhe (TH), where he had been dean of the Faculty of Electrical Engineering. Research topics include radar, remote sensing, wireless communication and antennas. In 1989 and 1994, respectively, he spent a six month sabbatical at the Jet Propulsion Laboratory, Pasadena. He is a member of the IEEE GRS-S AdCom (1992 - 2000), Chairman of the GRS-S Awards Committee (1994 - 1998, 2002 -), Executive Vice President IEEE GRS-S (1998 - 1999), President IEEE GRS-S (2000 - 2001), Associate Editor IEEE-AP Transactions (1996-1999), past and present Treasurer of the IEEE German Section (1987-1996, 2003-2005). He has been General Chairman of the '88 Heinrich Hertz Centennial Symposium, the '93 Conference on Microwaves and Optics (MIOP '93), the Technical Chairman of International mm-Wave and Infrared Conference 2004 and he has been a member of the scientific committees of many conferences. For the

A Modified LU Recombination Technique for Improving the Performance of Boundary Element Methods at Low Frequencies

Haixin Ke and Todd H. Hubing
 Department of Electrical and Computer Engineering
 University of Missouri-Rolla
 Rolla, MO 65409

ABSTRACT

Many numerical electromagnetic modeling techniques that work very well at high frequencies do not work well at lower frequencies. This is directly or indirectly due to the weak coupling between the electric and magnetic fields at low frequencies. One technique for improving the performance of boundary element techniques at low frequencies is through the use of loop-tree basis functions, which decouple the contributions from the vector and scalar electric potential. However, loop-tree basis functions can be difficult to define for large, complex geometries. This paper describes a method for improving the low-frequency performance of boundary element techniques that does not require the explicit definition of loop-tree basis functions. The method is a modified version of an LU recombination method proposed earlier. It automatically detects the linear space spanned by the scalar electric potential and corrects numerical errors during the LU decomposition of the impedance matrix. This method does not require special basis functions and is relatively easy to implement. Several examples are presented to demonstrate the effectiveness of this method.

I. INTRODUCTION

The boundary element method is a widely used numerical electromagnetic modeling technique. Boundary element modeling codes use the method of moments to solve an electric field integral equation (EFIE) or magnetic field integral equation (MFIE) to calculate equivalent currents induced on a surface in the presence of an exciting field. There are many boundary element modeling codes available that do an excellent job of modeling complex geometries at high frequencies (megahertz and higher). At low frequencies however, these codes may exhibit instabilities, particularly when using general purpose basis functions such as the popular Rao-Wilton-Glisson (RWG) [1] basis functions [2, 3, 4]. These instabilities can be explained in terms of the natural Helmholtz decomposition of Maxwell's equations [5]. At low

frequencies, the magnetic vector potential and the electric scalar potential become more decoupled. Their representations in the impedance matrix become heavily imbalanced [3, 6, 7] and this imbalance results in the loss of important information due to the finite precision of the numerical computations.

Loop-tree basis functions have been proposed to overcome this difficulty [3]. These basis functions allow the divergence-free and the curl-free components of the current, which have different frequency dependencies, to be separated [5]. The round-off error due to the difference in size of the scalar and vector potential contributions is avoided. Unfortunately, loop-tree basis functions are not widely used because they can be difficult to work with; particularly if the geometry being modeled is large and complex.

In [8] an LU recombination method was proposed that mathematically forced the scalar potential to be zero around loops, without explicitly defining new basis functions. It was readily applied to existing moment method algorithms. This method works well for simple structures like small loops but does not model surface currents correctly on large plates.

In this paper we present a modified LU recombination method. This method extracts the linear dependence information from the \mathbf{L} matrix and modifies both the \mathbf{L} and \mathbf{U} matrices to remove the error in the linear relations and recover the space spanned by the scalar potentials. Examples show that this method works better than the previous LU recombination method.

The rest of the paper is organized as follows: Section II explains the reason for the low-frequency errors in boundary element codes and briefly describes loop-tree basis functions; Section III introduces the new method based on LU decomposition; Section IV presents several numerical examples; and finally in Section V, we provide a brief summary.

II. LOW-FREQUENCY PROBLEM AND LOOP-TREE SCHEME

Consider the electromagnetic scattering from perfect electric conductors (PECs). The “mixed-potential” form of the scattered electric field is expressed as

$$\mathbf{E}^{sca} = -j\omega\mathbf{A} - \nabla\Phi. \quad (1)$$

The first term on the right-hand side of this equation is directly proportional to frequency while the second term is not. At low frequencies, the scalar potential term dominates.

The low frequency problem can be understood by examining the testing process [9]. A vector identity states that the integration of the gradient, $\nabla\Phi$, is path-independent. If the scatterer mesh allows current to flow in closed loops, the testing of the scalar potentials associated with the loops should cancel. If, due to numerical error, the testing of scalar potential is not exactly zero when evaluated around a closed loop, the error can overwhelm the vector potential term in (1) at low frequencies. The solution to the matrix equation then becomes unstable.

The construction of the loop-tree basis functions starts with the physical decomposition of current,

$$\mathbf{J} = \mathbf{J}^s + \mathbf{J}^i, \quad (2)$$

where \mathbf{J}^s is the solenoidal current and \mathbf{J}^i is the irrotational component. Loop basis functions are used to expand \mathbf{J}^s and tree basis functions to expand \mathbf{J}^i .

A loop basis function is associated with an inner node and its surrounding edges. Explicitly, the definition in terms of RWG basis functions is [2],

$$\mathbf{O}_n(\mathbf{r}) = \sum_{i \in \text{loop}_n} \frac{\sigma_i}{\lambda_i} \mathbf{f}_i(\mathbf{r}), \quad (3)$$

where \mathbf{f}_i is the RWG basis function for the i^{th} edge connected to node n . λ_i is the length of the edge and the coefficient $\sigma_i = \pm 1$ forces the current to flow in the same direction around node n .

Tree basis functions are simply chosen from a subset of the RWG basis functions and are complementary to the loop basis functions. It is easy to show that the loop basis functions are divergence-free. Physically, that means there is no charge associated with the loop basis functions.

The loop-tree basis function scheme inherently forces the numerical integration of $\nabla\Phi$ over closed paths to be exactly zero and preserves the

information contained in \mathbf{A} . However, to take advantage of this technique, one has to identify all possible closed paths in the mesh. This requires searching the mesh to locate the inner nodes, identifying shared edges for each inner node, and adjusting the basis functions associated with the edges to orient them properly. This procedure can be cumbersome [2].

III. THE MODIFIED LU RECOMBINATION METHOD

The modified LU recombination method described here takes advantage of the fact that the loop-tree basis functions are linear combinations of the RWG basis functions. In this method, the reordering of the impedance matrix is performed automatically without having to identify current loops explicitly.

Consider the following $N \times N$ matrix equation,

$$\mathbf{C} \cdot \mathbf{J} = \mathbf{F} \quad (4)$$

obtained after applying the method of moments using RWG basis and testing functions. $\mathbf{J} = [J_n]$ is a vector of the unknown surface current densities which are normal to the edges. $\mathbf{F} = [F_m]$ is the excitation vector. $\mathbf{C} = [C_{mn}]$ is the $N \times N$ impedance matrix. Each row of \mathbf{C} corresponds to an edge in the mesh. The elements of \mathbf{C} are given by [10],

$$\begin{aligned} C_{mn} &= C_{1mn} + C_{2mn} \\ &= jk\eta \int_{T_m} \mathbf{f}_m(\mathbf{r}) \cdot \left[\int_{T_n} \mathbf{f}_n(\mathbf{r}') \mathbf{G}_0(\mathbf{r}, \mathbf{r}') dS' \right] dS \\ &\quad + j \frac{\eta}{k} \int_{T_m} \mathbf{f}_m(\mathbf{r}) \cdot \left[\int_{T_n} (\nabla' \cdot \mathbf{f}_n(\mathbf{r}')) \nabla' \mathbf{G}_0(\mathbf{r}, \mathbf{r}') dS' \right] dS \end{aligned} \quad (5)$$

where k is the wave number and η the intrinsic impedance. \mathbf{C}_1 is the vector potential component and \mathbf{C}_2 is the scalar potential component of \mathbf{C} . The function \mathbf{f}_n is the RWG basis function defined on triangle pair T_n . T_n is composed of two triangles, T_n^+ and T_n^- , sharing edge n . \mathbf{G}_0 is the free space Green's function. \mathbf{r} and \mathbf{r}' are the observation and source points, respectively. We can write the elements of \mathbf{C}_2 , the second integral on the right of (5), as

$$\begin{aligned} C_{2mn} &= j \frac{\eta}{k} \int_{T_m^+} (\nabla \cdot \mathbf{f}_m) \left[\int_{T_n^+} (\nabla' \cdot \mathbf{f}_n) \mathbf{G}_0(\mathbf{r}, \mathbf{r}') dS' \right] dS \\ &\quad + j \frac{\eta}{k} \int_{T_m^-} (\nabla \cdot \mathbf{f}_m) \left[\int_{T_n^-} (\nabla' \cdot \mathbf{f}_n) \mathbf{G}_0(\mathbf{r}, \mathbf{r}') dS' \right] dS \\ &\quad + j \frac{\eta}{k} \int_{T_m^+} (\nabla \cdot \mathbf{f}_m) \left[\int_{T_n^-} (\nabla' \cdot \mathbf{f}_n) \mathbf{G}_0(\mathbf{r}, \mathbf{r}') dS' \right] dS \\ &\quad + j \frac{\eta}{k} \int_{T_m^-} (\nabla \cdot \mathbf{f}_m) \left[\int_{T_n^+} (\nabla' \cdot \mathbf{f}_n) \mathbf{G}_0(\mathbf{r}, \mathbf{r}') dS' \right] dS. \end{aligned} \quad (6)$$

The surface divergence of the function f_n , which is proportional to the surface charge density, is

$$\nabla \cdot \mathbf{f}_n = \begin{cases} +\lambda_n / A_n^+ & \mathbf{r} \text{ in } T_n^+ \\ -\lambda_n / A_n^- & \mathbf{r} \text{ in } T_n^- \end{cases}, \quad (7)$$

where λ is the edge length and A is the area of the triangle. Using this property and defining

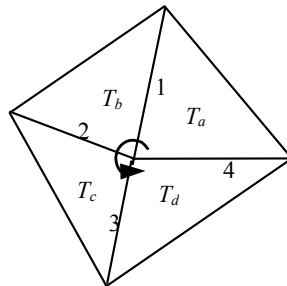
$$I(m^+, n^-) = \int_{T_m^+} \left[\int_{T_n^-} \mathbf{G}_o(\mathbf{r}, \mathbf{r}') dS' \right] dS, \quad (8)$$

(6) can be written as

$$C_{2mn} = j \frac{\eta}{k} \begin{bmatrix} \left(\frac{\lambda_m}{A_m^+} \right) \left(\frac{\lambda_n}{A_n^+} \right) I(m^+, n^+) \\ + \left(-\frac{\lambda_m}{A_m^-} \right) \left(\frac{\lambda_n}{A_n^+} \right) I(m^-, n^+) \\ + \left(\frac{\lambda_m}{A_m^+} \right) \left(-\frac{\lambda_n}{A_n^-} \right) I(m^+, n^-) \\ + \left(-\frac{\lambda_m}{A_m^-} \right) \left(-\frac{\lambda_n}{A_n^-} \right) I(m^-, n^-) \end{bmatrix}. \quad (9)$$

Suppose an inner node is surrounded by 4 triangles, T_a , T_b , T_c , and T_d and the edges shared by these four triangles are edges 1, 2, 3, and 4 as shown in Fig. 1. For simplicity, the orientations of the edges are defined to be counterclockwise. Now consider the integrals for these observation edges and a source edge n , also shown in Fig. 1.

$$C_{21n} = j \frac{\eta}{k} \begin{bmatrix} \left(\frac{\lambda_1}{A_a} \right) \left(\frac{\lambda_n}{A_n^+} \right) I(a, n^+) \\ + \left(-\frac{\lambda_1}{A_b} \right) \left(\frac{\lambda_n}{A_n^+} \right) I(b, n^+) \\ + \left(\frac{\lambda_1}{A_a} \right) \left(-\frac{\lambda_n}{A_n^-} \right) I(a, n^-) \\ + \left(-\frac{\lambda_1}{A_b} \right) \left(-\frac{\lambda_n}{A_n^-} \right) I(b, n^-) \end{bmatrix}, \quad (10.a)$$



$$C_{22n} = j \frac{\eta}{k} \begin{bmatrix} \left(\frac{\lambda_2}{A_b} \right) \left(\frac{\lambda_n}{A_n^+} \right) I(b, n^+) \\ + \left(-\frac{\lambda_2}{A_c} \right) \left(\frac{\lambda_n}{A_n^+} \right) I(c, n^+) \\ + \left(\frac{\lambda_2}{A_b} \right) \left(-\frac{\lambda_n}{A_n^-} \right) I(b, n^-) \\ + \left(-\frac{\lambda_2}{A_c} \right) \left(-\frac{\lambda_n}{A_n^-} \right) I(c, n^-) \end{bmatrix}, \quad (10.b)$$

$$C_{23n} = j \frac{\eta}{k} \begin{bmatrix} \left(\frac{\lambda_3}{A_c} \right) \left(\frac{\lambda_n}{A_n^+} \right) I(c, n^+) \\ + \left(-\frac{\lambda_3}{A_d} \right) \left(\frac{\lambda_n}{A_n^+} \right) I(d, n^+) \\ + \left(\frac{\lambda_3}{A_c} \right) \left(-\frac{\lambda_n}{A_n^-} \right) I(c, n^-) \\ + \left(-\frac{\lambda_3}{A_d} \right) \left(-\frac{\lambda_n}{A_n^-} \right) I(d, n^-) \end{bmatrix}, \quad (10.c)$$

$$C_{24n} = j \frac{\eta}{k} \begin{bmatrix} \left(\frac{\lambda_4}{A_d} \right) \left(\frac{\lambda_n}{A_n^+} \right) I(d, n^+) \\ + \left(-\frac{\lambda_4}{A_a} \right) \left(\frac{\lambda_n}{A_n^+} \right) I(a, n^+) \\ + \left(\frac{\lambda_4}{A_d} \right) \left(-\frac{\lambda_n}{A_n^-} \right) I(d, n^-) \\ + \left(-\frac{\lambda_4}{A_a} \right) \left(-\frac{\lambda_n}{A_n^-} \right) I(a, n^-) \end{bmatrix}. \quad (10.d)$$

In (10), C_{2in} is the element on the i^{th} row and n^{th} column of \mathbf{C}_2 . It is easy to show that these elements are dependent, and satisfy the following equation [8],

$$\frac{C_{21n}}{\lambda_1} + \frac{C_{22n}}{\lambda_2} + \frac{C_{23n}}{\lambda_3} + \frac{C_{24n}}{\lambda_4} = 0. \quad (11)$$

Since n can be any edge in the mesh, (11) indicates that rows 1, 2, 3, and 4 of \mathbf{C}_2 are linearly

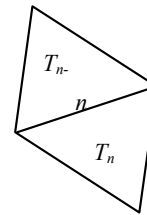


Figure 1. Source and observation triangles.

\mathbf{C}_2 in Equation (5) is singular if closed loops exist in the mesh. The rows forming a loop are linearly dependent as shown in (11) and we can write them in a form similar to (13),

$$\left(\frac{\mathbf{C}_{21}}{\lambda_1}\right) = (\pm a)\left(\frac{\mathbf{C}_{22}}{\lambda_2}\right) + (\pm b)\left(\frac{\mathbf{C}_{23}}{\lambda_3}\right) + (\pm c)\left(\frac{\mathbf{C}_{24}}{\lambda_4}\right) \quad (18)$$

where $\frac{\mathbf{C}_{2i}}{\lambda_i}$ is the i^{th} row of \mathbf{C}_2 normalized by the edge length. Comparing (18) to (11), it is clear that the coefficients a , b , and c should be either 1 or -1 . It is not difficult to rearrange the edges in the mesh so that the LU decomposition of \mathbf{C}_2 can be written as in (15). If we fill (17) with the \mathbf{L} matrix and solve the equation, the solution \mathbf{R} should be a vector with integer elements. The non-zero integers correspond to edges forming a loop with one of the dependent edges, and zero values correspond to edges not related to the loop. The numerical solution will not be exact. However, it is accurate enough for us to identify all the integers. So we can determine the edges forming a loop and how they are related. Moreover, we can replace the elements in the solution with the exact values of the integers and recalculate \mathbf{L}_{di} using (17). This modification, together with the modification of \mathbf{U} , not only makes those rows dependent but also corrects their linear relation and recovers the scalar potential space.

In practice, we decompose \mathbf{C}_2 in the form,

$$\mathbf{C}_2 = \mathbf{L} \cdot \mathbf{U} \cdot \mathbf{L}' \quad (19)$$

where \mathbf{L} is the lower triangular matrix resulting from an LU decomposition. Since \mathbf{C}_2 is symmetric, the \mathbf{U} matrix in (19) is also symmetric and \mathbf{U} is still partitioned into four parts as in (15). \mathbf{U} can then be modified by setting \mathbf{U}_{di} , \mathbf{U}_{id} , and \mathbf{U}_{dd} to zero. In this manner, we make all modifications symmetrically thus maintaining the symmetric property of the new \mathbf{C}_2 matrix.

After the LU recombination, the errors in \mathbf{C}_2 are eliminated and the information from \mathbf{C}_1 is preserved. This can be seen from the equation below.

$$\begin{aligned} \mathbf{C} &= \mathbf{C}_1 + \mathbf{C}_2 = \mathbf{L}\mathbf{D}\mathbf{L}' + \mathbf{L}\mathbf{U}\mathbf{L}' \\ &= \mathbf{L} \left(\begin{bmatrix} \mathbf{D}_{ii} & \mathbf{D}_{id} \\ \mathbf{D}_{di} & \mathbf{D}_{dd} \end{bmatrix} + \begin{bmatrix} \mathbf{U}_{ii} & \mathbf{U}_{id} \\ \mathbf{U}_{di} & \mathbf{U}_{dd} \end{bmatrix} \right) \mathbf{L}', \end{aligned} \quad (20)$$

where \mathbf{L} and \mathbf{U} are the same as in (19). \mathbf{D} is a matrix such that $\mathbf{C}_1 = \mathbf{L} \cdot \mathbf{D} \cdot \mathbf{L}'$. \mathbf{U}_{di} , \mathbf{U}_{id} , and \mathbf{U}_{dd} are set to zero in the recombination. Their counterparts, \mathbf{D}_{di} , \mathbf{D}_{id} , and \mathbf{D}_{dd} , however, are so small that the new \mathbf{C} is still poorly conditioned when summing up \mathbf{D}

and \mathbf{U} . In previously described loop-tree schemes, the frequency scaling property of the operators was analyzed and frequency normalization was applied to the elements of the EFIE matrix [5, 6]. In the modified LU recombination method we reduce the imbalance between the magnitudes of the matrix elements by scaling the vector potential part, that is, the sub matrices \mathbf{D}_{di} , \mathbf{D}_{id} , and \mathbf{D}_{dd} in (20). This scaling is based directly on the magnitudes of the elements in \mathbf{C}_1 and \mathbf{C}_2 rather than on the frequency dependence. In our examples, this greatly improves the condition of the \mathbf{C} matrix.

IV. NUMERICAL RESULTS

We applied a boundary element method employing RWG basis functions, the LU recombination method, and the modified LU recombination method to the analysis of the square loop circuit shown in Figure 2. The circuit has a voltage source and a resistive load. The mesh has 74 edges and 10 inner nodes. Since the circuit itself is a loop, there are 11 loops in this mesh and there are 11 dependent rows in the \mathbf{C}_2 matrix. Figure 3 shows the current through the load calculated by each of the three methods. Both the LU recombination method and the modified method calculate the current correctly down to frequencies as low as 1 Hz while the standard RWG method exhibits significant errors below 80 MHz.

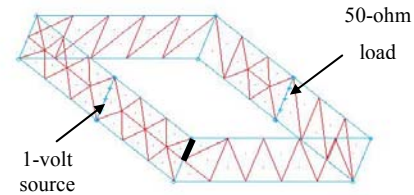


Figure 2. Mesh used to model a square loop circuit.

Figure 4 shows the current on another edge, indicated by the thick line in Figure 2. The current on this edge can be divided into two parts, one is the actual current flowing around the loop, and the other is an artificial current circling the inner node. The old LU recombination method exhibits errors below 10 kHz due to the artificial currents, but the modified method works well as low as 1 Hz.

Figure 5 shows a simple electric dipole antenna with a voltage source on the center edge. From the mesh we can see that the source edge is not part of any loop. Figure 6 compares this current through this edge calculated by the three methods. The LU recombination method fails for this example,

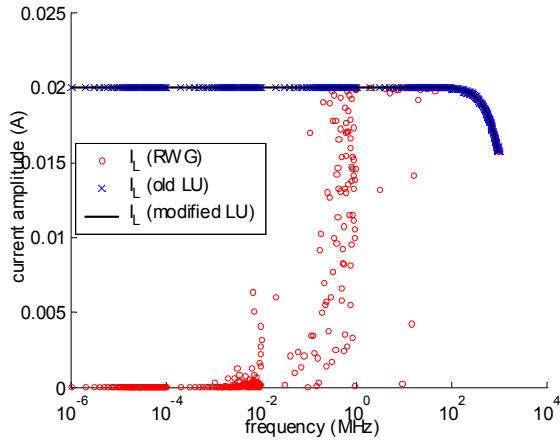


Figure 3. Current on the load edge of the loop circuit.

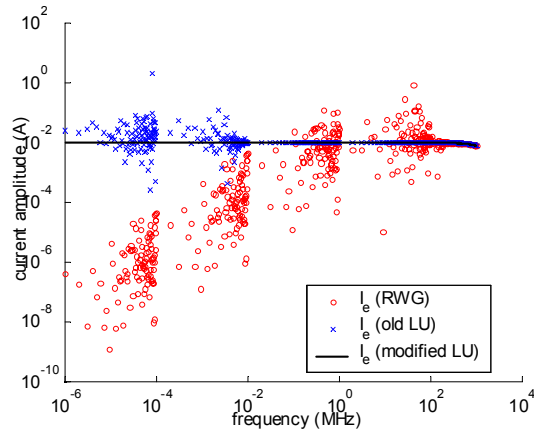


Figure 4. Current on a single edge of the loop circuit.

while both the standard RWG method and the modified method work fine. Figure 7 compares the current on another edge, indicated in Figure 5 by a thick line. In this case only the modified LU recombination method yields stable results below a few MHz.

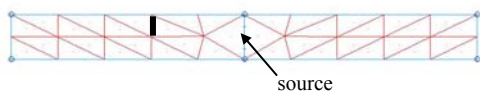


Figure 5. Mesh used to model a short dipole.

The dipole has a relatively simple mesh. We can readily observe how loops are formed around inner nodes in Figure 5, so it is relatively straightforward to implement the loop-tree scheme for this example. Figure 8 compares the current calculated by the modified LU recombination method to the current obtained using a loop-tree scheme. The results of the two methods match very well. The

unstable results at frequencies below 100 Hz are due to the significant imbalance in the scale of the vector and scalar potential terms. When we scale up the vector potential, the new method yields good results down to a few Hz, as shown in Figure 7.

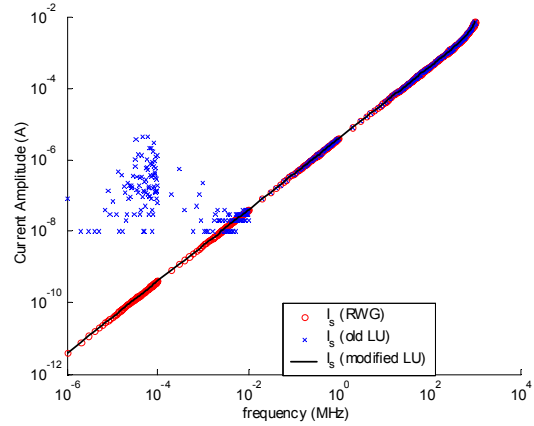


Figure 6. Current on the source edge of the dipole.

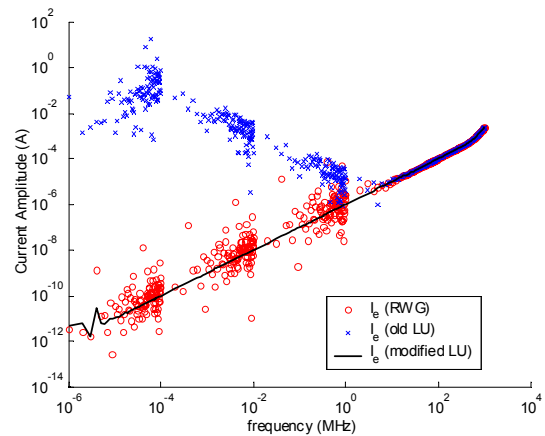


Figure 7. Current on a single edge of the dipole.

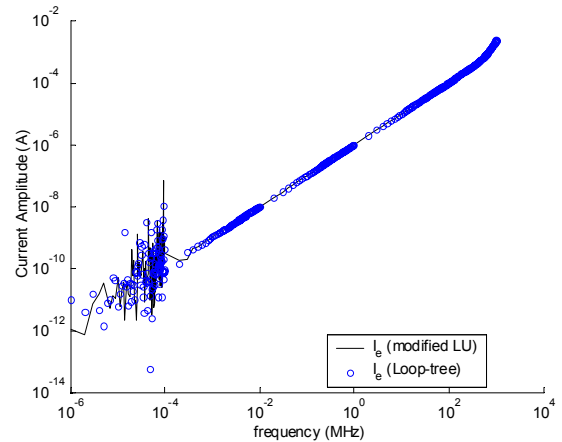


Figure 8. Modified LU and loop-tree results.

Figure 9 shows a simple circuit board configuration. Two traces of the same shape are centered over a 100-mm x 8-mm plate. The traces have the same length as the plate. They have a width of 1 mm and are placed 2 mm apart and 2 mm above the plate. One trace has a 1-volt source on one end and is terminated with a 50-ohm resistor. The other trace has 50-ohm resistors on both ends. Both the traces and the plate have zero thickness and are modeled as PEC surfaces. In order to observe conductive crosstalk at very low frequencies, a lumped resistance is located across the middle of the plate. The model employs 374 triangles and a total of 440 edges.

The current on the load resistor of the source trace, modeled using the RWG basis function method and the modified LU recombination method, is shown in Figure 10. Figure 11 shows the calculated current through the far-end resistor of the victim trace. In both cases, the standard RWG method exhibits significant errors below a few MHz, while the modified LU recombination method is accurate down to 1 Hz.

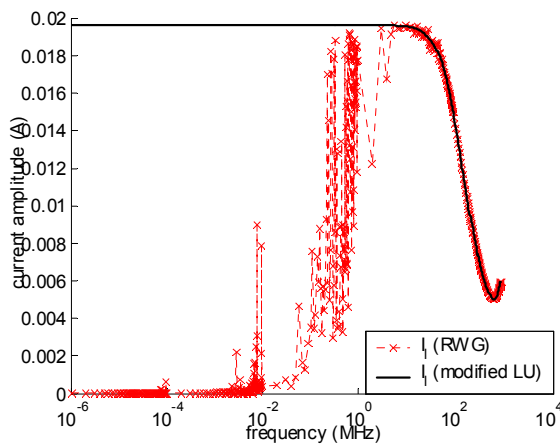


Figure 10. The current on the far end of the source trace.

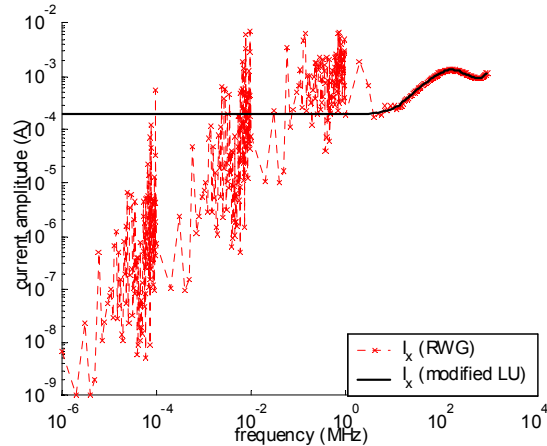


Figure 11. The coupled current on the far end of the victim trace.

V. CONCLUSION

In this paper, a new method to remove the low frequency instability inherent in the boundary element method using RWG basis functions is presented. This method uses LU decomposition of the impedance matrix to find the dependent components in the integration of the scalar potential. It then recovers the correct relationship between the dependent components, by modifying the L and U matrices.

This method accomplishes the same goal as using loop-tree basis functions. However the new method extracts all the necessary information from the MoM matrix itself without requiring the user to define new basis functions. It enforces a zero scalar potential over closed loops and preserves the information from the vector potential that otherwise would be lost due to numerical error. Dipole and loop circuit examples demonstrate that this method is capable of working at frequencies as low as a few Hz.

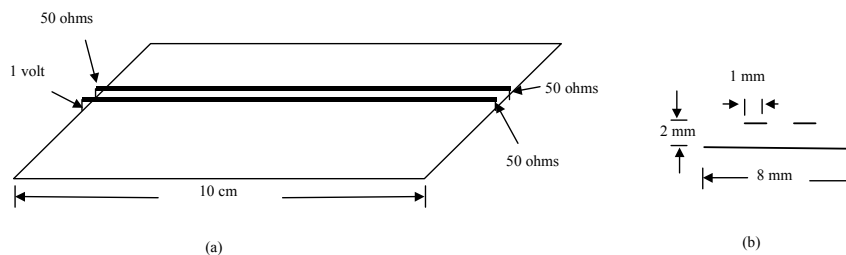
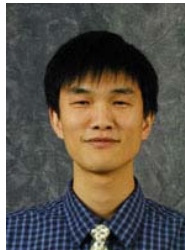


Figure 9. The crosstalk example. (a) geometry; (b) side view.

REFERENCES

- [1] S. M. Rao, D. R. Wilton, and A. W. Glisson, "Electromagnetic scattering by surfaces of arbitrary shape," *IEEE Trans. Antennas Propagat.*, vol. AP-30, no. 3, pp. 409-418, May 1982.
- [2] M. Burton, S. Kashyap, "A study of a recent moment-method algorithm that is accurate to very low frequencies," *Appl. Computational Electromagn. Soc. J.*, vol. 10, no. 3, pp. 58-68, Nov. 1995.
- [3] W. Wu, A. W. Glisson, and D. Kajfez, "A study of two numerical solution procedures for the electric field integral equation at low frequency," *Appl. Comp. Electromagn. Soc. J.*, vol. 10, no. 3, pp. 69-80, Nov. 1995.
- [4] J. R. Mautz and R. F. Harrington, "An E-field solution for a conducting surface small or comparable to the wavelength," *IEEE Trans. Antennas Propagat.*, vol. AP-32, no. 4, pp. 330-339, Apr. 1984.
- [5] S. Y. Chen, W. C. Chew, J. M. Song, and J. S. Zhao, "Analysis of low frequency scattering from penetrable scatterers," *IEEE Trans. Geoscience and Remote sensing*, vol. 39, no. 4, pp. 726-735, Apr. 2001.
- [6] J. S. Zhao, W. C. Chew, "Integral equation solution of Maxwell's equations from zero frequency to microwave frequencies," *IEEE Trans. Antennas Propagat.*, vol. 48, no. 10, pp. 1635-1645, Oct. 2000.
- [7] Y. H. Zhang, T. J. Cui, W. C. Chew, and J. S. Zhao, "Magnetic field integral equation at very low frequencies," *IEEE Trans. Antennas Propagat.*, vol. 51, no. 8, pp. 1864-1871, Aug. 2003.
- [8] H. Ke and T. Hubing, "Using an LU Recombination Method to Improve the Performance of the Boundary Element Method at Very Low Frequencies," *Proc. of the 2005 IEEE Internat. Symp. on Electromagnetic Compatibility*, Chicago, USA, pp. 442-445, Aug. 2005.
- [9] A. Peterson, S. L. Ray, and R. Mittra, *Computational Methods for Electromagnetics*, Section 10.6, pp. 433-434, New York: IEEE Press, 1997.
- [10] Y. Ji, "Development and applications of a hybrid finite-element-method/method-of-moments (FEM/MOM) tool to model electromagnetic compatibility and signal integrity problems in printed circuit boards," Ph.D. dissertation, University of Missouri-Rolla, 2000.



Haixin Ke received his BSEE and MSEE degrees from Tsinghua University in 1998 and 2001, respectively. He is currently a Ph.D. student in Electrical Engineering at the University of Missouri-Rolla. His research interests include numerical modeling techniques for analyzing signal integrity and electromagnetic compatibility problems.



Todd Hubing received his BSEE degree from MIT in 1980, his MSEE degree from Purdue University in 1982, and his Ph.D. in Electrical Engineering from North Carolina State University in 1988.

From 1982 to 1989, he was an electromagnetic compatibility engineer for IBM in Research Triangle Park, NC. He is currently a Professor of Electrical and Computer Engineering at the University of Missouri-Rolla. He serves on the Board of Directors and is a Past President of the IEEE EMC Society.

FVTD Characterization of Substrate Effects for Archimedean Spiral Antennas in Planar and Conformal Configurations

Christophe Fumeaux, Dirk Baumann, Rüdiger Vahldieck
 Swiss Federal Institute of Technology, ETHZ, IFH, 8092 Zürich, Switzerland
 E-mail: fumeaux/dbaumann/vahldieck@ifh.ee.ethz.ch

Abstract — This paper describes the application of the Finite-Volume Time-Domain (FVTD) method to characterize the influence of the substrate on Archimedean spiral antennas. The unstructured mesh of the FVTD method permits to model precisely the fine spiral structure and the thin underlying substrate. Time-domain numerical results permit to demonstrate how the substrate affects the distribution of currents propagating on the metallic spiral arms. The substrate influence in the active region of the spiral is described through an effective permittivity which can be related to the transverse mode distribution on the arm of the spiral. Application of the FVTD method to conformal spiral geometries is also suggested in three examples.

Index Terms—FVTD, spiral antennas, conformal antennas

I. INTRODUCTION

Archimedean spiral antennas are characterized by their compactness and stable radiation performances over a large bandwidth. They have been therefore widely applied as circular-polarized broadband radiators. The Archimedean spiral is identified through its constant line width and fixed distance between successive spiral windings. Because of these fixed dimensions, it is not a truly frequency-independent radiator. However, circular polarization and remarkably stable radiation patterns are achievable over a bandwidth of more than one decade. The operational frequency limits of the spiral are determined by two radii that delimits the spiral extent: The lowest operational frequency of the spiral is determined by its outer radius which defines the overall dimensions of the device, and the upper frequency limit is set by the inner spiral radius, required to accommodate the physical extent of the feed in the spiral center. A typical Archimedean spiral antenna exhibits narrow arms and a large number of windings, making it a challenging problem for any computational method. Several authors have analyzed Archimedean spiral antenna problems using different numerical methods. The approaches include e.g., the method of moments (MoM) [1],[2], the finite-difference time-domain method (FDTD) [3]-[5] and the finite-element method boundary integral method [4],[6]. Depending on the method used, approximations are made such as a thin-wire formulation for the MoM or

the limitation to square spiral or spiral in free-space in FDTD.

In the present paper, a numerical analysis of Archimedean spiral antennas on a thin-substrate is performed using the Finite-Volume Time-Domain (FVTD) method. The main advantage of the FVTD technique is its geometrical flexibility which arises from its application in an unstructured mesh. For the presented analysis, the curved spiral geometry is approximated accurately using an inhomogeneous tetrahedral mesh. This permits to resolve the fine features of the overall structure, such as the spiral arms and the thin substrate, through adaptation of the cell size to the local geometrical requirements.

The numerical analysis presented in this paper is addressing two aspects of the modeling of spiral antennas. First, the influence of the thin substrate supporting the metallic spiral arms (Section III). Particularly the effect of varying the permittivity and thickness of the dielectric material is characterized through a detailed simulation of the current distribution on the spiral arms, the field distribution transverse to the arms and the polarization bandwidth. Second, the paper explores conformal geometries of spiral antennas on conical, spherical, and cylindrical surfaces comparing the radiation characteristics to those of the corresponding planar geometry (Section IV).

II. FVTD ANALYSIS OF THE SPIRAL ANTENNA

This section reviews the main steps that lead to the FVTD simulation of the Archimedean spiral. Details of the geometry of the spiral structure are given as well as on the discretization of the models and on the computational aspects.

A. The FVTD Method

The FVTD method has been introduced at the end of the 80's [7],[8] as a numerical technique to solve Maxwell's equation in an unstructured mesh. It is inspired from finite-volume techniques that solve conservation equations in computational fluid dynamics. In electromagnetic applications, the method uses a

conservative form of Maxwell's curl equations integrated over finite volumes V_i

$$\begin{aligned} -\frac{\partial}{\partial t} \iiint_{V_i} \vec{B} dv &= \iint_{\partial V_i} \vec{n} \times \vec{E} da \\ \frac{\partial}{\partial t} \iiint_{V_i} \vec{D} dv &= \iint_{\partial V_i} \vec{n} \times \vec{H} da . \end{aligned} \quad (1)$$

For discrete solutions of these coupled differential equations, the finite volumes V_i are defined as the elementary cells of a partition of the computational volume. The boundary of the volume V_i is the surface ∂V_i with outward-pointing normal vector \vec{n} . Among the several FVTD algorithm variations, the formulation applied in this investigation is characterized by a collocation of all field components (electric and magnetic) in space and time. Specifically, all field components are located in the barycenter of the tetrahedral cells and are updated simultaneously during the march-in-time iteration. The explicit update equations are obtained using a flux-splitting method [9] and second-order in time is obtained using a predictor-corrector scheme.

B. The Archimedean Spiral Antenna

An Archimedean spiral is defined in polar coordinates (ρ, ϕ) as

$$\rho = a_0(\phi + \phi_0) \quad (2)$$

where a_0 defines the winding tightness and ϕ_0 is the starting angle that determines the inner radius of the spiral. To define the metallization of the two arms of the spiral antenna, four such curves rotated in increment of 90 degree are needed. The 90 degree rotation angle results in a self-complementary spiral where the arm width d_s is equal to the inter-arm spacing.

The spiral modeled in this investigation is composed of 11 turns. It has an arm width $d_s = 0.25$ mm, an outer radius $R = 11.25$ mm, and an inner radius $r = 0.25$ mm. The metallic spiral is supported by a substrate with a thickness of $h = 0.254$ mm (Fig. 1). All these dimensions make the device a challenging problem for time-domain simulations because of the discrepancy between the different scales involved: The full length along each spiral arm is around $L_s = 400$ mm, which represents ~ 1600 times the arm width d_s .

C. Discretized Spiral Model

To create the discretized FVTD spiral model, the boundary surfaces are first triangulated, and a tetrahedral volume mesh is constructed on the basis of this surface mesh (Fig. 2). This unstructured mesh is advantageous for two main reasons. First, the triangular discretization ensures an accurate approximation of the spiral. Second,

an inhomogeneous tetrahedral mesh permits to adapt locally the cell size to the dimensions of the fine structures

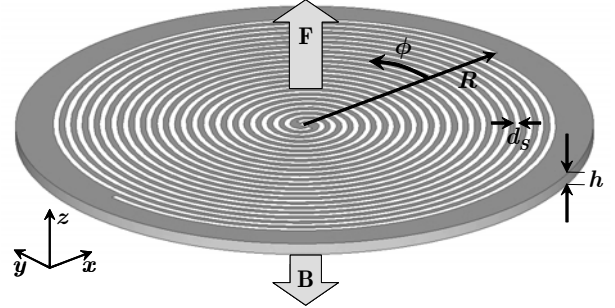


Fig. 1. Geometry of the analyzed Archimedean spiral. The two-arm spiral consists of 11 turns and has a fixed arm width d_s of 0.25 mm. The thin substrate under the substrate is also represented. It breaks plane symmetry of the device and is used to define directions for front (F) and back (B) radiation.

that need to be resolved (here both, the fine spiral arms and the thin substrate). As illustrated in Fig. 2 for the discretized model, the linear size of the tetrahedrons grows quickly from $\sim \lambda_{\min}/100$ in the close proximity of the spiral to $\sim \lambda_{\min}/10$ in free-space, where λ_{\min} is the smallest wavelength of interest. This inhomogeneity of the mesh keeps the total number of cells in the model at a reasonable level.

The transition from small cells to large cell can occur over a relatively short distance in a tetrahedral mesh. Nevertheless, a certain spatial range is required for the intermediate zone since a rapid transition decreases the mesh quality. The quality of a tetrahedron can be judged (among other criteria) by considering the ratio of its volume V_i to the sum of the area of its 4 faces S_k ($k = 1, 2, 3, 4$). Tetrahedrons with elongated or flat shapes (i.e. that have a small volume/surface ratio) should be avoided as much as possible for best results. In addition, this ratio is used to determine the time step necessary for stable FVTD computation, according to [9]

$$\Delta t \leq \frac{1}{c} \min_i \left(\frac{V_i}{\sum_{k=1}^4 S_k} \right). \quad (3)$$

Therefore, the “worst” or the smallest tetrahedron in the whole mesh determines the fundamental time step for stability. This requirement can be relaxed by combining the spatial inhomogeneity of the mesh to an inhomogeneous temporal discretization, implemented in the form of local time steps introduced in [10]. This scheme automatically separates the computational domain in sub-domains where time steps corresponding to power of two multiples $2^{\ell-1} \Delta t$ ($\ell = 1, 2, 3, \dots$) of the fundamental time step Δt are applied. Typically, for the

type of inhomogeneity necessary to mesh the spiral, 5 levels of time steps are used, corresponding to local time steps between Δt and $16\Delta t$.

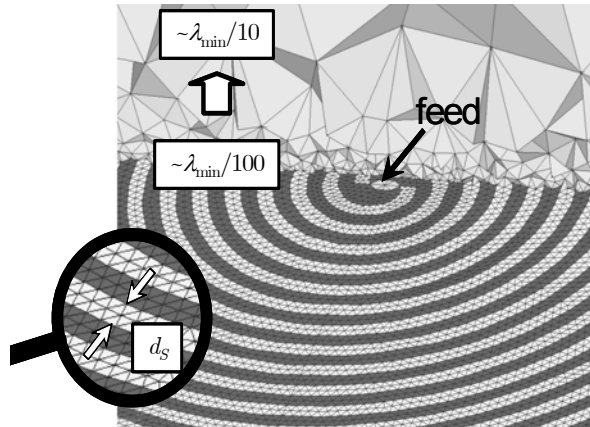


Fig. 2. Cut through the tetrahedral mesh of the spiral antenna. The lower part of the image shows the triangulation of the spiral plane, with a magnified view illustrating the resolution of the spiral arms.

D. Feed Model

In practical spiral antenna designs, a broadband balun is used for a balanced feeding of the radiating spiral. Simulations of such a practical balun has been demonstrated in [11] and compared to experimental data. The balun needs to be designed to provide nearly constant input impedance for the device over the operational frequency band. It is the component mainly responsible for the return loss of a practical spiral antenna.

The analysis of the balun can be in principle performed separately, and therefore, in the present simulation, a simple port is used to provide excitation of the spiral. The modeled port consists of 8 triangles located at the apex of the spiral (Fig. 2) where the excitation is provided through impressed electric fields between the starting points of the spiral arms. Both harmonic and broadband (1-20 GHz Gaussian pulse) excitations have been applied in this study.

E. Convergence and Computational Load

The side length of the triangles on the spiral plane corresponds to half the line width d_s (magnified view in Fig. 2). This fine discretization is necessary for the simulation to converge. It should be noted, that the strong inhomogeneity of the tetrahedral mesh permits to save computer memory. Despite a large number of triangles ($>10k$ triangles per arm) on the spiral surface, a spiral model requires less than 250 MB computer memory ($\sim 400k$ tetrahedrons). Large simulation times however are necessary to allow the low-frequency components of the wave to propagate along the full length of the spiral arms, and to be reflected.

F. Validation

For validation of the analysis method, the FVTD simulation results of a practical cavity-backed spiral antenna have been compared to measurements. The device has been modeled including the 26 turns two-arm spiral, the thin-substrate, the absorber-loaded cavity, the balun and the fine feed (Fig. 3). Far-field data measured in an anechoic chamber showed an excellent agreement with simulation and provided validation of the numerical analysis. A full analysis will be published elsewhere.

III. RESULTS – SUBSTRATE EFFECTS

In this section, the effects of the substrate under the Archimedean spiral on the radiation properties are characterized through numerical analysis. The variation of substrate characteristics, such as permittivity and thickness, are related to changes in the simulated current distributions. A characterization of the observed effects is obtained by defining an effective permittivity in the active region of the spiral antenna.

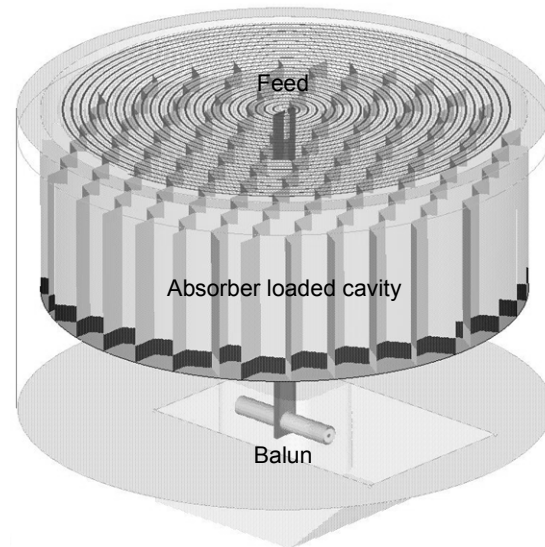


Fig. 3. Model of the cavity-backed Archimedean spiral analyzed for validation of the method. The substrate and the metallic housing of the device are shown transparent.

A. Substrate Permittivity Dependence

The current density on the metallic arms of the spiral is retrieved from the FVTD simulations. Instantaneous pictures of the current density at 8 GHz are shown in Fig. 4 for six different values of substrate permittivity. In these representations, the sign of the current density is defined considering the vectorial component of the current tangential to the spiral curve: A current propagating towards the outer end of the spiral is by convention positive, whereas a current directed toward the spiral feed is defined as negative.

The increase of the substrate permittivity ϵ_r is clearly apparent through the shrinking of the central area of the spiral where the current density distribution is visible. This shrinking is caused by the shortening of the effective wavelength λ_{eff} of the wave propagating along the spiral arms, which is defined introducing an effective permittivity ϵ_{eff} so that

$$\lambda_{eff} = \frac{\lambda_0}{\sqrt{\epsilon_{eff}}} . \quad (4)$$

Classically, the active radiating region of the spiral is defined as annular band around a radius r_a where one full turn of the spiral corresponds to one effective wavelength, i.e.

$$\lambda_{eff} = 2\pi r_a . \quad (5)$$

Past the active region, the current density becomes insignificant, and the contribution to radiation irrelevant. The dashed circles in the six images of Fig. 4 indicate the circles with approximate radius of r_a . A more precise characterization is obtained by considering the current distribution along the arms, as demonstrated in the next paragraph.

B. Effective Permittivity

To estimate the effective permittivity in the active region, the current density is plotted as a function of the length of the path along the spiral arms, starting from the feed. Fig. 5 shows an example of this 1D representation of the instantaneous current distribution at 8 GHz. The active region corresponds to the location on the spiral where the effective wavelength λ_{eff} is equal to a turn length ΔL of the spiral (as highlighted in the figure at around 5-6 turns). There, the currents on adjacent arms of the spiral are nearly in phase. On the inner windings of the spiral, before the active region, the current distribution takes the form of a damped sinusoid. Past the active region, on the outer turns of the spiral, the current distribution exhibits a non-sinusoidal standing-wave characteristic shaped by reflections at the end of the arms and by crosstalk between the windings.

The effective permittivity ϵ_{eff} in the active region of the spiral is retrieved by measuring the effective wavelength λ_{eff} from graphs similar as the one represented in Fig. 5. The region taken into account for the estimation of ϵ_{eff} encompasses one turn of the spiral where $\lambda_{eff} \approx \Delta L$. The results of the analysis are represented in Fig. 6 for substrate permittivities ϵ_r ranging from 1.0 (free-space) to 12.0. The uncertainty grows with increasing ϵ_r , since the measured quantity λ_{eff} has a nonlinear dependence (4) on ϵ_{eff} .

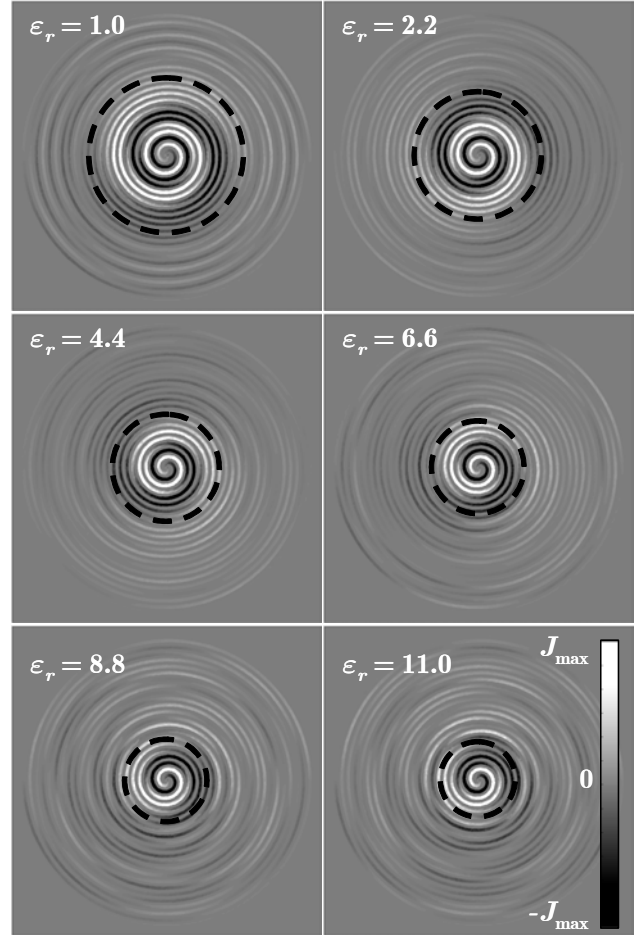


Fig. 4. Instantaneous current distribution on the spiral arms at 8 GHz for the six different permittivities ϵ_r indicated. The thickness of the substrate is equal to $h = 0.254$ mm. The dashed circles indicate the estimated location of the active region.

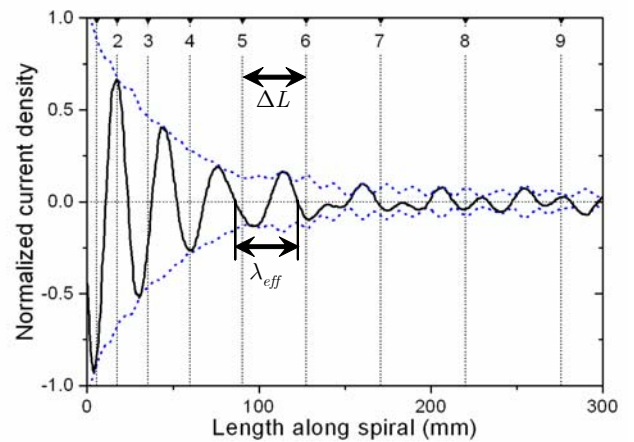


Fig. 5. Current distribution along the length of one spiral arm at 8 GHz. The permittivity of the substrate is $\epsilon = 2.2$ and its thickness $h = 0.254$ mm. The instantaneous current distribution is shown as solid line and the envelope as dotted lines. The upper scale indicates the turns on the spiral.

For comparison, the effective permittivities of two different coplanar strip (CPS) line geometries (shown in Fig. 7) are also represented in Fig. 6 as a function of the substrate permittivity. The first of these geometries (CPS 1) corresponds to the transverse dimensions of two adjacent spiral arms, i.e. with both the gap width G and the strips widths W_1 equal to d_S . It is observed that the effective permittivity of the CPS computed from closed-form expressions [12] is higher than the ϵ_{eff} in the active region of the spiral. To obtain a good match between a CPS geometry and the spiral, wider strips are necessary. In the coplanar geometry CPS 2, the strips widths are doubled to get a resulting ϵ_{eff} dependence that matches that of the spiral.

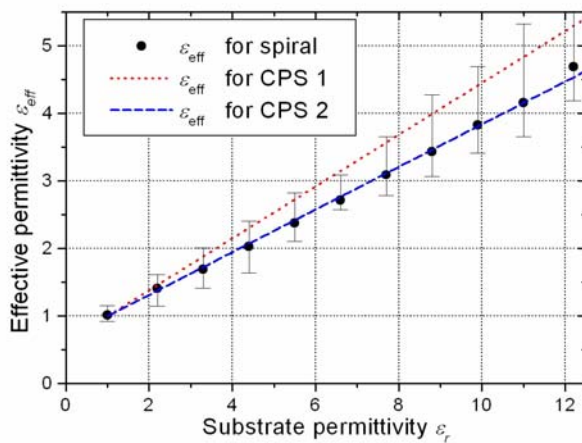


Fig. 6. Estimated effective permittivity for the propagation of the waves in the active region of the spiral antenna as a function of the substrate permittivity. The error bars indicates uncertainty, which is mainly arising from the influence of the reflected waves. Also shown for comparison are the ϵ_{eff} of the coplanar strip (CPS) lines depicted in Fig. 7.

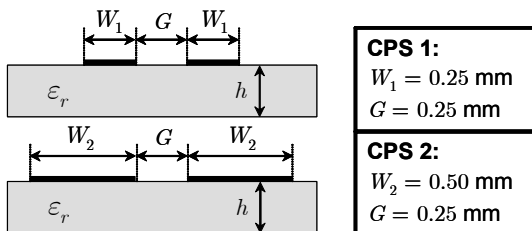


Fig. 7. Transverse dimensions of the coplanar strips used for comparison of the effective permittivity with that in the active region of the spiral. The dimensions of CPS 1 correspond to the transverse dimensions of two adjacent spiral windings. CPS 2 considers an increased width of the conducting strips.

C. Substrate Thickness Dependence

In a second numerical experiment, the permittivity $\epsilon_r = 4.4$ of the substrate is kept fixed, and the thickness h is varied. Fig. 8 shows the current distribution on the spiral for four different substrate thicknesses, from $h = 0$ (spiral in free-space) to $h \rightarrow \infty$ (semi-infinite substrate

in the lower half-space) for $\epsilon_r = 4.4$. The variation clearly affects the effective permittivity that describes the propagation of the currents on the spiral arms: As the substrate thickness grows, the active area shrinks towards the center of the spiral. However, by comparing the two bottom images of Fig. 8, it can be observed that increasing the substrate thickness past 1 mm does not change significantly the current distribution on the spiral arms.

The effective permittivity is then estimated on the basis of the simulations with the technique described in the previous paragraph (Sect. III B). The results for two substrate permittivities are shown in Fig. 9. In both plots, as the thickness of the substrate is increased, the effective permittivity rapidly increases from the value for a spiral in free-space ($\epsilon_{eff} = 1$ for $h = 0$) to the asymptotic value

$$\epsilon_{eff}(h \rightarrow \infty) = \frac{\epsilon_r + 1}{2}. \quad (6)$$

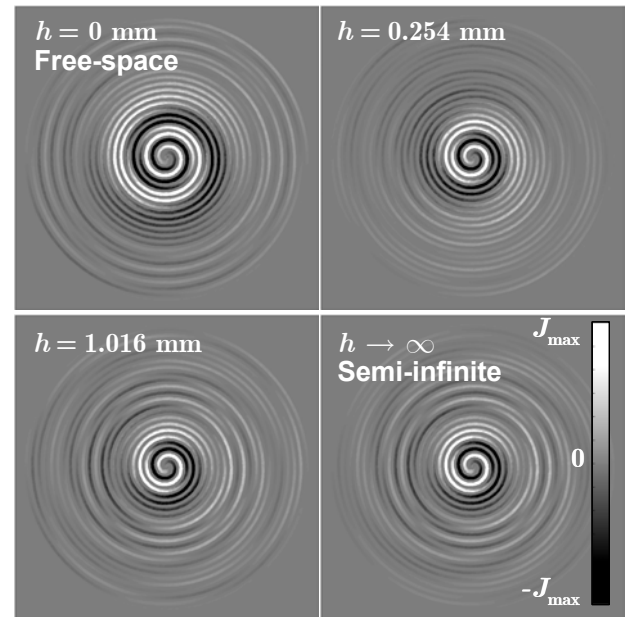


Fig. 8. Instantaneous current distribution at 8 GHz for the spiral on a substrate with permittivity $\epsilon_r = 4.4$ for four different substrate thicknesses h .

This asymptotic value is already nearly achieved, as anticipated from Fig. 8, for a substrate thickness of $h = 1$ mm. It should be mentioned that a nearly perfect match with the analytical value (6) is found for the ϵ_{eff} - values retrieved from the FDTD simulations. The same can be said about the value found for a spiral in free space. The consistency of these extremes provides an additional verification of the validity of the method used to estimate ϵ_{eff} from the results of the numerical analysis.

Also represented in the plots of Fig. 9 are the corresponding $\epsilon_{eff}(h)$ curves for the two CPS lines of Fig. 7. As in Fig. 6, the best match to the numerical

analysis is not obtained from the CPS 1, which has strip widths corresponding to the arm width d_s of the spiral ($W_1 = d_s$), but from the CPS 2, with has broader strips ($W_2 = 2d_s$). An explanation for this phenomenon is given in the following paragraph.

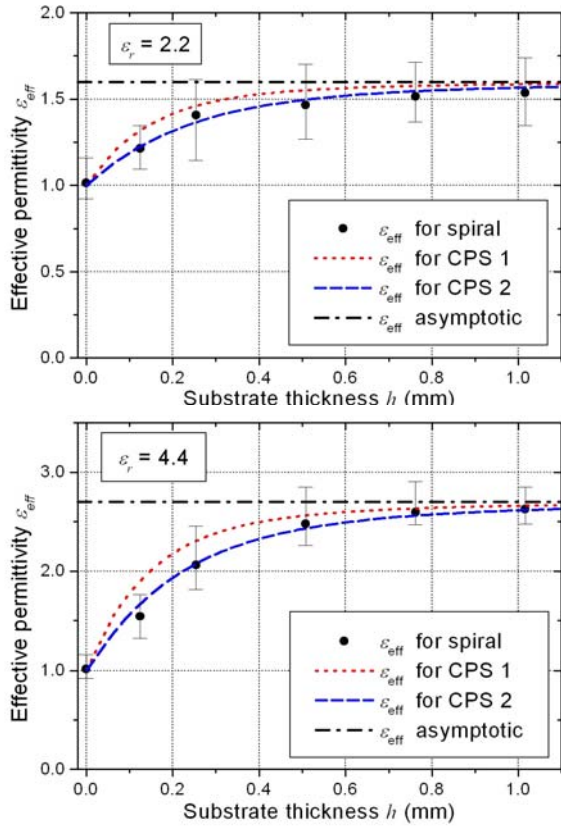


Fig. 9. Estimated effective permittivity of the propagation of the waves in the active region of the spiral antenna as a function of the substrate permittivity. Also shown for comparison are the ϵ_{eff} of the two coplanar strip lines depicted in Fig. 7 and the asymptotic value for semi-infinite substrate.

D. Transverse Field Distribution

The propagation properties of a wave on a transmission line are determined by the properties of the modes involved. For a CPS line, the fundamental mode is well-known: It is a quasi-TEM balanced mode, with the electric field in a transverse cross-section going from one strip to the other. Its propagation is best described through an effective permittivity ϵ_{eff} . Dependences of ϵ_{eff} on ϵ_r and h have been shown for two geometries with different strip widths (CPS 1 and CPS 2) in Fig. 7 and Fig. 9.

Despite a certain similarity between the transverse geometry of two adjacent spiral arms and that of a CPS, the propagation of currents along the spiral arms is different for the following reasons

- The spiral represents a system with a large number of adjacent coplanar strips.

- Although the feeding of the spiral is balanced, two adjacent arms of the spiral do not constitute a balanced system: the relative phase between adjacent arms depends on their location on the spiral.

Therefore, the transverse field distribution is expected to change significantly along the spiral arms, according to the phase difference between successive turns. To better visualize the sign (as defined in Sect. III A) of the instantaneous currents, the contrast of the grayscale current distribution representation in the spiral plane has been exaggerated in Fig. 10. Positive current density distribution is then represented as white and negative as black. The transverse field distributions are then considered in a plane perpendicular to the spiral plane, along a radial line, in the two ranges {1} and {2} indicated in Fig. 10.

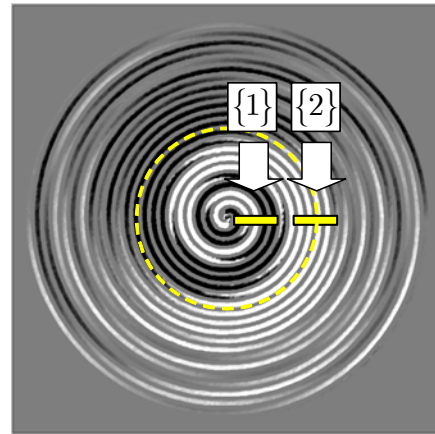


Fig. 10. Instantaneous current distribution on the spiral antenna at 8 GHz ($\epsilon_r = 2.2$, $h = 0.254$ mm). The contrast is increased, so that the alternating black and white color basically indicates regions of opposite current directions on the spiral arms. The region {1} and {2} indicate the locations of the transversal cuts represented in Fig. 11, and Fig. 12, respectively. The dashed circle indicates the location of the active radius.

{1} The transverse field distribution in the inner turns of the spiral at a particular time is shown in Fig. 11. From this image, it is apparent that because the adjacent arms are at different potentials, the field lines are primarily confined in the direct vicinity of the strips. Starting from the left of the image, the E and H field distributions on the three first strips in Fig. 11 ($r = 0.5 - 1.75$ mm) resemble the field distribution of the dominant coplanar waveguide (CPW) mode. Continuing along the radial direction ($r = 2.0 - 2.75$ mm), the field lines between the last two represented strips resemble those of a CPS. Other instantaneous representations might show different patterns, but all share the characteristics that the fields are closely confined near the strips and that interaction is basically limited between adjacent arms.

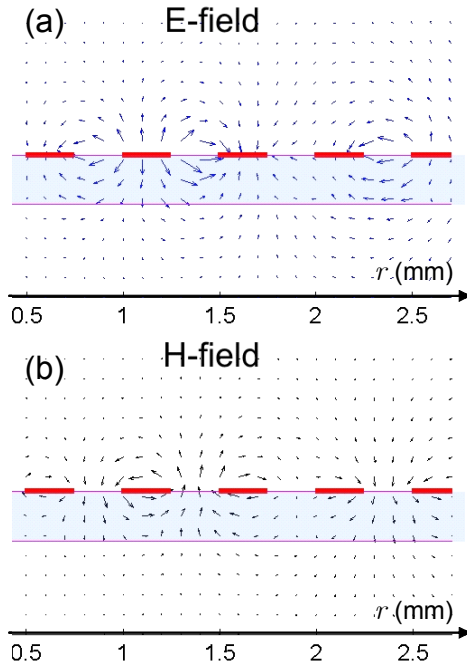


Fig. 11. Vectorial representation of the transverse field distribution at 8 GHz in the center region {1} of the spiral antenna (r is the radius from the center of the spiral). The substrate is indicated by the shaded region and the spiral arms by line segments that represent cross-sections of the metallic strips. The arrows are normalized for good representation.

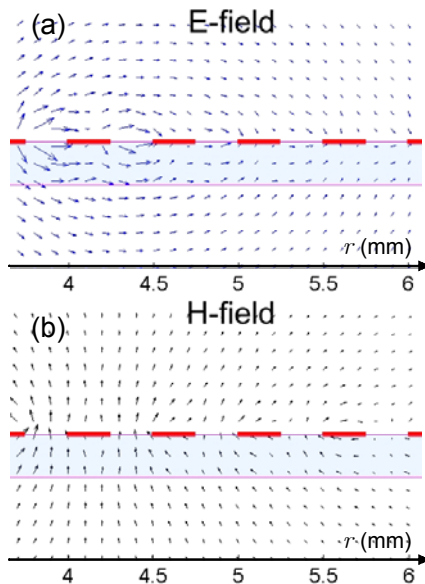


Fig. 12. Vectorial representation of the transverse field distribution at 8 GHz in the active region {2} of the spiral antenna. The substrate is indicated by the shaded region and the spiral arms by line segments that represent cross-sections of the metallic strips. The arrows are normalized for good representation.

{2} Considering the transverse field distribution in the active region (Fig. 12), one observes a behavior different than in the inner turns. In the spiral active radiating region, adjacent arms are in phase, and therefore at nearly the same potential for all times. Therefore, the field lines show that interaction between strips extends farther than just to the

adjacent arm, and the fields are much less closely confined than in the inner turns. This explains why the effective permittivity ϵ_{eff} in the active region of the spiral is lower than that of the CPS 1 that has corresponding transverse dimensions. Instead, ϵ_{eff} shows the same dependence as CPS 2, which has less confined fields because of its larger strips. The non-confined field distribution in the vicinity of the spiral arms in the active region is the cause for increased “radiation loss” of the considered coplanar structure.

The comparison of Fig. 11 and Fig. 12 illustrates why the propagation velocity on the spiral arms is not constant. In the more confined transverse field distribution of the inner turns, the effective permittivity is larger than in the outer turns, since most of the field lines under the spiral are located in the substrate. This effect is of course dependent on the frequency and this dispersive effect contributes to the chirp observed in broadband pulse excitation.

E. Effect on the Radiation Characteristics

The analysis presented in this section is concerned with the near-field of the spiral antenna. However, the substrate configuration correspondingly influences the radiation characteristics. This paragraph shows how the lower frequency limit of the circular polarization bandwidth varies with the substrate permittivity of the spiral.

The low-frequency transition from linear polarization to circular polarization happens on a spiral antenna when the active radius approaches the outer radius of the spiral. Currents reflected at the outer end of the spiral are degrading the circular polarization purity. The low-frequency transition from linear to circular polarization is apparent through the following far-field characteristics (for increasing frequency):

- The axial ratio of the polarization ellipse decreases from a large value (indicating nearly linear polarization) and becomes smaller than the specified value for circular polarization (typically 3 dB).
- The phase between the orthogonal E -field components has a transition from 0 degree to 90 degree.

Fig. 13 and Fig. 14 show distinctly this low-frequency transition in axial ratio and phase, with a clear dependence on substrate permittivity. In Fig. 13 the approximated frequency of the 3 dB transition is displaced from higher than 5 GHz for the free-space spiral to about 2.6 GHz for $\epsilon_r = 11.0$. This reduction factor of nearly 2 corresponds to $\sqrt{\epsilon_{eff}}$, which confirms the data of Fig. 6.

Furthermore, the following general remarks can be made based on the numerical analysis of the spiral:

- For both the axial ratio and the phase, oscillations are observed in the transition region. These oscillations are caused by currents reflected from the spiral outer end. As the frequency increases, the reflected currents are reduced since the active region shrinks towards the spiral center.
- The polarization purity in the band of operation is slightly degraded by the presence of the denser substrate.

- The presence of the substrate causes an asymmetry that introduces a slightly higher radiation towards the back-side (substrate side). This effect becomes slightly more pronounced as the permittivity of the substrate increases resulting in a front-to-back asymmetry smaller than 0.5 dB.
- The input resistance in the operation range of the spiral is lower for substrates with higher permittivity ϵ_r . The results of the simulation give a value of $\sim 120 \Omega$ for the spiral in free-space. The value for $\epsilon_r = 11.0$ is decreased to $\sim 60 \Omega$. These values are obtained with a simple feed in the center of the spiral. A wideband balun is necessary in practice to provide balanced excitation over the operational bandwidth of the spiral and for matching purpose.
- The high-frequency limit of the spiral operation band is determined by the physical extension of the feed in the center of the spiral. The transition to linear polarization for broadside direction is -in this case- not the limiting factor and is therefore not apparent in Fig. 13 and Fig. 14. The higher operation frequency limit is determined by the degradation of the radial symmetry of the main beam.

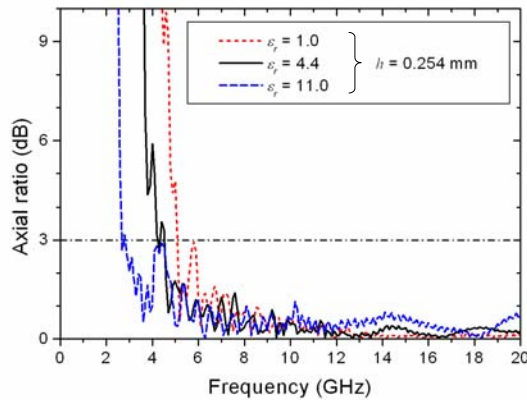


Fig. 13. Axial ratio of the polarization ellipse in broadside direction as a function of the frequency for three different substrate permittivities.

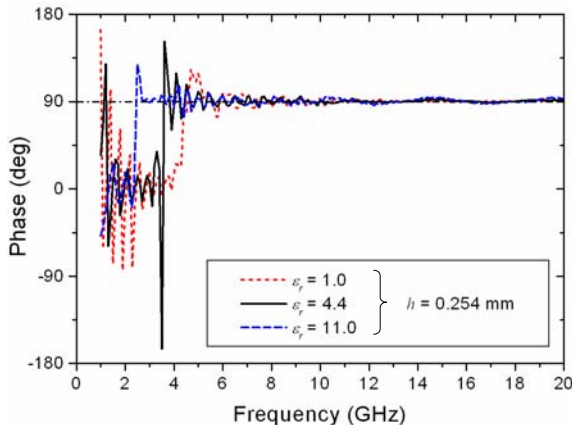


Fig. 14. Phase between the two orthogonal E -field components in broadside direction (far-field) as a function of the frequency for three different substrate permittivities.

IV. CONFORMAL SPIRAL ANTENNAS

In this section the radiation characteristics of spirals mounted conformally on non-planar substrates are investigated. Several examples are tested numerically: Spirals in (a) conical, (b) spherical and (c) cylindrical shape. The advantage of using the tetrahedral mesh is particularly evident in this case, since the FVTD simulation of such conformal structures imposes no additional computational cost over that of the corresponding planar geometry. In all conformal configurations presented below, the spirals have the same characteristic dimensions as in the planar configuration shown above, i.e. 11 spiral turns, arm width $d_s = 0.25$ mm, outer radius $R = 11.25$ mm, and inner radius $r = 0.25$ mm. All substrates have the standard thickness of $h = 0.254$ mm. The next section presents all studied configurations followed by a discussion of their radiation characteristics.

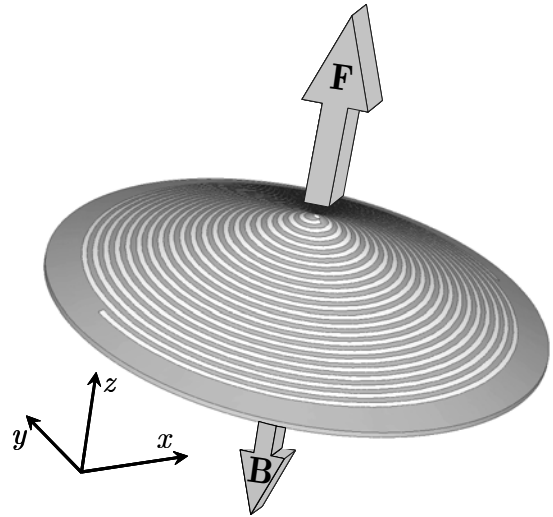


Fig. 15. Spiral antenna mounted on a conical substrate. The supporting cone has a height of 5 mm and a thickness of 0.254 mm. The spiral has the same geometry as the planar configuration (outer radius $R = 11.25$ mm). The front side of the antenna is defined in the direction showing towards the tip of the cone.

A. Conical Configuration

A conical arrangement (Fig. 15) with a base radius of 12.5 mm and a height of 5 mm is considered first. This conformal configuration is a well-known variation of spiral antenna design, the conical spiral antenna, characterized by an increased gain towards the front side. However in the present design, a very flat cone is considered, mainly with the aim of providing comparison with the spherical and cylindrical configurations.

B. Spherical Configuration

In the second conformal configuration, the spiral is mounted on a spherical surface. The curvature radius of the surface is 18 mm. This results in a total height (extent in z -direction) close to 5 mm for the configuration shown in Fig. 16.

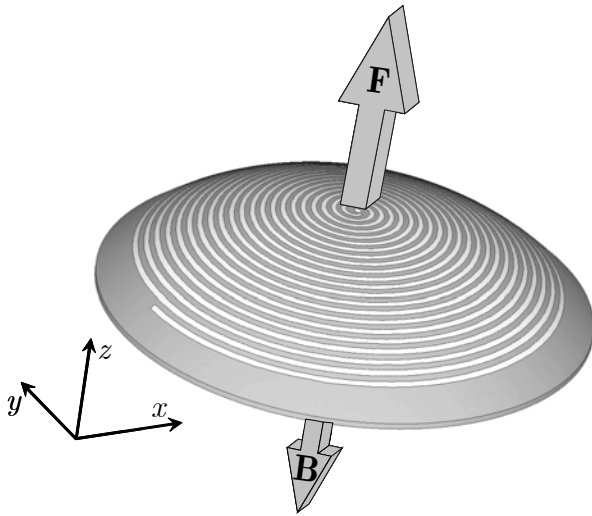


Fig. 16. Spiral antenna mounted on a spherical substrate. The substrate has a curvature radius of 18 mm and a thickness of 0.254 mm. The spiral has the same geometry as the planar configuration (outer radius $R = 11.25$ mm).

C. Cylindrical Configurations

Two different variations of the spiral mounted on a section of a cylinder have been analyzed. The two arrangements are distinguished by their different axis orientations with respect to the feed, as shown in Fig. 17. The curvature of the cylinder section exhibits the same radius as in the spherical case, i.e. 18 mm, and therefore has the same 5 mm total height for both cylindrical configurations.

D. Radiation Properties of the Conformal Geometries

The radiation performance of all three configurations is investigated in terms of:

- (i) Circular polarization purity (for broadside direction)
- (ii) Front-to-back ratio (F/B).

Both these characteristics are considered as a function of frequency.

(i) Circular Polarization

The circular polarization of the spiral is best described by the axial ratio of the polarization ellipse. Additional information is provided by the phase between the two orthogonal E-field components. For both the conical and the spherical configuration, the phase and the axial ratio are plotted in Fig. 18. From a comparison with the curves for the planar configuration (which is also shown in the figure), it can be concluded that for both cases, the integration on a non-planar substrate has no noticeable adverse effect on the polarization quality or on the low-frequency limit of the operational range. The reason for this result is the symmetry of the substrate geometries with respect to the spiral axis.

Axial symmetry is not present in both cylindrical geometries of Fig. 17 and thus an increased axial ratio (~ 1 dB) can be observed, indicating a degradation of the circular polarization purity (Fig. 19). In both orientations of the cylinder substrate, a spiral turn exhibits a saddle shape which affects the phase between the orthogonal field components in

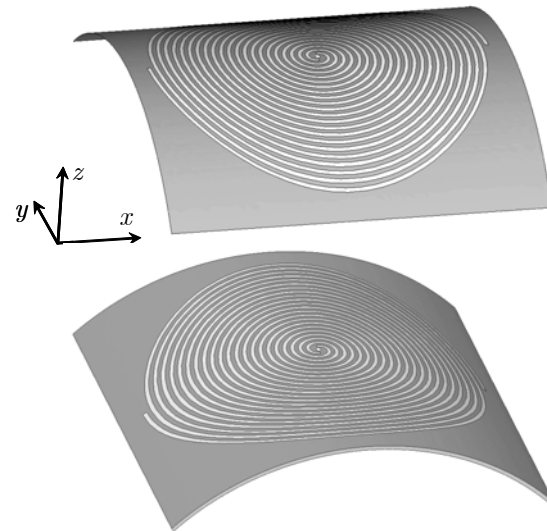


Fig. 17. Spiral antennas mounted on cylindrical substrates. The substrates have a curvature radius of 18 mm and a thickness of 0.254 mm. Top: Cylinder with axis in x -direction; bottom: Cylinder with axis in y -direction. The feed for both cases is oriented in y -direction. The spirals have the same geometry as the planar configuration (outer radius $R = 11.25$ mm).

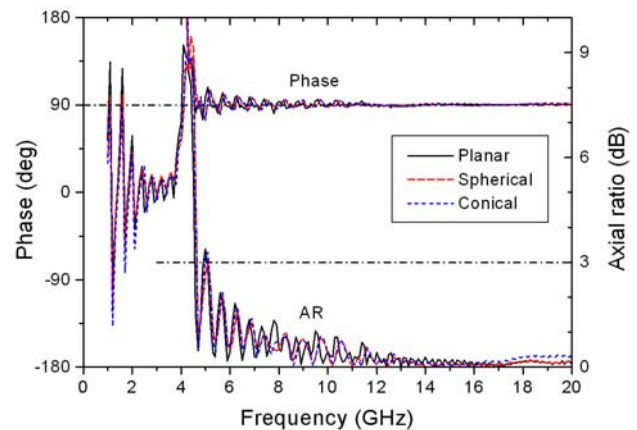


Fig. 18. Phase and axial ratio of the polarization ellipse in broadside direction (far-field on front side) as a function of the frequency for conical, spherical and planar configurations.

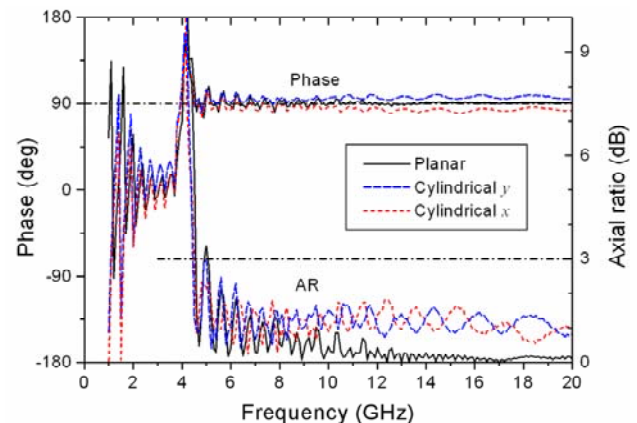


Fig. 19. Phase and axial ratio of the polarization ellipse in broadside direction (far-field on front side) for the two cylindrical configurations (Fig.17) as a function of the frequency, compared to the planar case.

the far-zone, altering the circular polarization. The deviation of the phase from the required 90 degree between the two orthogonal components is also visible in Fig. 19. The oscillations observed in the axial ratio are due to the frequency-dependent angular location of the active radiating region on the saddle shaped turns of the spiral. This is confirmed by the fact that the oscillatory behaviors of the axial ratios for the two orientations of the cylinder are 180 degree offset. Also, a variation of the effective permittivity (not shown here) affects the shape of the oscillations consistently, i.e. a smaller ϵ_r stretches the oscillations since the effective wavelength is larger.

(ii) Front-to-Back Ratio

The second radiation characteristic altered by the shape of the substrate is the F/B ratio (measured as ratio of radiated fields in $+z$ vs. $-z$ direction). The frequency dependence of this quantity is shown in Fig. 20 for the different geometrical configurations investigated. Depending on the shape of the substrate, different observations can be made:

- For the planar spiral, the presence of a substrate breaks the symmetry. For a thin substrate, this leads to a slight increase of the radiation towards the substrate side (F/B $\simeq -0.12$ dB at 20 GHz).
- In the conical configuration, as expected, the pattern becomes more directive towards the front side. Due to the small height of the supporting dielectric cone, the F/B only reaches a maximum of 2.7 dB at about 9 GHz. For higher frequencies, the F/B ratio decreases because of the effect of the conical substrate, which now acts as a “reflector” (or “lens”) towards the back side. This effect is demonstrated in Fig. 21 which shows the radiation patterns of the spiral at 9 GHz, i.e. near the frequency of maximum F/B ratio, and at 18 GHz, where the F/B ratio has decreased to 0.6 dB. The narrowing of the back lobe is clearly visible and becomes more pronounced as the frequency increases. Although the 3 dB beamwidth of the front lobe is in both cases close to 80°, the 3 dB beamwidth of the back lobe is reduced from 84° at 9 GHz down to 62° at 18 GHz.

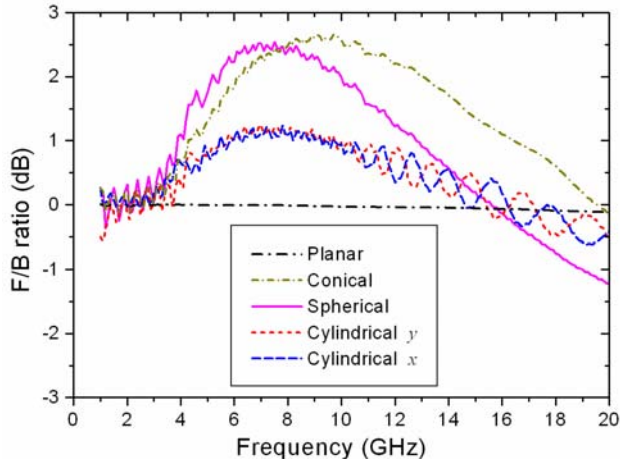


Fig. 20. Front-to-back ratio as a function of the frequency for the four conformal spiral configurations compared to the planar case.

- For the spherical arrangement, similar observations as in the conical case can be made, with an overall increase of directivity for front radiation. This is expected because of the similarity with the conical configuration: Adjacent turns in the active spiral region correspond roughly to a conical arrangement with an angle α set by the tangential line to the sphere. In the spherical case, this flare angle α varies with the frequency-dependent location of the active region. For a particular frequency (and the associated active radius r_{a0}), the tangential line on the sphere has an angle corresponding to the flare angle α_0 of the conical arrangement (Fig. 22). In the present arrangement, this happens for a frequency of 6 GHz. Below this frequency, the angle α is sharper than in the conical case, which explains the displacement of the maximum F/B toward lower frequencies (maximum F/B occurs around 7 GHz) compared to the conical configuration. Again, the F/B ratio is shaped by two competing mechanisms with opposing effects: The increased directivity towards the front due to the non-planar shape, and the narrowing of the back lobe caused by the substrate acting as a reflector. For the spherical case, a negative F/B ratio past 16 GHz can be observed.
- For the two cylindrical configurations, the increase of the front-side directivity because of the convex shape is less pronounced than in the spherical case. In addition, oscillations (with 180 degree offset between both orientations) are also visible at the higher frequencies because of the saddle shape of the spiral turns. In the cylindrical configuration, the substrate exhibits only one radius of curvature in a particular direction and therefore, both effects observed (increase of front-side radiation and narrowing of the beam towards the back) are restricted to one angular dimension.

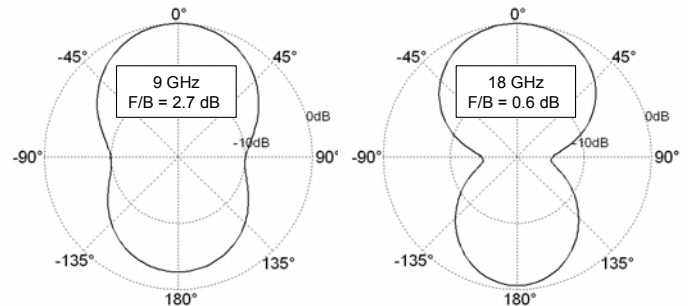


Fig. 21. Radiation pattern of the conical spiral in the xz plane for two frequencies. Left-hand side: 9 GHz; Right-hand side: 18 GHz.

Considering that for most applications, the back side radiation is suppressed through a cavity, the design of a spiral can take advantage of a conformal design, even with the limited extent of the height (as opposed to classical conical spirals that have a sharp flare angle). However, for shapes that do not have an axial symmetry with respect to the center of the spiral, e.g. for surfaces with varying radii of curvatures in different directions, a degradation of the circular polarization can be expected.

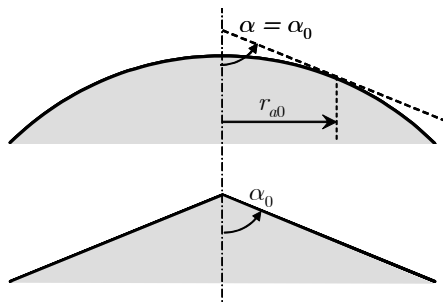


Fig. 22. Side views of the spherical and conical substrates. The flare angle α of the cone is defined in the bottom drawing. The tangential line to the sphere that forms the same angle α with the axis of the spiral occurs for an active radius r_a and is shown in the top drawing.

V. CONCLUSION

The FVTD method has been utilized for the simulation of various Archimedean spiral antennas with different substrate configurations. Although the presented radiating structures are challenging for most computational methods, the analysis with the FVTD method has been straightforward and did not impose any problems. The FVTD's unstructured mesh provides the geometrical flexibility to resolve the fine spiral structure on a thin substrate.

The FVTD method has also been used to investigate substrate effects on the radiation characteristics of an Archimedean spiral. Several variations in the substrate properties (permittivity, thickness) and shape (planar vs. non planar) have been studied. Conclusions have been drawn based on the simulated effective permittivity relevant for currents propagating along the spiral arms and considering the spiral active radiating region, i.e. where one spiral turn corresponds to one effective wavelength.

The effects caused by variations of the substrate permittivity and thickness of the planar configurations have been compared to CPS lines with comparable cross-sections (same gap width as inter-arm distance on the spiral). The comparison of the transverse field distribution on the spiral and on the CPS permits to understand the difference found in the effective permittivity for both geometries. Considering a CPS with broader conducting strips (i.e. same gap, but twice the strip width) gives a good approximation of the ϵ_{eff} on the spiral.

Three configurations of spirals on non-planar substrates with common geometrical shapes have been investigated. The effects on the antenna polarization and F/B ratio have demonstrated that the performance of non-planar configurations provide no substantial degradation of the radiation characteristics. In some configurations radiation characteristics are even improved.

As for the FVTD method it should be emphasized that the simulation of conformal structures represents the same

computational load as that of a corresponding planar geometry. Simulations of configurations with multiple radii of curvatures in different directions require no algorithm modifications and are solely reduced to the problem of mesh generation.

ACKNOWLEDGMENT

This work was supported by Armasuisse, Science and Technology, Bern, Switzerland.

REFERENCES

- [1] J.J. van Tonder, J.H. Cloete, "A study of an Archimedes spiral antenna", *IEEE Antennas and Propagat. Society Int. Symp. Dig.*, AP-S vol. 2, pp. 1302 – 1305, June 1994.
- [2] H. Nakano, K. Nogami, S. Arai, H. Mimaki, J. Yamauchi, "A spiral antenna backed by a conducting plane reflector", *IEEE Trans. Antennas Propagat.*, vol. AP-34, pp. 1417-1423, June 1986.
- [3] M.N. Afsar, Y. Wang, R. Cheung, "Analysis and measurement of a broadband spiral antenna", *IEEE Antennas Propagat. Mag.*, vol. 46, pp. 59-64, Feb. 2004.
- [4] C.W. Penney, R.J. Luebbers, "Input impedance, radiation pattern, and radar cross section of spiral antennas using FDTD", *IEEE Trans. Antennas Propagat.*, vol. AP-42, pp. 1328 -1332, Sept. 1994.
- [5] H. Nakano, M. Ikeda, K. Hitosugi, J. Yamauchi, "A spiral antenna sandwiched by dielectric layers", *IEEE Trans. Antennas Propagat.*, vol. AP-34, pp. 791-796, June 2004.
- [6] D.S. Filipović, J.L. Volakis, "Novel slot spiral antenna designs for dual-band/multiband operation", *IEEE Trans. Antennas Propagat.*, vol. AP-51, pp. 430-440, March 2003.
- [7] N.K. Madsen, R.W. Ziolkowski, "A three-dimensional modified finite volume technique for Maxwell's equations", *Electromagnetics*, vol. 10, pp. 147-161, 1990.
- [8] V. Shankar, A.H. Mohammadian, W.F. Hall, "A time-domain, finite-volume treatment for the Maxwell equations", *Electromagnetics*, vol. 10, pp. 127-145, 1990.
- [9] P. Bonnet, X. Ferrieres, B.L. Michielsen, P. Klotz, J.L. Roumiguieres, "Finite-Volume Time Domain Method", Chapter 9 in *Time domain electromagnetics*, edited by S.M. Rao, Academic Press, San Diego, 1999.
- [10] C. Fumeaux, D. Baumann, P. Leuchtman, R. Vahldieck, "A generalized local time-step scheme for efficient FVTD simulations in strongly inhomogeneous meshes", *IEEE Trans. Microwave Theory Tech.* MTT-52(3), pp. 1067-1076, 2004.
- [11] D. Baumann, C. Fumeaux, P. Leuchtman, R. Vahldieck, "Generalized-scattering-matrix extraction using the finite-volume time-domain (FVTD) method", *IEEE MTT-S Int. Microwave Symp. Dig.*, pp. 1701-1704, June 2004.
- [12] B.C. Wadell, "Transmission Line Design Handbook", Artech House, Boston (1991).



Christophe Fumeaux received the diploma and Ph.D. degrees in physics from the Swiss Federal Institute of Technology (ETH) Zurich, Switzerland, in 1992 and 1997, respectively. His Ph.D. thesis on antenna-coupled infrared detectors was awarded the ETH Silver Medal of Excellence. From 1998 to 2000 he was post-doctoral researcher in infrared technology at the School of Optics (CREOL) of the University of Central Florida (UCF), Orlando. In 2000 he joined the Swiss Federal Office of Metrology in Bern, Switzerland, as a scientific staff member. Since 2001, he is a research associate at the Laboratory for Electromagnetic Fields and Microwave Electronics (IFH) at ETH Zurich. His current main research interest concerns computational electromagnetics in the time domain for numerical analysis of microwave circuits and antennas.

now the Editor-in-Chief effective Jan. 2004. Since 1992 he serves on the Technical Program Committee of the IEEE International Microwave Symposium, the MTT-S Technical Committee on Microwave Field Theory, and in 1999 on the TPC of the European Microwave Conference. From 1998 until 2003 Professor Vahldieck was the chapter chairman of the IEEE Swiss Joint Chapter on MTT, AP and EMC.



Dirk Baumann received the Dipl. Ing. degree in electrical engineering from the University of Karlsruhe, Germany, in 2001. Between Spring and Fall 2000 he did an internship at the Alaska SAR Facility (ASF) in Fairbanks, AK, working on the calibration of ASF's SAR processor. Currently he is working toward the Ph.D. degree in electrical engineering at the Laboratory for Electromagnetic Fields and Microwave Electronics (IFH), ETH Zurich, Switzerland. His research interests include numerical methods with emphasis on time domain techniques and their application to general electromagnetic problems.



Rüdiger Vahldieck received the Dipl. Ing. and the Dr. Ing. degrees in electrical engineering from the University of Bremen, Germany, in 1980 and 1983, respectively.

From 1984 to 1986 he was a Postdoctoral Fellow at the University of Ottawa, Canada. In 1986 he joined the Department of Electrical and Computer Engineering at the University of Victoria, British Columbia, Canada, where he

became a Full Professor in 1991. During Fall and Spring of 1992-'93 he was a visiting scientist at the "Ferdinand-Braun-Institut für Höchstfrequenztechnik" in Berlin, Germany. In 1997 he accepted an appointment as Professor for electromagnetic field theory at the Swiss Federal Institute of Technology, Zurich, Switzerland, and became head of the Laboratory for Electromagnetic Fields and Microwave Electronics (IFH) in 2003. His research interests include computational electromagnetics in the general area of EMC and in particular for computer-aided design of microwave, millimeter wave and opto-electronic integrated circuits.

Professor Vahldieck is a Fellow of the IEEE. He received the J.K. Mitra Award of the IETE (in 1996) for the best research paper in 1995, and was co-recipient of the outstanding publication award of the Institution of Electronic and Radio Engineers in 1983. Since 1981 he has published more than 230 technical papers in books, journals and conferences, mainly in the field of microwave CAD. He is the Past-President of the IEEE 2000 International Zurich Seminar on Broadband Communications (IZS'2000) and since 2003 President and General Chairman of the international Zurich Symposium on Electromagnetic Compatibility. He is a member of the editorial board of the IEEE Transaction on Microwave Theory and Techniques. From 2000 until 2003 he served as an Associate Editor for the IEEE Microwave and Wireless Components Letters and is

High Accuracy Evaluation of the EFIE Matrix Entries on a Planar Patch

Malcolm M. Bibby* and Andrew F. Peterson**

*Gullwings, 47 Whitney Tavern Rd., Weston, MA 02493

e-mail: mbibby@gullwings.com

**Georgia Institute of Technology, Atlanta, GA

e-mail: peterson@ee.gatech.edu

Abstract - A method for the evaluation of the integral of the free-space Green's function on a planar patch, that is exact to machine precision, is developed. The results are used to evaluate two other, commonly used, methods - singularity extraction and singularity cancellation. It was found that these two methods produced unacceptable results. It is shown what steps need to be taken to improve the performance of these methods for patches with varying aspect ratios.

I. INTRODUCTION

The matrix entries arising within numerical solutions of the electric field integral equation, EFIE, for a wide range of applications involve an evaluation of integrals of the form

$$I(x,y) = \iint f(x',y') \frac{e^{-jkR}}{R} dx'dy' \quad (1)$$

where f is usually a bounded, well-behaved function $k = 2\pi/\lambda$ and R is given by

$$R = \sqrt{(x-x')^2 + (y-y')^2}. \quad (2)$$

These calculations are most difficult when the test point (x,y) is within or near the source cell over which the integral is performed, due to the $O(1/R)$ behavior of the Green's function, e^{-jkR}/R .

One widely-used method of evaluating (1) is the singularity extraction (SE) procedure, often implemented as

$$I(x,y) = \iint \left\{ f(x',y') \frac{e^{-jkR}}{R} - f(x,y) \frac{1}{R} \right\} dx'dy' \quad (3)$$

$$+ f(x,y) \iint \frac{1}{R} dx'dy'.$$

The first integral in (3) is to be evaluated by quadrature, while the second yields an analytical result for triangular or rectangular domains [1]. The first integrand in (3), although bounded, is still not analytic in the vicinity of $R=0$. Therefore, the accuracy of the result obtained with standard quadrature rules for that integral may be limited.

A second approach for evaluating (1) is the singularity cancellation (SC) method, often known as the Duffy transformation [2]. Suppose that the domain of integration is the rectangle $0 < x' < a$, $0 < y' < b$, and the test point (singularity) is $x = y = 0$. The SC method requires that the domain be divided into two triangles, each of which is transformed into a rectangular domain according to (4),

$$I(x,y) = \int_{x'=0}^a \int_{y'=0}^{Kx'} f(x',y') \frac{e^{-jkR}}{R} dx'dy' \quad (4)$$

$$+ \int_{y'=0}^b \int_{x'=0}^{y'/K} f(x',y') \frac{e^{-jkR}}{R} dx'dy'$$

$$= \int_{x'=0}^a \int_{u=0}^1 f(x',y') Kx' \frac{e^{-jkR}}{R} dx'du$$

$$+ \int_{y'=0}^b \int_{v=0}^1 f(x',y') y' \frac{e^{-jkR}}{KR} dvdy'.$$

K is the cell aspect ratio

$$K = \frac{b}{a}. \quad (5)$$

The change of variable

$$y' = Kx' u, \quad dy' = Kx' du \quad (6)$$

is used in the first integral and the substitution

$$x' = \frac{1}{K} y' v, \quad dx' = \frac{1}{K} y' dv \quad (7)$$

is used in the second. In the new first integral, at the test point, the integrand is now given by

$$\begin{aligned} f(x', y') Kx' \frac{e^{-jkR}}{R} \Big|_{x' \rightarrow 0} &\cong \frac{f(x', y') Kx'}{\sqrt{(x')^2 + (Kx')^2 u^2}} \\ &= \frac{f(x', y')}{\sqrt{(1/K)^2 + u^2}}. \end{aligned} \quad (8)$$

In the second, the integrand is

$$\begin{aligned} f(x', y') \frac{1}{K} y' \frac{e^{-jkR}}{R} \Big|_{y' \rightarrow 0} &\cong \frac{f(x', y') y' / K}{\sqrt{(y' / K)^2 v^2 + (y')^2}} \\ &= \frac{f(x', y')}{\sqrt{v^2 + K^2}}. \end{aligned} \quad (9)$$

These results are both nonsingular at the original test point, permitting the two integrals in (4) to be evaluated using standard numerical quadrature routines. As shown below, the cancellation of the singularity depends on the cell aspect ratio, K , and the SC approach can yield poor overall accuracy when K is very small or very large.

A third approach is an extension of the SE method described above, obtained by extracting a second term from the integrand [3]. The extended singularity extraction (ESE) approach may be implemented as

$$\begin{aligned} I(x, y) = &\iint \left\{ \begin{aligned} &f(x', y') \frac{e^{-jkR}}{R} \\ &-f(x, y) \frac{(1 - k^2 R^2 / 2)}{R} \end{aligned} \right\} dx' dy' \\ &+ f(x, y) \iint \frac{1}{R} dx' dy' - \frac{f(x, y) k^2}{2} \iint R dx' dy'. \end{aligned} \quad (10)$$

A closed-form expression for the final integral in (10) is described in the following section. The first integral, as in the SE method, is to be evaluated by quadrature.

In order to evaluate the effectiveness of the above approaches a method capable of providing high accuracy is needed. One such approach is based on a MacClurin series expansion of the Green's function [4], followed by the closed-form evaluation of the integrals of each term in the series. This series closed-form (SCF) approach is described in the following section.

II. FORMULATION OF THE SCF METHOD

For illustration, consider the evaluation of (1) for a rectangular cell $0 < x' < a$, $0 < y' < b$, $f(x', y') = 1$, and the test point (singularity) at $x = y = 0$. The Green's function may be expanded as

$$\frac{e^{-jkR}}{R} = S_1 - jS_2 \quad (11)$$

where

$$S_1 = \frac{1}{R} - \frac{k^2}{2!} R + \frac{k^4}{4!} R^3 - \frac{k^6}{6!} R^5 + \dots, \quad (12)$$

$$S_2 = k - \frac{k^3}{3!} R^2 + \frac{k^5}{5!} R^4 - \frac{k^7}{7!} R^6 + \dots \quad (13)$$

Since the expansion in (13) is regular and causes no undue difficulty, we focus on (12) and the integral

$$I = \iint \left\{ \frac{1}{R} - \frac{k^2}{2!} R + \frac{k^4}{4!} R^3 - \frac{k^6}{6!} R^5 \dots \right\} dx' dy'. \quad (14)$$

The SC approach can be applied to (14) to yield

$$I = I_0 + I_1 + I_2 + \dots \quad (15)$$

where

$$\begin{aligned} I_0 &= \int_{x'=0}^a \int_{u=0}^1 \frac{Kx'}{\sqrt{(x')^2 + (Kx')^2 u^2}} dx' \\ &+ \int_{y'=0}^b \int_{v=0}^1 \frac{y'}{K\sqrt{(y'/K)^2 v^2 + (y')^2}} dv dy' \\ &= \int_{x'=0}^a \int_{u=0}^1 \frac{1}{\sqrt{(1/K)^2 + u^2}} dx' \\ &+ \int_{y'=0}^b \int_{v=0}^1 \frac{1}{\sqrt{v^2 + K^2}} dv dy', \end{aligned} \quad (16)$$

$$\begin{aligned} I_1 &= -\frac{k^2}{2!} \left[\int_{x'=0}^a \int_{u=0}^1 Kx' \sqrt{(x')^2 + (Kx')^2 u^2} dx' \right. \\ &\quad \left. + \int_{y'=0}^b \int_{v=0}^1 \frac{y'}{K} \sqrt{(y'/K)^2 v^2 + (y')^2} dv dy' \right] \\ &= -\frac{k^2}{2!} \left[\frac{K^2}{2} \int_{x'=0}^a \int_{u=0}^1 (x')^2 \sqrt{1/K^2 + u^2} dx' \right. \\ &\quad \left. + \frac{1}{K^2} \int_{y'=0}^b \int_{v=0}^1 (y')^2 \sqrt{v^2 + K^2} dv dy' \right], \end{aligned} \quad (17)$$

and the n -th term can be expressed as

$$\begin{aligned} I_n &= (-1)^n \frac{k^{2n}}{(2n)!} \\ &\times \left[\frac{K^{2n}}{2^n} \int_{x'=0}^a \int_{u=0}^1 (x')^{2n} \left[\sqrt{1/K^2 + u^2} \right]^{2n-1} dx' \right. \\ &\quad \left. + \frac{1}{K^{2n}} \int_{y'=0}^b \int_{v=0}^1 (y')^{2n} \left[\sqrt{v^2 + K^2} \right]^{2n-1} dv dy' \right]. \end{aligned} \quad (18)$$

The problem reduces to finding an analytical evaluation of

$$I = \int_0^1 \left(\sqrt{\delta^2 + z^2} \right)^{2n-1} dz. \quad (19)$$

With the aid of the transformation $z = \delta \tan u$, $dz = \delta \sec^2 u du$, $u_1 = \tan^{-1} \left| \frac{1}{\delta} \right|$, equation (19) can be written as

$$\begin{aligned} I &= \int_0^{u_1} \left(\sqrt{\delta^2 + \delta^2 \tan^2 u} \right)^{2n-1} \delta \sec^2 u du \\ &= \delta^{2n} \int_0^{u_1} \left(\sqrt{1 + \tan^2 u} \right)^{2n-1} \sec^2 u du \\ &= \delta^{2n} \int_0^{u_1} \frac{1}{\cos^{2n+1} u} du \\ &= \delta^{2n} \left\{ \frac{\sin z}{2n} \left[\sec^{2n} z + \sum_{k=1}^{n-1} \frac{(2n-1)(2n-3)\dots(2n-2k+1)}{2^k (n-1)(n-2)\dots(n-k)} \sec^{2n-2k} z \right] \right. \\ &\quad \left. + \frac{(2n-1)!!}{2^n n!} \ln \sqrt{\frac{1+\sin z}{1-\sin z}} \right\}. \end{aligned} \quad (20)$$

The identity used in the final statement of (20) is found in [5; 2.519.2 & 2.526.9]. In practice the number of terms required for the evaluation of (15) to full quad precision is approximately 15, although it was always evaluated to machine precision using as many terms as necessary, per (23).

The formulation can be expanded to include polynomials such as

$$f(x, y) = x^p y^q \quad (21)$$

or by any function that can be represented by combinations of such polynomials. The associated integrals have the form

$$\begin{aligned} I_n &= \int_0^a x^p dx \int_0^b y^q R^{2n-1} dy \\ &= \frac{a^{2n+p+q+1}}{2n+p+q+1} K^{2n+q} \int_0^1 u^q \left(\sqrt{\left[\frac{1}{K} \right]^2 + u^2} \right)^{2n-1} du \\ &\quad + \frac{b^{2n+p+q+1}}{2n+p+q+1} \frac{1}{K^{2n+p}} \int_0^1 v^p \left(\sqrt{v^2 + K^2} \right)^{2n-1} dv. \end{aligned} \quad (22)$$

Evaluation of these integrals proceeds in a manner similar to the earlier method.

III. METHODOLOGY

The present study investigates the numerical accuracy obtained from the preceding methods, and the relative computational efficiency (run times)

required for each method to produce a specified level of accuracy. The use of single, double, and quad precision for some or all of the calculations is considered. The objectives of the testing were:

- To examine the effect of machine precision on the accuracy of the SCF method.
- To investigate the accuracy of the SE and SC methods.

The location of the test point is rarely at the exact corner of a patch and so, in practice, the domain is divided into four rectangular sub-patches each with a corner at the test point. These sub-patches will frequently have aspect ratios significantly different from $K=1.0$. As the location of the test point may well be the result of using a quadrature rule, it is instructive to examine the location of test points required by various quadrature formulae. In particular, one is interested in the smallest dimension involved in an application. Examples are shown in Table I. The third rule, “Linlog+Sqrt singularity” possesses the capability to integrate a log singularity and a square root singularity at the same end point.

Table I. Locations of the first test point for various Gaussian quadrature rules, $0 \leq x \leq 1$

# of nodes in the quadrature rule	Type of quadrature rule		
	Gauss-Legendre	Linlog [6]	Linlog + Sqrt singularity [7]
16	5.30E-3	8.28E-5	4.99E-6
32	1.37E-3	5.69E-6	9.86E-8
48	6.14E-4	1.15E-6	9.35E-9
64	3.47E-4	3.73E-7	1.73E-9

From Table I, one can see that in some instances the location of the test point may result in rectangles with aspect ratios of $K \approx 10^{-9}$. Therefore the range over which tests were conducted was $1.0 \times 10^{-10} \leq K \leq 1.0$. Two tests were designed. In the first, the location of the test point is at the corner of a patch that has one side dimension of 0.1λ and the other a dimension of 10^{-n} , where $1 \leq n \leq 11$. The second test uses a constant patch size of $0.1\lambda \times 0.1\lambda$. The test point is located on the line stretching from the center of the patch, at

$(0.05, 0.05)$ to the corner of the patch, at $(0.0, 0.0)$, in steps of 10.0^{-n} where $0 \leq n \leq 10$. The integration over the patch is achieved by dividing it into four sub-patches each with a corner at the test point. The purpose of the second test is to evaluate the impact of the high aspect ratio sub-cell on the overall integral.

As a baseline for comparison, a reference result for the series (15) was evaluated in Multi-Precision, MP, arithmetic [8] using an epsilon value of 10.0^{-400} and reported out in quad (REAL*16) precision. Such precision may seem extreme. However, the comparative accuracy of the other results was based on these reference values.

The effect of machine precision was investigated not only for the present new formulation but also for the SE and SC methods. The integrals requiring the use of quadrature rules were evaluated with an adaptive Gauss-Kronrod-Patterson, GKP, procedure using tabulations derived in MP from an algorithm published by Patterson [9]. These integrals were evaluated so that:

$$\frac{|I_n - I_{n-1}|}{|I_n|} \leq 2\epsilon \tag{23}$$

where I_n is the value of the integral after the n^{th} evaluation. *Epsilon*, ϵ , is defined as the difference between 1.0 and the smallest number which is greater than 1.0, that can be represented by the compiler. Two other compiler parameters needed to be considered - *tiny* and *huge* - which are the smallest and largest positive numbers respectively that can be represented by the compiler. These are shown in Table II for single, double and quad precision, as well as for the level of precision used in the MP calculations performed in this study.

Relative error was used to evaluate the different schemes using:

$$Error = \log_{10} \left| \frac{I - I_{ref}}{I_{ref}} \right| \tag{24}$$

Table II. Compiler specific parameters for various levels of precision.

precision	ϵ	$\text{Log}_{10}(\epsilon)$	tiny	huge
single	1.19E-07	-6.92360	1.18E-38	3.40E+38
double	2.22E-16	-15.6536	2.22E-308	1.80E+308
quad	1.93E-34	-33.7154	3.36E-4932	1.19E+4932
MP	1.00E-400	-400.000	6.19E-14449439	6.19E+14449439

Here, I and I_{ref} are the values of the relevant integral, evaluated in the stated machine precision, and the reference value respectively.

IV. NUMERICAL RESULTS

The results for the SE method, the SC method and the SCF method when evaluated in quad precision are shown in Figure 1.

The susceptibility of the SC method to aspect ratio has already been mentioned in the literature, [4, 10], and investigating this phenomenon was an early motivation for this study. Such suspicions appear to be confirmed as that approach essentially fails for $K < 10^{-4}$. The criticism of the SE method is that although the obvious singularity has been removed, the first integral in the right-hand side of (3) is still not “smooth” in a mathematical sense due to the derivatives of the integral being unbounded at one of the integration limits. Nevertheless, the results over the test range are accurate to better than double precision. The results for the SCF method show that, even in quad precision, there is degradation for the more extreme aspect ratios.

When the same study was carried out in single precision, none of the methods provided acceptable results. It is doubtful that one would encounter such extreme aspect ratios as $K = 1.0 \times 10^{-10}$ when using single precision. Nevertheless the underlying causes for these failures were examined as an aspect ratio of $K = 1.0 \times 10^{-6}$ could arise in single precision work.

Two factors were determined to play a role in the failures – the value of ϵ and the values of tiny/huge in the Fortran compiler. Examination of the calculations in the SCF method of (20) indicated the need to carry numbers with a wide range of values – wider than is available with single precision. Routines were written that accepted single precision input and returned single precision

output, but within the routines the working precision was either double or quad precision. The results for the SCF method are reported in Table III.

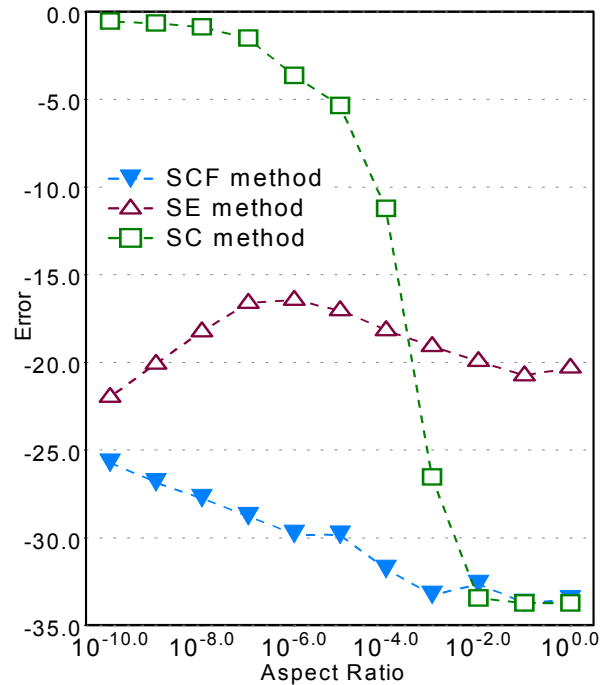


Fig. 1. Plots of results for the SCF, SE, and SC methods when using quad precision for all calculations.

In Table III, the first column reports the aspect ratio, AR, for the calculations. The column headed “single” reports the results of simply using single precision. The column headed “tiny” again uses single precision throughout but guards against $\cos^{2n}(z)$ being less than the tiny value in Table II. When this potential violation is detected, the routine exits with the last value calculated prior to the detection. The columns headed “double” and “quad” indicate use of the special routines mentioned earlier. Use of double precision prevented total failure of the SCF method. However, quad precision was needed to provide

Table III. Effect of machine precision on error (24) of the SCF solution. (d.b.z. is divide-by-zero fault)

AR	Mode			
	single	tiny	double	quad
1	-6.92369	-6.92369	-6.92369	-6.92369
0.1	-6.92369	-6.92369	-6.92369	-6.92369
1.00E-02	-5.97828	-5.97828	-6.92369	-6.92369
1.00E-03	-5.64612	-5.64612	-6.92369	-6.92369
1.00E-04	-5.05785	-5.05785	-6.92369	-6.92369
1.00E-05	d.b.z.	-4.06992	-6.92369	-6.92369
1.00E-06	d.b.z.	0.00E+00	-6.92369	-6.92369
1.00E-07	d.b.z.	0.00E+00	-6.92369	-6.92369
1.00E-08	d.b.z.	0.00E+00	-6.75083	-6.92369
1.00E-09	d.b.z.	0.00E+00	-6.00224	-6.92369
1.00E-10	d.b.z.	0.00E+00	-5.05588	-6.92369

success over the entire range. The reason that double precision does not provide success over the entire range has to do with the calculation of $R = \sqrt{c^2 + x^2}$. Precision is lost whenever the ratio of the two numbers, c^2 and x^2 , or its reciprocal, is less than the relevant value of ϵ . This can be seen quite clearly in the “double” results, where precision is lost when the aspect ratio exceeds 1.0E-07.

When the SE approach was examined with single precision it was found that the integration of the “non-singular” part was performing satisfactorily, but evaluation of the singular part was not good, as seen in the “single” column of Table IV. Once this was performed in double precision, the errors were at their lower limit until the aspect ratio reached a value of $K = 1.0 \times 10^{-9}$. To cover the entire range, it was necessary to use quad precision. This is an important finding, as the SCF method has not yet been developed for more general situations and hence one may still need to resort to SE and/or SC.

The problems in the SC method can be understood when one considers the effect of K on the evaluation of the inner integrals of (4). When K takes on an extreme value one of the inner integrals is essentially independent of the variable of integration whereas the other inner integral approaches $O(1/R)$. This latter effect makes the Gauss-Legendre integration perform very poorly.

Table IV. Effect of machine precision on error (24) of the SE solution.

AR	Single	Double	Quad
1	-6.92369	-6.92369	-6.92369
0.1	-6.41765	-6.92369	-6.92369
1.00E-02	-5.94832	-6.92369	-6.92369
1.00E-03	-5.07121	-6.92369	-6.92369
1.00E-04	-3.90065	-6.92369	-6.92369
1.00E-05	-2.42700	-6.92369	-6.92369
1.00E-06	2.73E-03	-6.92369	-6.92369
1.00E-07	2.37E-03	-6.92369	-6.92369
1.00E-08	2.10E-03	-6.92369	-6.92369
1.00E-09	1.89E-03	-6.92369	-6.92369
1.00E-10	1.71E-03	-6.10287	-6.92369

The solution is to use the SE method in conjunction with the SC method. That is, use (3) in each of the integrals of (4). The results are reported in Table V. Again the importance of evaluating the extracted component in double precision is to be noted. If the extracted component is only evaluated in single precision there is a degradation of the accuracy for intermediate values of the aspect ratio.

Similar findings were made when using double precision as the underlying machine precision. It was necessary to write routines that accepted double precision input and returned double precision output with the internal calculations performed in quad precision. The relevant results are shown in Tables VI. The heading “Double + quad ESE” in this table means that the main quadrature routines used double precision while the

evaluation of the extracted components was performed in quad precision. Note that it is necessary to extract two terms in the SE method that is use ESE, as is also the case in the SC method.

Table V. Effect of machine precision on error (24) of the SC solution.

AR	Single only	Single + single SE	Single + double SE
1	-6.92369	-6.92369	-6.92369
0.1	-6.92369	-6.92369	-6.92369
1.00E-02	-6.92369	-5.97828	-6.92369
1.00E-03	-6.92369	-5.55185	-6.92369
1.00E-04	-4.09225	-4.97039	-6.92369
1.00E-05	-2.08886	-3.98617	-6.92369
1.00E-06	-1.1023	-2.52202	-6.92369
1.00E-07	-0.70402	-1.96481	-6.92369
1.00E-08	-0.53765	-1.30139	-6.92369
1.00E-09	-0.43983	-1.34868	-6.92369
1.00E-10	-0.3739	-1.39132	-6.92369

are close to, if not identical, to the results for the SCF method.

So far, the reported results were concerned with accuracy. The timing results for quad precision are shown in Table VII. These show that the SCF method is clearly superior to the other two methods. It is important to note that all of the calculations are performed in the same precision. When one runs similar timing tests in double and single precision the SE method is superior. The reason for the shift is that the SCF method is still largely performed in quad precision, whereas the quadrature routines run mainly in double and single precision respectively.

In the second test series the test point was not located at a corner of the patch. Instead it was moved on a diagonal extending from the center to close to the corner. The patch was then subdivided into four sub-patches each with a corner at the test point. Two of the sub-patches are square and two have potentially extreme aspect ratios. The test was conducted for each of the three methods, incorporating the information learned in

Table VI. Error (24) for double precision on the three methods of integration.

AR	SCF		SE		SC	
	Double	Quad internal	Double	Double + quad ESE	Double	Double + quad ESE
1	-13.8785	-15.6536	-15.6536	-15.464	-15.6536	-15.6536
0.1	-13.2513	-15.6536	-15.6536	-15.6536	-15.6536	-15.6536
1.00E-02	-7.91709	-15.6536	-14.1219	-15.6536	-15.6536	-15.6536
1.00E-03	-5.77831	-15.6536	-13.5385	-15.6536	-15.6536	-15.6536
1.00E-04	-3.82704	-15.6536	-12.2983	-15.6536	-11.2123	-15.6536
1.00E-05	-3.91093	-15.6536	-11.7914	-15.6536	-5.33437	-15.6536
1.00E-06	-3.98120	-15.6536	-10.1758	-15.6536	-3.62397	-15.6536
1.00E-07	-4.04162	-15.6536	-9.18065	-15.6536	-1.50125	-15.6536
1.00E-08	-4.09416	-15.6536	-8.38368	-15.6536	-0.85638	-15.6536
1.00E-09	-4.13613	-15.6536	-8.43096	-15.6536	-0.64213	-15.6536
1.00E-10	-4.12927	-15.6536	-6.14382	-15.6536	-0.52264	-15.6536

Returning to the use of quad precision as the underlying, and only, precision level, the SE method is modified to incorporate the extraction of two terms. The SC method is modified to incorporate the incorporation of one term and then two terms. The results appear in Figure 2, which has the same scaling as Figure 1 – for direct comparison. It is clear that when two terms are extracted in both the SE and SC methods the results

the first test series. Thus it was unsurprising that the integrations all performed well. An exception occurred in the quad precision studies where it was found that, in the case of the SE method, better results were obtained when the integration area was divided into four subsections, each with a corner at the location of the (extracted) singularity – just as was necessarily done for the SCF and the SC methods. The two results for the SE method are

shown in Table VIII. In the cases of single precision and double precision, integration over the entire cell gave results at the limit of precision.

Table VII. Results for relative times for the three different methods when set up for greatest accuracy, using quad precision.

AR	SCF	SE	SC
1	4.59E-02	4.48	2.20
0.1	3.91E-02	2.31	4.15
1.00E-02	4.00E-02	1.46	6.18
1.00E-03	4.10E-02	1.12	6.18
1.00E-04	4.00E-02	1.12	6.15
1.00E-05	4.00E-02	0.86	6.01
1.00E-06	4.00E-02	0.69	6.12
1.00E-07	4.10E-02	0.73	6.13
1.00E-08	3.91E-02	0.17	2.64
1.00E-09	4.00E-02	0.15	2.14
1.00E-10	4.00E-02	0.16	2.76

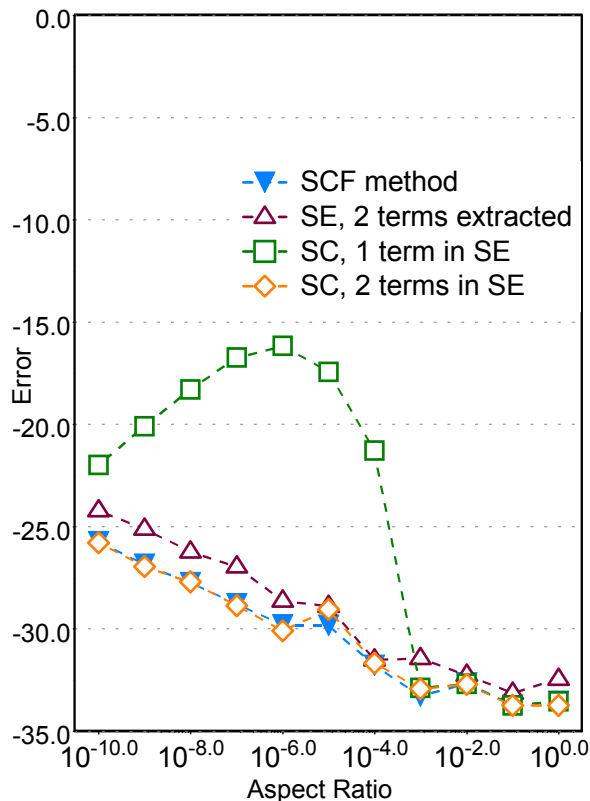


Fig. 2. Plots of results for the SCF, SE, and SC methods when using quad precision for all calculations and incorporating two term extraction.

Table VIII. Results for error (24) for the SE method, using quad precision.

AR	Entire cell	4 sub-cells
1	-16.7542	-33.5543
0.1	-18.3499	-32.6836
1.00E-02	-21.8931	-32.3831
1.00E-03	-23.9701	-32.3669
1.00E-04	-27.0118	-32.4292
1.00E-05	-30.7153	-32.4119
1.00E-06	-32.1547	-32.2953
1.00E-07	-32.4289	-32.4651
1.00E-08	-32.6807	-32.6807
1.00E-09	-32.3217	-32.3083
1.00E-10	-32.3644	-32.3797

V. CONCLUSIONS

The SCF method was developed as a fast, accurate method to evaluate the integral of the free-space Green's function. This method was also used to investigate the effect of machine precision on other approaches to this same evaluation. It was found that in order to span the range of aspect ratios investigated here:

- The SCF method needed to be evaluated in quad precision regardless of the default precision of the compiler.
- The analytical term(s) extracted in the SE method needed to be evaluated in a level of precision higher than the default precision.
- The SC method was successful only when singularity extraction was applied to the inner integrals, and only if those extracted terms were evaluated in a higher level of precision than the default level.
- When extracted terms were evaluated in quad precision it was also important to extract a second term and evaluate it in quad precision.

When dealing specifically with planar patches and polynomial basis functions, the SCF method is the fastest approach of the three considered when using quad precision. Otherwise, the SE approach is faster.

VI. REFERENCES

- [1] A. F. Peterson, S. L. Ray, R. Mittra, *Computational Methods for Electromagnetics*, IEEE Press, 1998.
- [2] M. G. Duffy, "Quadrature Over a Pyramid or Cube of Integrands with a Singularity at a Vertex", *SIAM J. Numer. Anal.*, vol. 19, no. 6, pp. 1260-1262, Dec. 1982.
- [3] S. Jarvenpaa, M. Taskinen and P. Yla-Oijala, "Singularity extraction technique for integral equation methods with higher order basis functions on plane triangles and tetrahedra", *Intl. Journal for Numerical Methods in Engineering*, vol. 58, pp. 1149-1165, 2003.
- [4] M. M. Bibby, A. F. Peterson, "High Accuracy Calculation of the Magnetic Vector Potential on Surfaces", *ACES Journal*, vol. 18, no. 1, pp. 12-22B, 2003.
- [5] L. S. Gradshteyn & I. M. Ryzhik, *Table of Integrals, Series, and Products*, Sixth Edition, Academic Press, 2000.
- [6] J. H. Ma, V. Rokhlin, S. Wandzura, "Generalized Gaussian Quadrature Rules for Systems of Arbitrary Functions", *SIAM J. Numer. Anal.*, vol. 33, pp. 971-996, June 1996.
- [7] H. Cheng, V. Rokhlin, N. Yarvin, "Nonlinear Optimization, Quadrature, and Interpolation", *SIAM J. Optim.*, vol. 9, no. 4, pp. 901-923, 1999.
- [8] D. H. Bailey, "A Fortran-90 Based Multi-precision System", *ACM Trans. on Mathematical Software*, vol. 20, no. 4, pp. 379-387, Dec 1995. See also RNR Technical Report RNR-90-022, 1993 and <http://crd.lbl.gov/~dhbailey/mpdist/>.
- [9] T. N. L. Patterson, "Generation of Interpolatory Quadrature Rules of the Highest Degree of Precision with Preassigned Nodes for General Weight Functions", *A.C.M. Trans. On Math Software*, vol. 15, no. 2, pp. 137-143, June, 1989.
- [10] M. A. Khayat & D. R. Wilton, "Numerical Evaluation of Singular and Near-Singular Potential Integrals", *IEEE Trans. Antennas Prop.*, vol. 53, pp. 3180-3190, Oct., 2005.



Malcolm M. Bibby received the B.Eng. and Ph.D. degrees in Electrical Engineering from the University of Liverpool, England in 1962 and 1965, respectively. He also

holds an MBA from the University of Chicago, U.S.A. His career includes both engineering and management. He was president of LXE Inc., manufacturer of wireless data communications products from 1983 to 1994. Thereafter he was president of NDI, a manufacturer of hardened handheld computers, for five years before retiring. He has been interested in the numerical aspects associated with antenna design for the last twenty-five years.



Andrew F. Peterson received the B.S., M.S. and Ph.D. degrees in Electrical Engineering from the University of Illinois, Urbana-Champaign in 1982, 1983 and 1986 respectively. Since 1989, he has been a member of the faculty of the School of Electrical

and Computer Engineering at the Georgia Institute of Technology, where he is now Professor and Associate Chair for Faculty Development. Within ACES, he served for six years (1991-1997) as a member of the Board of Directors, and has been the Finance Committee Chair and the Publications Committee Chair.

PML ABSORBING BOUNDARY CONDITIONS FOR THE MULTIREOLUTION TIME-DOMAIN TECHNIQUES BASED ON THE DISCRETE WAVELET TRANSFORM

C. Represa (*), C. Pereira (*), A.C.L. Cabeceira (**), I. Barba (**), J. Represa (**)

(*) Dpt. of Electromechanical Engineering, University of Burgos, 09001 Burgos, Spain

Phone: +34 947258830 FAX: +34 947258831 E-Mail: crepresa@ubu.es

(**) Dpt. of Electricity and Electron, University of Valladolid, 47011 Valladolid, Spain

Phone: +34 983423223 FAX: +34 983423225 E-Mail: ibarba@ee.uva.es

Abstract: The use of numerical methods to solve electromagnetic problems with open boundaries requires a method to limit the domain in which the field is computed. This can be achieved by truncating the mesh and setting certain numerical boundary conditions on the outer perimeter of the domain to simulate its extension to infinity. In this paper, the formulation of the perfectly matched layer (PML) is applied to the multiresolution time-domain technique (MRTD) to effectively simulate free-space. The PML region is modelled by means of the two-dimensional discrete wavelet transform. In addition, the numerical reflectivity of the PML medium is also investigated for a variety of thicknesses.

Keywords: Absorbing boundary conditions, PML, MRTD, DWT.

1. INTRODUCTION

Different wavelet-based discretizations for Maxwell equations have been developed in the very recent literature. These numerical methods are known as multiresolution time-domain (MRTD) techniques and its main point of interest is the intrinsic capability of wavelets to add higher spatial frequency contributions in the representation of the fields. These methods employ numerical analysis based on different wavelet functions like Battle-Lemarié [1], Haar [2], and Daubechies [3], and have been applied to several electromagnetic problems such as scattering, radiation, and integrated-circuit component modeling. Many of these applications involve modeling electromagnetic fields in an unbounded open space. It is well known that, since the computational domain is limited in space by storage limitations, a certain type of boundary condition, which is called absorbing boundary condition (ABC) must be implemented to effectively simulate open regions and having the capability to suppress numerical reflections of the outgoing waves.

Many absorbing boundary conditions have been proposed in past years [4]-[6], but since 1994, a new improvement has been made in this area by J.P. Berenger's technique designated as the perfectly matched layer or PML [7]. This technique is based on the introduction of a highly effective absorbing material medium to terminate the outer boundary of the space lattice. This nonphysical absorbing medium has a wave impedance less sensitive to the angle of incidence, polarization and frequency of outgoing waves, and therefore a perfectly matched interface is derived.

In this paper, the PML principle has been implemented into the multiresolution time-domain technique. This technique uses Daubechies compactly supported wavelet functions denoted as D_M [8], and the PML medium has been modelled using the discrete wavelet transform (DWT).

2. APPLICATION OF THE PML ABSORBER TO THE MRTD TECHNIQUE

A. Fundamentals of the PML theory

In the PML theory described in [7] it is assumed that the PML region is characterized by a free-space permittivity ϵ_0 and permeability μ_0 , and electric and magnetic conductivities σ and σ^* , respectively. Then, if the following PML relationship is satisfied

$$\frac{\sigma}{\epsilon_0} = \frac{\sigma^*}{\mu_0} \quad (1)$$

the impedance of the medium matches that of vacuum and no reflection occurs when a plane wave propagates normally across a vacuum-medium interface. Since sharp variations of conductivity can create numerical reflections, for a PML region of thickness δ , the conductivities are chosen to vary

from zero at the vacuum-layer interface to a maximum value σ_{MAX} at the outer side of the layer

$$\sigma(\rho) = \sigma_{MAX} \left(1 - \frac{\rho}{\delta}\right)^n, \text{ with } n = 2 \text{ for } 0 \leq \rho \leq \delta. \quad (2)$$

Usually the PML area is terminated with a PEC, thus the maximum value σ_{MAX} is determined by a designated apparent reflection coefficient R at normal incidence, which is given by the relationship [7]

$$R = \exp\left(-\frac{2\sigma_{MAX}\delta}{\varepsilon_0 c(n+1)}\right). \quad (3)$$

By choosing the theoretical reflection coefficient (typically $R = 10^{-4}$ or $R = 10^{-5}$) and the PML thickness δ , the maximum value σ_{MAX} can be obtained from (3).

B. Implementation of the PML absorber

In this section, we will analyze the implementation of the PML absorber into the MRTD scheme. This implementation does not involve a special treatment if scaling functions are used to expand the field components. Otherwise, if two or more resolution levels are applied, that is, scaling and wavelet functions are used to expand the field components, we must model the PML medium before its implementation into the algorithm. For simplicity in this presentation, let us assume a one dimensional problem. That is, the simplest case of a TEM plane wave propagating in free-space, with E_x and H_y fields, is considered. In order to simulate open boundaries, we will locate two PML areas of thickness δ at both ends, with an electric conductivity σ and a magnetic conductivity σ^* satisfying the relation (1) and with a parabolic spatial distribution, that is, a spatial profile like (2) with $n = 2$ (Fig. 1). Within the PML area, the equations to

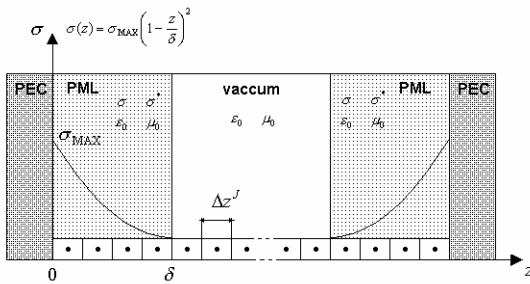


Fig. 1. Parabolic spatial distribution of σ and σ^* within the PML area.

solve are

$$\frac{\partial H_y}{\partial t} + \frac{\sigma^*}{\mu_0} H_y = -\frac{1}{\mu_0} \frac{\partial E_x}{\partial z} \quad (4.a)$$

$$\frac{\partial E_x}{\partial t} + \frac{\sigma}{\varepsilon_0} E_x = -\frac{1}{\varepsilon_0} \frac{\partial H_y}{\partial z}. \quad (4.b)$$

Thus, according to the exponential time stepping [9], these equations are discretized in time as

$$H_y^{n+\frac{1}{2}} = e^{-\frac{\sigma^* \cdot \Delta t}{\mu_0}} H_y^{n-\frac{1}{2}} - \frac{1}{\sigma^*} \left(1 - e^{-\frac{\sigma^* \cdot \Delta t}{\mu_0}}\right) \frac{\partial E_x^n}{\partial z} \quad (5.a)$$

$$E_x^{n+1} = e^{-\frac{\sigma \cdot \Delta t}{\varepsilon_0}} E_x^n - \frac{1}{\sigma} \left(1 - e^{-\frac{\sigma \cdot \Delta t}{\varepsilon_0}}\right) \frac{\partial H_y^{n+\frac{1}{2}}}{\partial z}. \quad (5.b)$$

According to the notation given in [8], an approximate solution at level J can be obtained using scaling functions of J -th order to expand each field component respect to space. The final set of discretized equations are expressed in matrix form as follows

$${}^{n+\frac{1}{2}}[H^\phi]^J = [\sigma_1^*]^J {}^{n-\frac{1}{2}}[H^\phi]^J - [\sigma_2^*]^J \frac{1}{\Delta z} [d^J]^n [E^\phi]^J \quad (6.a)$$

$${}^{n+1}[E^\phi]^J = [\sigma_1]^J {}^n[E^\phi]^J - [\sigma_2]^J \frac{1}{\Delta z} [d^J]^{n+\frac{1}{2}} [H^\phi]^J \quad (6.b)$$

where ${}^n[H^\phi]^J$ and ${}^n[E^\phi]^J$ are column vectors whose elements are the scaling coefficients at level J , evaluated at time $t = n\Delta t$, of the magnetic and electric field expansions, respectively. The matrix $[d^J] = \mathbf{D}^J$ is the derivative matrix at level J (Fig. 2) [8].

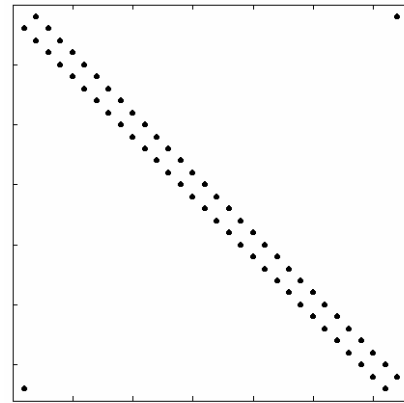


Fig. 2. Derivative matrix D^J : Only non zero elements have been plotted.

The matrices $[\sigma_1]^J$, $[\sigma_2]^J$, $[\sigma_1^*]^J$, and $[\sigma_2^*]^J$ are diagonal matrices whose elements are function of the time discretization interval Δt , the permittivity ϵ_0 , the permeability μ_0 , and the electric and magnetic conductivity, σ and σ^* , respectively, and are distinct from zero only at each point $z = k\Delta z^J = k2^{-J}\Delta z$ within the PML area of thickness $\delta = L\Delta z^J$. These matrices are given by the set of equations (7.a) to (7.d).

Now, the spatial resolution can be increased by adding wavelet functions to the field expansion. Therefore, adding wavelet functions of J -th order to

the field expansion results in an approximate solution at level $J+1$ with a spatial discretization interval Δz^{J+1} . The formulation of the fields within the PML region is written in matrix form as indicated in equation (8.a) and equation (8.b), where a derivative matrix at level $J+1$ (\mathbf{D}^{J+1}) [8] has been used, and the matrices related to the conductivity of the PML medium have been modeled using the two-dimensional discrete wavelet transform DWT_{2D} [10].

$$[\sigma_1]^J = \begin{bmatrix} \sigma_{10}^J & & & & \\ & \ddots & & & \\ & & \sigma_{1k}^J & & \\ & & & \ddots & \\ & & & & \sigma_{1L-1}^J \end{bmatrix}, \text{ where } \sigma_{1k} = \exp\left(-\frac{\sigma(k\Delta z^J) \cdot \Delta t}{\epsilon_0}\right) \quad (7.a)$$

$$[\sigma_2]^J = \begin{bmatrix} \sigma_{20}^J & & & & \\ & \ddots & & & \\ & & \sigma_{2k}^J & & \\ & & & \ddots & \\ & & & & \sigma_{2L-1}^J \end{bmatrix}, \text{ where } \sigma_{2k} = \frac{1}{\sigma(k\Delta z^J)} \left(1 - \exp\left(-\frac{\sigma(k\Delta z^J) \cdot \Delta t}{\epsilon_0}\right)\right) \quad (7.b)$$

$$[\sigma_1^*]^J = \begin{bmatrix} \sigma_{10}^{*J} & & & & \\ & \ddots & & & \\ & & \sigma_{1k}^{*J} & & \\ & & & \ddots & \\ & & & & \sigma_{1L-1}^{*J} \end{bmatrix}, \text{ where } \sigma_{1k}^* = \exp\left(-\frac{\sigma^*(k\Delta z^J) \cdot \Delta t}{\mu_0}\right) \quad (7.c)$$

$$[\sigma_2^*]^J = \begin{bmatrix} \sigma_{20}^{*J} & & & & \\ & \ddots & & & \\ & & \sigma_{2k}^{*J} & & \\ & & & \ddots & \\ & & & & \sigma_{2L-1}^{*J} \end{bmatrix}, \text{ where } \sigma_{2k}^{*J} = \frac{1}{\sigma^*(k\Delta z^J)} \left(1 - \exp\left(-\frac{\sigma^*(k\Delta z^J) \cdot \Delta t}{\mu_0}\right)\right). \quad (7.d)$$

$${}^{n+\frac{1}{2}} \begin{bmatrix} H^\phi \\ H^\psi \end{bmatrix}^{J+1} = \begin{bmatrix} d \sigma_1^* & \gamma \sigma_1^* \\ \beta \sigma_1^* & \alpha \sigma_1^* \end{bmatrix}^{n-\frac{1}{2}} \begin{bmatrix} H^\phi \\ H^\psi \end{bmatrix}^{J+1} - \begin{bmatrix} d \sigma_2^* & \gamma \sigma_2^* \\ \beta \sigma_2^* & \alpha \sigma_2^* \end{bmatrix} \frac{1}{\Delta z} \begin{bmatrix} d^J & \gamma^J \\ \beta^J & \alpha^J \end{bmatrix}^n \begin{bmatrix} E^\phi \\ E^\psi \end{bmatrix}^{J+1} \quad (8.a)$$

$${}^{n+1} \begin{bmatrix} E^\phi \\ E^\psi \end{bmatrix}^{J+1} = \begin{bmatrix} d \sigma_1 & \gamma \sigma_1 \\ \beta \sigma_1 & \alpha \sigma_1 \end{bmatrix}^n \begin{bmatrix} E^\phi \\ E^\psi \end{bmatrix}^{J+1} - \begin{bmatrix} d \sigma_2 & \gamma \sigma_2 \\ \beta \sigma_2 & \alpha \sigma_2 \end{bmatrix} \frac{1}{\Delta z} \begin{bmatrix} d^J & \gamma^J \\ \beta^J & \alpha^J \end{bmatrix}^{n+\frac{1}{2}} \begin{bmatrix} H^\phi \\ H^\psi \end{bmatrix}^{J+1} \quad (8.b)$$

The procedure depicted in Fig. 3 to obtain these matrices is as follows: first, we compute the σ -matrices corresponding to level $J+1$, that is, double sample points with a spatial discretization interval Δz^{J+1} (see Fig. 4). Then, we apply the one dimensional discrete wavelet transform in a successive manner to its rows and to its columns. This procedure results in a matrix composed of four submatrices arranged this way

$$\begin{bmatrix} d\sigma_1 & \gamma\sigma_1 \\ \beta\sigma_1 & \alpha\sigma_1 \end{bmatrix} = DWT_{2D}[\sigma_1]^{J+1} \quad (9.a)$$

$$\begin{bmatrix} d\sigma_2 & \gamma\sigma_2 \\ \beta\sigma_2 & \alpha\sigma_2 \end{bmatrix} = DWT_{2D}[\sigma_2]^{J+1} \quad (9.b)$$

$$\begin{bmatrix} d\sigma_1^* & \gamma\sigma_1^* \\ \beta\sigma_1^* & \alpha\sigma_1^* \end{bmatrix} = DWT_{2D}[\sigma_1^*]^{J+1} \quad (9.c)$$

$$\begin{bmatrix} d\sigma_2^* & \gamma\sigma_2^* \\ \beta\sigma_2^* & \alpha\sigma_2^* \end{bmatrix} = DWT_{2D}[\sigma_2^*]^{J+1}. \quad (9.d)$$

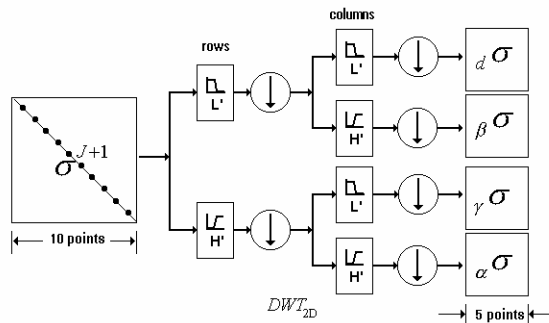


Fig. 3. Modelling of the σ -matrix using the two-dimensional discrete wavelet transform.

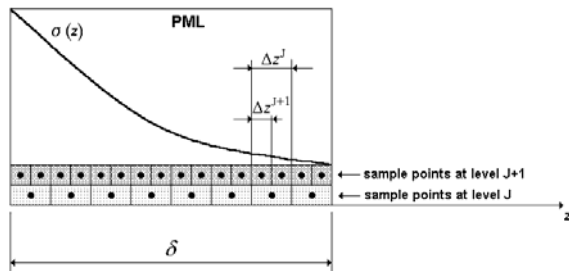


Fig. 4. Spatial discretization of the PML zone at level J and at level $J+1$.

3. NUMERICAL RESULTS

In order to evaluate the numerical effectivity of the implemented PML technique, the propagation of a TEM pulse, incident on the boundaries of the computational domain, has been simulated, and the response of the PML layer has been analyzed. A benchmark test has been done comparing the reflection coefficient S_{11} computed for three different thicknesses of the PML medium and using three different Daubechies wavelet functions (D_1 , D_2 , and D_3) in each case. The expansion of the field components with respect to space has been done using scaling and wavelet, and the time marching algorithm is then described by equations given in (8). Therefore, a numerical simulation with two levels of resolution has been done using scaling plus wavelet functions of zero order ($J = 0$). We have chosen a spatial discretization interval $\Delta z^1 = 1$ mm ($\Delta z = 2$ mm) and a time discretization interval $\Delta t = 3.34$ ps. The thicknesses of PML used in this test have been $\delta = 5\Delta z$, $\delta = 10\Delta z$, and $\delta = 15\Delta z$. A quadratic variation in PML conductivity is assumed for all cases, with maximum theoretical reflection coefficient of 10^{-4} . From equation (3), the maximum value σ_{MAX} obtained in each case was 3.67 S/m, 1.83 S/m, and 1.22 S/m, respectively. The reflection coefficient obtained in each case has been depicted in Figs. 5(a) through 5(c), corresponding to a PML thickness of $5\Delta z$, $10\Delta z$, and $15\Delta z$, respectively. As it can be appreciated from these figures, the scheme with field components expanded in terms of Daubechies wavelet functions D_1 is more sensitive to variations in the PML thickness. A great improvement is obtained with the increase of the thickness. Otherwise, the schemes with field components expanded in terms of Daubechies wavelet functions D_2 and D_3 are less sensitive to variations in the PML thickness and present a better behaviour than the other scheme when narrow thicknesses are used.

4. CONCLUSION

A procedure to implement PML absorbing boundary conditions into the MRTD scheme based on the discrete wavelet transform has been developed. This PML technique can be directly implemented into the algorithm when scaling functions are used, and for higher resolutions, the multilevel decomposition of the conductivity of the PML area needed has been done by means of the two-dimensional discrete wavelet transform. The numerical effectivity of the method has been also investigated for different thicknesses of the PML area, and using different

Daubechies wavelet functions for the expansion of the fields.

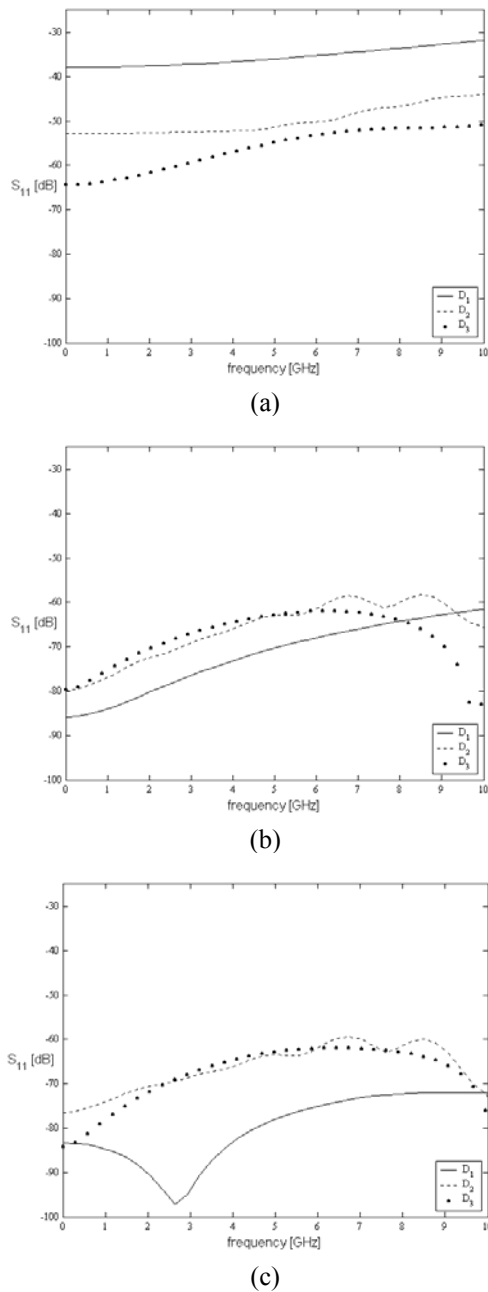


Fig. 5. Reflection coefficient S_{11} versus frequency computed using different Daubechies' wavelet functions and different thicknesses of PML: a) $\delta=5\Delta z$, b) $\delta=10\Delta z$, and c) $\delta=15\Delta z$.

5. ACKNOWLEDGEMENT

This work has been supported in part by Spanish "Comisión Interministerial de Ciencia y Tecnología". Contract/Grant number TIC2003-09677-C03-02.

6. REFERENCES

- [1] M. Krumpholz and L.P.B. Katehi, "MRTD: New Time-Domain schemes based on multiresolution analysis," *IEEE Trans. Microwave Theory Tech.*, vol. 44, no. 4, pp. 555–571, April 1996.
- [2] M. Fujii and W.J.R. Hoefer, "A 3-D Haar-Wavelet-Based Multiresolution Analysis Similar to the FDTD Method – Derivation and Application," *IEEE Trans. Microwave Theory Tech.*, vol. 46, no. 12, pp. 2463–2475, December 1998.
- [3] Y. W. Cheong, Y. M. Lee, K. H. Ra, and C. C. Shin, "Wavelet-Galerkin scheme of time-dependent inhomogeneous electromagnetic problems," *IEEE Microwave Guided Wave Lett.*, vol. 9, pp. 297–299, August 1999.
- [4] B. Engquist and A. Madja, "Absorbing boundary conditions for the numerical simulation of waves," *Mathematics Computation*, vol. 31, pp. 629–651, 1977.
- [5] G. Mur, "Absorbing boundary conditions for the finite-difference approximations of the time-domain electromagnetics field equations," *IEEE Trans. Electromagnetic Compatibility*, vol. 23, pp. 377–382, 1981.
- [6] K. K. Mei and J. Fang, "Superabsorption - A method to improve absorbing boundary conditions," *IEEE Trans. Antennas and Propagation*, vol. 40, pp. 1001–1010, September 1992.
- [7] J. P. Bérenger, "A perfectly matched layer for the absorption of electromagnetics waves," *J. Computational Physics*, vol. 114, pp. 185–200, 1994.
- [8] C. Represa, C. Pereira, I. Barba A.C.L. Cabeceira and J. Represa, "An approach to multiresolution in time domain based on the discrete wavelet transform," *ACES Journal*, vol. 18, no. 3, pp. 210–218, November 2003.
- [9] A. Taflove, *Computational Electrodynamics: The Finite-Difference Time-Domain Method*. Artech House, 1995.
- [10] S. G. Mallat, "A theory for multiresolution signal decomposition: The wavelet representation," *IEEE Trans. Pattern Analysis and Machine Intelligence*, vol. 11, no. 7, pp. 647–693, 1989.



César Represa was born in Medina del Campo, Spain, in 1971. He received the *Licenciado* degree in Physics from the University of Valladolid in 1995, and the PhD degree in 2001 from the University of Burgos. He was *Profesor Asociado* at the University of Burgos from 1997 to 2000. Since 2000 he has been

Assistant Professor at the University of Burgos. His research interest includes numerical methods in electromagnetics.



Carmen Pereira was born in Zamora, Spain, in 1951. She received the *Licenciado* degree in Physics in 1974, and the PhD degree in 1983, both from the University of Valladolid, Spain. She was Assistant Professor at the University of Valladolid from 1974 to 1985, and since 1985 has been *Profesor Titular*

in Electromagnetics at the Universities of Valladolid and Burgos. Her current research interest includes numerical methods in electromagnetics and microwave devices.



Ana Cristina L. Cabeceira was born in Pontevedra, Spain, in 1969. She received the *Licenciada* Degree on Physics in 1992, and the Ph. D. Degree in 1996, both from the University of Valladolid, Spain. From 1992 to 1999 she was Assistant Professor, then she

become *Profesora Titular* in Electromagnetism of the University of Valladolid. Her main research interests include numerical methods for Electromagnetism, as well as characterization of electromagnetics properties of materials.



Ismael Barba was born in Palencia, Spain, in 1970. He received his *Licenciado* degree in Physics from the University of Valladolid in 1993. He received his MA degree in Electronical Engineering in 1995, and his PhD in Physics in 1997, all from the same University. He was Assistant

Professor from 1994 to 1999, and since 1999, he is *Profesor Titular* in Electromagnetics in the University of Valladolid. His main research interest includes numerical methods in electromagnetics, and characterization of electromagnetics properties of materials.



José Represa was born in Valladolid, Spain, in 1953. He received the *Licenciado* degree in Physics in 1976, and the PhD degree in 1984, both from the University of Valladolid, Spain. He was Assistant Professor from 1976 to 1985, and since 1985

Professor in Electromagnetics at the University of Valladolid. His current research interest includes numerical methods in electromagnetics, characterization of electromagnetics properties of materials and microwave devices.

Response Bounds Analysis for Transmission Lines Characterized by Uncertain Parameters

S. Barmada, A. Musolino, and M. Raugi

Dipartimento Sistemi Elettrici e Automazione,
Universita di Pisa,
via Diotallevi 2, 56126, Pisa, Italy
sami.barmada@dssea.unipi.it

Abstract

This work is focused on the study of Multiconductor Transmission Lines (MTL) with uncertain parameters; i.e. the values of r , l , c and g can vary in an interval. The wavelet expansion in time domain is used in order to obtain an accurate and low cost representation of the line in terms of an algebraic system. The wavelet representation applied to the study of MTL with variation of the electrical parameters allow us to easily calculate a set of equivalent distributed generators, which represent the effects of the disturbance produced by the parameter variation. This analysis allows us to directly evaluate the response bounds related to the parameters uncertainties without performing repeated simulations (Montecarlo Method).

Keywords— **Uncertain Parameters, Transmission Lines, Time Domain Expansion.**

1 Introduction

The study of the effect of uncertainties in the electrical parameters of MTLs is an important yet complex topic; its importance comes from the fact that even the most developed industrial technologies cannot guarantee 100% accuracy in the construction of electronic devices, where transmission lines play a key role. Furthermore, the aging process is another cause of the parameters variation with respect to the nominal value. The effect of uncertainties can be studied by statistic Montecarlo techniques, that suffer of long computational times [1], by probabilistic approaches under some simplifying hypotheses [2], or by calculating a time domain sensitivity function (see for example [3]).

In this paper, the telegrapher equation is expanded in the wavelet domain; more precisely a time domain wavelet expansion is performed, as in [4], [5]. This technique is chosen because it

allows to represent the MTL through a sparse algebraic system, where the unknowns are the wavelet coefficients of voltages and currents, and the system matrix is a function of the electrical parameters of the MTL. The time domain solution is then obtained by simply solving the algebraic system and inverse transforming the results. It is noteworthy that the technique for the bounds definition proposed here, can be applied to any solution technique characterized by the expansion of the time variables on a basis functions, for example as performed in [6], resulting in a linear algebraic system.

This representation and some simple algebraic calculations performed on the system matrix let us calculate a set of equivalent time domain distributed generators, representing the effects of the uncertainties on the nominal output. The analysis of the magnitude of these equivalent distributed generators allows us to understand the effect of each single variation, and most important a simple procedure is defined to determine the response bounds due to the variation of the parameters in the given range. Insights of the physical meaning of the procedure and some results are shown.

2 Wavelet Based Modeling of Multiconductor Transmission Lines

As widely addressed in [4] the use of the Wavelet Expansion (WE) for the simulation of multiconductor transmission lines is a powerful tool, allowing fast and accurate simulations. The way the wavelet based model is obtained is the following: starting from the quasi-TEM MTL equations, the time variation of voltages and currents (which are variable with space and time coordinates) are expanded on a wavelet basis, yielding space variable vectors of coefficients. Time derivatives are dealt with by using the differential (or

integral, in case the MTL equations are first integrated) operator in the wavelet domain, which are constant and sparse matrices, calculated only once prior to the simulation.

In the so obtained equations only the space variable appears now; for this reason the line needs to be segmented in a number of cells, each represented by a sparse matrix, which can be cascade connected in order to obtain an algebraic system, which solved gives the value of the wavelet coefficients. The general form of the system is reported in equation (1)

$$\begin{bmatrix} \mathbf{I}_d & \mathbf{Ch} & 0 & \cdots & \cdots \\ 0 & \mathbf{I}_d & \mathbf{Ch} & \cdots & \cdots \\ 0 & 0 & \mathbf{I}_d & \cdots & \cdots \\ \vdots & \vdots & \vdots & \vdots & \vdots \\ 0 & \cdots & \cdots & \mathbf{I}_d & \mathbf{Ch} \\ \mathbf{BcL} & \cdots & \cdots & \cdots & \mathbf{Bc0} \end{bmatrix} \begin{bmatrix} \mathbf{v}_L \\ \mathbf{i}_L \\ \mathbf{v}_{L-1} \\ \mathbf{i}_{L-1} \\ \vdots \\ \mathbf{v}_j \\ \mathbf{i}_j \\ \vdots \\ \mathbf{v}_0 \\ \mathbf{i}_0 \end{bmatrix} = \mathbf{E} \quad (1)$$

where

$$\mathbf{E} = [0, 0, 0, 0, \dots, 0, 0, \dots, \mathbf{E}_L, \mathbf{E}_0]^T \quad (2)$$

and \mathbf{I}_d is the identity matrix of the proper dimension; \mathbf{v}_j and \mathbf{i}_j are the vectors of wavelet coefficients of voltages and currents at each cell (in particular \mathbf{v}_L , \mathbf{i}_L , \mathbf{v}_0 , \mathbf{i}_0 are the voltages and currents, respectively, at the two terminations of the line); \mathbf{BcL} and $\mathbf{Bc0}$ are the matrices of the boundary conditions (generators and terminations loads). The matrix \mathbf{Ch} , which contains the equation of a single cell, is analytically obtained and has the following expression

$$\mathbf{Ch} = \begin{bmatrix} 0 & (-l\mathbf{D} - r\mathbf{I}_d) \\ (-c\mathbf{D} - g\mathbf{I}_d) & 0 \end{bmatrix} \quad (3)$$

where \mathbf{D} is the wavelet representation of the differential operator, as previously discussed, and r, l, c, g are obviously the line parameters. As it can be easily observed, system (1) is an algebraic system characterized by a sparse matrix; hence it can be easily solved by iterative techniques. The known term of the system is characterized by having all zero entries except than the last

part, where the WE of the input signals (generator) is included (vectors \mathbf{E}_0 and \mathbf{E}_L).

Uniform and nonuniform transmission lines (with linear and nonlinear load) can be in this way conveniently solved, obtaining accurate solutions in lower CPU times if compared with standard step by step techniques.

At this stage frequency dependent transmission lines could not be included in the model. As a result of the further work performed by the authors, also frequency dependence of the parameters and proximity effect between the conductors have been included. The inclusion of these two important phenomena are presented in [5], in which starting from the original formulation presented in [7] and expressing the convolution between two functions in the wavelet domain, a convenient formulation is obtained. In particular, the algebraic system representing the MTL is obtained in the form of (1), in which the only difference is the presence of a constant matrix \mathbf{K} , function of the skin and proximity effect sensitive quantities (i.e. geometrical and physical characteristics of the line) simply included in the matrix \mathbf{Ch} as

$$\mathbf{Ch} = \begin{bmatrix} 0 & (-l\mathbf{D} - r\mathbf{I}_d - \mathbf{K}) \\ (-c\mathbf{D} - g\mathbf{I}_d) & 0 \end{bmatrix}. \quad (4)$$

As a conclusion to this section we underline that the use of WE for the solution of such problems, in our formulation allows the fast simulation of uniform, nonuniform, frequency dependent transmission lines; not being a frequency domain based method also nonlinearities can be easily included, as widely addressed in [4] and [5]. For this reason the proposed method could be conveniently used to perform Montecarlo procedures when uncertain parameters are considered, since the CPU time consumption of each run is lower if compared to standard techniques.

3 Response Bounds for MTL with Uncertain Parameters

In this section we define a technique for the evaluation of an upper and lower bound of the time domain response of a MTL when the per unit length parameters are uncertain. As stated in the introduction, this problem is of great importance, and nowadays the possibilities of dealing

with it are somehow limited, mainly consisting of Montecarlo procedures and statistical models based on some simplifying approximations. The procedure we propose here is based on the model of the MTL obtained as recalled in the previous section, and as it will be shown, the computational cost is reasonably low.

3.1 Definition of the Equivalent Sources

We start this section by considering the transmission line represented by the algebraic system (1), obtained by performing the WE of the MTL equations. We underline here that the proposed technique can be applied to any other numerical model where the time variation of voltages and currents is expanded on a basis of functions, as it is for example done in [6]; for this reason we refer to the general algebraic system (5)

$$\mathbf{A}\mathbf{x} = \mathbf{b} \quad (5)$$

where \mathbf{x} is the vector of unknown coefficients of voltages and currents at the port of each cell, in which the line is segmented and \mathbf{b} is a vector containing the input signal of the line.

In case of uncertainty of the line parameters, equation (5) can be seen as the representation of the MTL where the per unit length parameters assume the nominal value.

When a variation is considered, the new system can be written as

$$\tilde{\mathbf{A}}\tilde{\mathbf{x}} = \mathbf{b} \quad (6)$$

where $\tilde{\mathbf{A}}$ is the new matrix resulting from varied r, l, g, c ; $\tilde{\mathbf{x}}$ is the new solution and \mathbf{b} remains unchanged since the line is considered energized by the same signal. Equation (6) can be more conveniently written as

$$(\mathbf{A} + \Delta\mathbf{A})\tilde{\mathbf{x}} = (\mathbf{I} + \Delta\mathbf{A}\mathbf{A}^{-1})\mathbf{A}\tilde{\mathbf{x}} = \mathbf{b} \quad (7)$$

where the variation of the matrix \mathbf{A} is now evidenced. The solution to equation (7) can be written as

$$\tilde{\mathbf{x}} = \mathbf{A}^{-1}(\mathbf{I} + \Delta\mathbf{A}\mathbf{A}^{-1})^{-1}\mathbf{b}. \quad (8)$$

By comparing equations (5) and (8) it is easy to see that

$$\tilde{\mathbf{b}} = (\mathbf{I} + \Delta\mathbf{A}\mathbf{A}^{-1})^{-1}\mathbf{b} \quad (9)$$

can be seen as a new input vector for the line with the nominal values of the parameters, and the varied transmission line response can be calculated by solving the system

$$\mathbf{A}\mathbf{x} = \tilde{\mathbf{b}}. \quad (10)$$

This means that the effect of the parameters variation has been moved from the system matrix to the vector of the input signals, changing it from \mathbf{b} to $\tilde{\mathbf{b}}$.

As shown in [4] (and recalled in section II) the vector \mathbf{b} contains the imposed voltages and currents at the ports of each cell; since the line can be considered as excited only at the terminals, its entries are all zeroes except than the bottom part (representing the Wavelet Expansion of the feeding generator). On the contrary the new vector $\tilde{\mathbf{b}}$ is in general a full vector, and by inverse transforming it we obtain the time domain behavior of the distributed sources that take into account the effects of the parameters variation, which are zero for the nominal line.

It can be easily seen that the way the time domain equivalent generators are obtained is easy and straightforward, and requires low CPU time (due to the wavelet properties): the total cost is an inversion of a sparse matrix (the “nominal” matrix, hence to be performed only once, even if several evaluations need to be performed) and a linear system solution. An analysis of the waveform and the magnitude of the generators allows us to obtain an insight in the effect of the parameters variation, and how it affects the output variation with respect to the nominal value.

Let us suppose that the parameters vary in a range expressed by $r = r_n \pm \Delta x_r \%$, $l = l_n \pm \Delta x_l \%$, $g = g_n \pm \Delta x_g \%$, and $c = c_n \pm x_c \%$, where the subscript n is related to the nominal value. It is possible to evaluate the distributed sources for the worst case condition, i.e. for $r = r_n(1 + \Delta x_r/100)$ and $r_n = r_n(1 - \Delta x_r/100)$, and so on. Performing (for a single conductor line) this operation for the whole set of parameters we have to perform a matrix inversion and solve eight linear systems. The result is the set of vectors $\tilde{\mathbf{b}}_{r-}$, $\tilde{\mathbf{b}}_{r+}$, $\tilde{\mathbf{b}}_{l-}$, $\tilde{\mathbf{b}}_{l+}$, $\tilde{\mathbf{b}}_{g-}$, $\tilde{\mathbf{b}}_{g+}$, $\tilde{\mathbf{b}}_{c-}$, $\tilde{\mathbf{b}}_{c+}$. For each of them it is possible to calculate the vector $\mathbf{b}' = \tilde{\mathbf{b}} - \mathbf{b}$, isolating the effects of the variation from the input generator.

3.2 Bounds Definition

The most common way to define the bounds of the response in presence of parameter's uncertainty is to perform a Montecarlo procedure, by repeating several simulations with a random variation of the parameters. An alternative approach has been studied by the authors in [8], where the bounds have been calculated by a first order approximation of the sensitivity with respect to the variables. Here we propose a different approach, based on the previous definition of the vectors \mathbf{b} defined as follows.

Given a parameters' variation as expressed at the end of the previous section, we define the upper bound as related to a set of distributed sources constructed by adding up together the absolute values of the previously calculated vectors \mathbf{b}' , i.e.

$$\mathbf{b}_{upper} = |\mathbf{b}'_{r+}| + |\mathbf{b}'_{l+}| + |\mathbf{b}'_{g+}| + |\mathbf{b}'_{c+}| + |\mathbf{b}'_{r-}| + |\mathbf{b}'_{l-}| + |\mathbf{b}'_{g-}| + |\mathbf{b}'_{c-}| + \mathbf{b}. \quad (11)$$

In this way it is possible to obtain the upper bound of the response straightforwardly resolving system (5) with the known term previously calculated, i.e.

$$\mathbf{x}_{upper} = \mathbf{A}^{-1}\mathbf{b}_{upper} \quad (12)$$

which can also be written as

$$\mathbf{x}_{upper} = \Delta\mathbf{x} + \mathbf{x}. \quad (13)$$

The lower bound of the response can now be calculated with no need of a further simulation, i.e.

$$\mathbf{x}_{lower} = \Delta\mathbf{x} - \mathbf{x}. \quad (14)$$

The two vectors \mathbf{x}_{upper} and \mathbf{x}_{lower} must be inverse transformed giving the time domain bounds.

At this point it is important once again to underline the computational cost of the whole procedure: with a line with N conductors, there are $NP = 4 * (N - 1)$ line parameters which are supposed to vary. By the use of the proposed method the computational cost is the following:

- a simulation with the nominal values, at the cost of an algebraic system solution;
- a matrix inversion;

- $2NP$ matrix-vector products, as in (9), obtaining the the new known vectors;
- absolute value operation and a sum, as in (11);
- a simulation from which we determine the response bounds.

It is hence evident the very low computational cost of the method if compared with a standard Montecarlo procedure. It can be interesting to analyze how wide can be the range of variation of the parameters that still permits a reasonable evaluation of the bounds. Some qualitative considerations can be made: the proposed procedure allows us to obtain an estimate of the response bounds in the presence of uncertainties; the simple evaluation reported in (11) is of course valid in a certain range of variation. In particular, we implicitly infer that the variation of the vectors \mathbf{b} is monotonic in the range of variation of the parameters. Based on our experience the ranges of uncertainty in the parameters (due to aging or industrial tolerances) always satisfy the above mentioned requirement. It is noteworthy that a deeper analysis related to the wideness on the interval of uncertainty could be performed observing the magnitudes of the entries of matrix $\Delta\mathbf{A}$.

4 Numerical Results

In this section the results related to two different test cases are reported: first a simple bifilar line is considered, and a qualitative analysis of the equivalent sources, together with a comparison of the bounds obtained by the technique presented in [8] and by a Montecarlo procedure is shown. As a second test case a more complex 4 conductors line is chosen, showing the calculated bounds compared with a simulation technique.

4.1 Bifilar Line

The 2 conductors line is characterized by the following parameters:

$$\begin{aligned} r &= 200\Omega/m, & l &= 2.8\mu H/m, \\ c &= 1.2nF/m, & g &= 0S/m \end{aligned} \quad (15)$$

the line is characterized by a length of $L = 0.03$ m and is terminated at both ends on 50- Ω resistors. The feeding generator is a trapezoidal

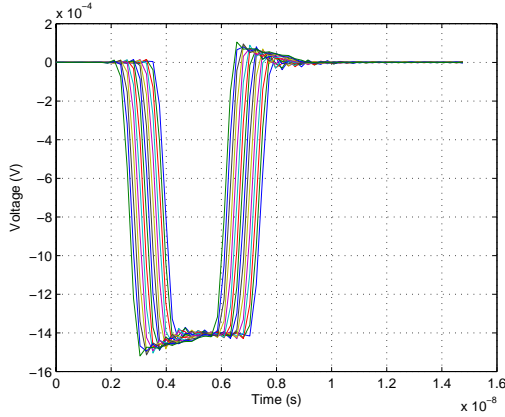


Figure 1: Distributed voltage sources related to the +10 % variation of r .

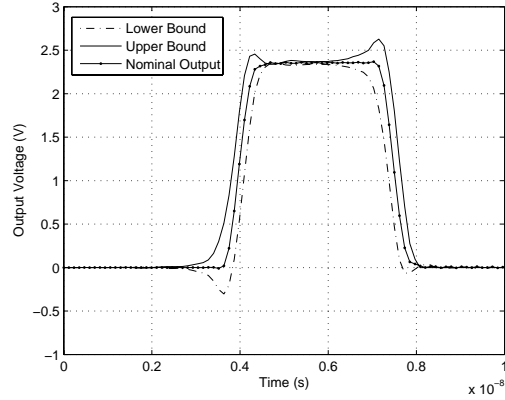


Figure 3: Calculated bounds and nominal output.

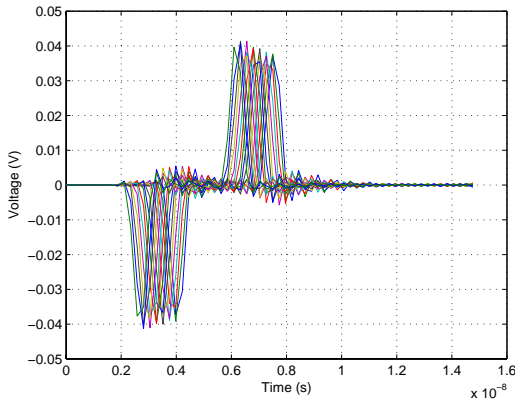


Figure 2: Distributed voltage sources related to the +10 % variation of l .

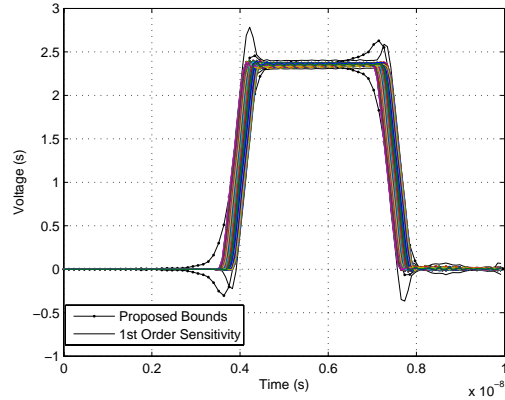


Figure 4: Calculated bounds and Montecarlo cloud.

pulse characterized by an amplitude of 5 V and a rise time of 0.5 ns. A variation of $\pm 10\%$ has been taken into account for all the parameters.

Figures 1 and 2 shows the time behavior of the distributed sources obtained considering a variation of resistance and inductance; analyzing the figure it is easy to verify the consistency of the obtained results and at the same time some conclusions can be drawn. In particular, we can see that the resistance variation mainly affects the steady state value of the voltages, while a variation of the inductance mainly influences the rise and fall time of the signal.

In a wider extent by performing a simple qualitative analysis on all the distributed sources re-

lated to all the parameters of a MTL it is possible to identify the most sensitive parameters.

Figure 3 shows the calculated bounds with respect to the result obtained by the nominal values of the parameters, while Fig. 4 shows a comparison between the bounds calculated by the proposed technique, with the bounds calculated as in [8] and with the Montecarlo cloud obtained performing 1000 random simulations.

Figures 3 and 4 show the accuracy of the method with respect to Montecarlo simulations.

4.2 Multiconductor Transmission Line

This second test case regards a 4 conductor transmission line, reported in Fig. 5

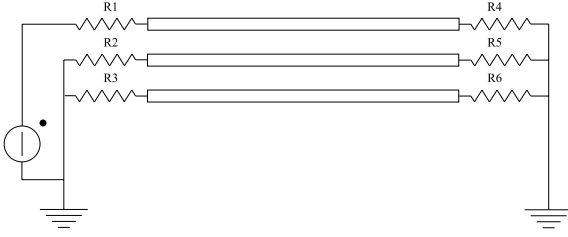


Figure 5: Multiconductor transmission line.

with the following parameters:

$$\mathbf{R} = \begin{vmatrix} 6 & 0 & 0 \\ 0 & 6 & 0 \\ 0 & 0 & 6 \end{vmatrix} \frac{\Omega}{m} \quad \mathbf{L} = \begin{vmatrix} 231 & 95 & 0 \\ 95 & 231 & 95 \\ 0 & 95 & 231 \end{vmatrix} \frac{nH}{m}$$

$$\mathbf{G} = \begin{vmatrix} 15.6 & 0 & 0 \\ 0 & 15.6 & 0 \\ 0 & 0 & 15.6 \end{vmatrix} \frac{\mu S}{m}$$

$$\mathbf{C} = \begin{vmatrix} 109 & -48 & 0 \\ -48 & 157 & -48 \\ 0 & -48 & 109 \end{vmatrix} \frac{pF}{m}$$

the line is characterized by a length of $L = 0.0156$ m while the values of the input and output resistances are: $R_1 = 30 \Omega$, $R_2 = 10 \text{ M}\Omega$, $R_3 = 30 \Omega$, $R_4 = 200 \text{ k}\Omega$, $R_5 = 60 \Omega$, $R_6 = 50 \text{ k}\Omega$.

Figures 6, 7, and 8 show the calculated bounds at the far end of the line (i.e. the voltages at the resistances R_4 , R_5 , and R_6 and the respective Montecarlo cloud calculated with 5000 random variation. The accuracy of the calculated bound can be easily seen in the figures.

A general comment can be made on the CPU time cost of the proposed method: as clearly addressed in section 3 the most relevant time consuming the activity is the inversion of the matrix \mathbf{A} , clearly depending on its dimension. The dimension of the above mentioned matrix depends on the frequency content of the input signal and the number of cells in which the line must be divided (more details can be found in [4]); these two parameters are related to the velocity of propagation of the signal along the line and the line length itself. The examples chosen contain typical signals and line length characteristics of high speed interconnects. In order

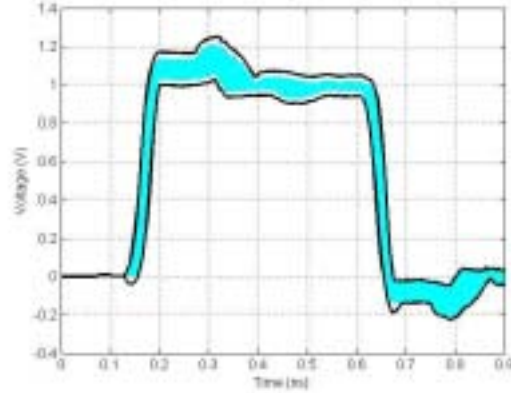


Figure 6: Calculated bounds and Montecarlo cloud for conductor 1.

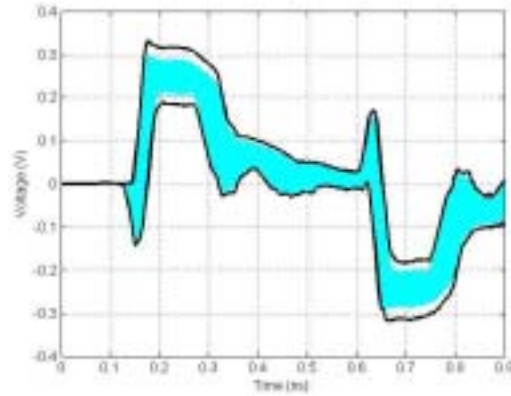


Figure 7: Calculated bounds and Montecarlo cloud for conductor 2.

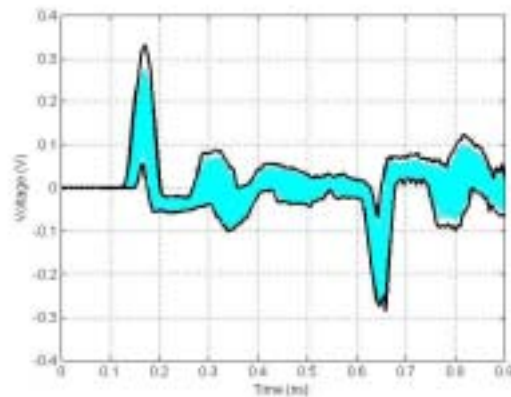


Figure 8: Calculated bounds and Montecarlo cloud for conductor 3.

to compare the proposed method and a Montecarlo procedure, it is necessary to remind an important difference: by the use of the proposed method the number of calculations (henceforth the CPU time) is determined, and allows us to find directly the bounds. As a matter of fact there is no apriori knowledge on the number of Montecarlo runs necessary to obtain a reasonable upper and lower limit, therefore the total number is chosen based on qualitative considerations. The comparison we have performed regard a number of Montecarlo simulations creating a cloud which is almost unchanged if we add another set of simulations. Under this assumption the proposed method is characterized by lowering the necessary CPU time of an order of magnitude and more.

5 Conclusion

In this paper a method for the analysis and evaluation of the response bounds of a Transmission Line characterized by uncertain parameters is shown. The bounds so obtained are compared with a Montecarlo simulation, showing the significance of the result.

Acknowledgment: This work is supported in part by the Italian Ministry of University (MIUR) under a Program for the Development of Research of National Interest (PRIN grant # 2004093025).

References

- [1] S. Pignari and D. Bellan "Statistical Characterization of Multiconductor Transmission Lines Illuminated by a Random Plane - Wave Field," Proceedings of IEEE International Symposium on Electromagnetic Compatibility, 2000, vol. 2, pp. 605 - 609, 21-25 Aug. 2000.
- [2] S. Shiran, B. Reiser, and H. Cory "A Probabilistic Model for the Evaluation of Coupling Between Transmission Lines," IEEE Trans. Electromagnetic Compatibility, vol. 35, pp. 387-393, Aug. 1993.
- [3] S. Lun, M. S. Nakhla, and Q-J Zhang, "Sensitivity Analysis of Lossy Coupled Transmission Lines," IEEE Transaction on Microwave Theory and Techniques, vol. 39, n. 12, pp. 2089 - 2099, December 1991.
- [4] S. Barmada and M. Raugi, "Transient numerical solution of nonuniform MTL equations with nonlinear loads by wavelet expansion in time or space domain," IEEE Trans. on Circuits and Systems, vol. 47, Issue 8, pp. 1178 - 1190, August 2000.
- [5] S. Barmada, A. Musolino, and M. Raugi "Wavelet Based Time Domain Solution of Multiconductor Transmission Lines with Skin and Proximity Effect," accepted for publication on IEEE Trans. EMC.
- [6] Y. S. Chung, T. K. Sarkar, B. H. Jung, M. Salazar - Palma, Z. Ji, S. Jang, and K. Kim, "Solution of Time Domain Electric Field Integral Equation Using the Laguerre Polynomials," IEEE Transaction on Antennas and Propagation, vol. 52, no. 9, pp. 2319 - 2328, September 2004.
- [7] G. Costache, "Transient Proximity Effect and Longitudinal Transient Parameters of a Bifilar Transmission Line," Rev. Roum. Sci. Techn. - Electrotechn. et Energ., vol. 16, no. 1, pp. 111-124, 1971.
- [8] S. Barmada, G. Becherini, A. Musolino, and M. Raugi, "A Sensitivity Approach to Determine the Response Bounds of Transmission Lines with Random Parameters," Proceedings of the 2004 IEEE International Symposium on Electromagnetic Compatibility, Santa Clara, USA, pp. 413 - 418, 9 - 13 August 2004.



Sami Barmada was born in Livorno, Italy, on November 18, 1970. He received the Master and Ph.D. degrees in electrical engineering from the University of Pisa, Pisa, Italy, in 1995 and 2001, respectively. From 1995 to 1997, he was with ABB Teknologi, Oslo, Norway, where he was involved with distribution network analysis and optimization. He is currently an Assistant Professor with the Department of Electrical System and Automation, University of Pisa, where he is involved with numerical computation of electromagnetic fields, particularly on the modeling of multiconductor transmission lines and to the application of wavelet expansion to computational electromagnetics. He was the technical chairman of the Progress In Electromagnetic Research Symposium (PIERS), Pisa, Italy, 2004 and has served as chairman and session organizer of international conferences.

Dr. Barmada was the recipient of the 2003 J F Alcock Memorial Prize, presented by The Institution of Mechanical Engineering, Railway Division, for the best paper in technical innovation.



Antonino Musolino was born in Reggio Calabria on January the 7th 1964. He received the Master degree in Electronic Engineering and the Ph. D degree in Electrical Engineering from the University of Pisa in 1990 and 1995 respectively. He is currently an Associate Professor of electrical engineering with the De-

partment of Electrical Systems and Automation, University of Pisa. His main research activities are the numerical methods for the analysis of electromagnetic fields in linear and nonlinear media, the design of special electrical machines and the application of the WE to computational electromagnetics.



Marco Raugi received the degree in Electronic Engineering from the University of Pisa in 1985 and the Ph. D. in Electrical Engineering from the Department of Electrical Systems and Automation in 1990. He is currently a full professor of Electrical Engineering. His research activity is in the numerical methods for the analysis of electromagnetic fields in linear

and nonlinear media. Main applications have been devoted to Non Destructive Testing, Electromagnetic compatibility in transmission lines, electromagnetic launchers. He is author of around 100 papers on international journals and conferences.

He was the general chairman of the International conference PIERS (Progress In Electromagnetic Research Symposium) 28-31 March 2004 in Pisa. He has been chairman of the Editorial Boards and he served as chairman and session organizer of international conferences. He has been recipient of the IEEE-IndustryApplicationSociety 2002 Melcher Prize Paper Award.

Analysis of Band-Pass Filter Characteristics in a Ferrite Device with Carbon Nanotube Electrodes

Toshihito Umegaki, Matsuto Ogawa, and Tanroku Miyoshi
 Department of Electrical and Electronics Engineering
 Kobe University
 Kobe City, 657-8501, Japan

ABSTRACT

We have studied magnetostatic waves excited and received by carbon nanotubes in the high-frequency band-pass filter on yttrium iron garnet (YIG). First, we have analyzed dispersion curves of magnetostatic waves in YIG based upon the magnetostatic approximation method. We have studied the characteristics of the band-pass filter where the high-frequency current flowing on single-wall CNTs may excite and receive directly magnetostatic waves in the ferrite film beneath them. Next, we have studied the device where the current is flowing on bundle CNTs. It is found that band-pass filter characteristics, such as the insertion loss (IL), the center frequency (f_0), and bandwidth (BW) are significantly controlled by both the chirality of the CNTs and the numbers of CNTs in the bundle CNTs. On these results, we have proposed a novel ferrite device which may work to discriminate the chirality of CNTs and the numbers of CNTs in a bundle CNT. In this device, the chirality or the number of CNTs in a bundle CNT may be measured by means of the band-pass characteristics via the wavelength of the operating magnetostatic waves.

I. INTRODUCTION

Many types of magnetostatic wave devices have been reported as small microwave devices such as delay lines, filters, and oscillators, where operating wavelength is ranging from 10^{-5} m to 10^{-8} m [1, 2]. Their operating frequency depends on the dimension of electrodes to excite magnetostatic waves and it is restricted within fabrication accuracy. On the other hand, since the discovery of carbon nanotubes (CNTs) [3], the properties of CNTs have attracted much interest due to their unique structures and promising electrical properties. Especially the diameters of CNTs can be

easily controlled as small as several nanometers. In addition, the great advantage of CNTs over conventional materials is that they have ballistic conductivities and diameter control can be achieved by means of self-organization. As an application to make use of the characteristics, we investigate the High-Frequency (HF) filters using CNTs for electrodes to excite magnetostatic waves in ferrite devices. Compared with the case of the HF filters with conventional metal-electrodes [1, 2], the CNT electrodes may improve the operating frequency up to THz region. As the operating frequency of such devices increases, we can realize devices which can handle more information than conventional ones.

In this paper, we study magnetostatic waves excited and received by CNTs in yttrium iron garnet (YIG). We analyze dispersion curves of magnetostatic waves in YIG based upon the magnetostatic approximation method. It is found that, at the frequency in THz domain, magnetostatic waves propagate with wavelength as short as several nanometers. We study the band-pass filter characteristics of the YIG device where the high-frequency current flowing on single-wall CNTs, which are treated as cylindrical electrodes but reflecting the results of quantum transport analysis. The CNT electrodes may excite and receive directly magnetostatic waves in the ferrite film beneath them.

In the following sections, we study the high frequency characteristics of the device based upon the magnetostatic approximation. The dispersion curves show the operating frequency is ranging from GHz region to THz, and the wavelength is ranging longer than a few nm. Then we analyze the filter characteristics of the device with single wall CNTs or with bundle CNTs. In order to excite and receive magnetostatic waves efficiently by high frequency current in CNTs, we may have to construct practical structures of CNTs to overcome

attenuation of magnetostatic waves and to avoid other electromagnetic couplings between CNTs.

In this paper, however, we treat the CNT as realistic quantum wire. It is found that band-pass filter characteristics, such as the insertion loss (IL), the band-pass center frequency (f_0), and bandwidth (BW) are significantly controlled by both the chirality of the CNTs and the numbers of CNTs in a bundle CNT, which are used as electrodes. On these results, we propose a novel ferrite device, which will discriminate the chirality of CNTs and the numbers of CNTs in a bundle CNT. In this device, the chirality or the number of CNTs in a bundle CNT may be measured by means of the band-pass characteristics via the wavelength of the operating magnetostatic waves. In the final section, conclusions are summarized.

II. A FERRITE DEVICE WITH SINGLE-WALL CARBON NANOTUBES

A. Theoretical Analysis

Consider a ferrite based HF filter using CNTs for electrodes to excite magnetostatic waves, whose schematic structure is shown in Fig. 1. The high-frequency current flowing through one single-wall CNT excites directly magnetostatic waves in a ferrite film and the other single-wall CNT receives them. Although the distance between the two electrodes v is not a parameter in our calculation, we may have to control v in practical structures of CNTs to overcome attenuation of

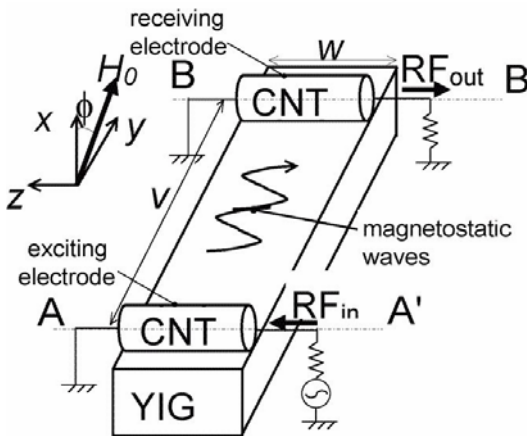


Fig.1. The schematic structure of the device: Straight lines A-A' and B-B' coincide with the axes of CNTs supplied with RF_{in} and detected RF_{out} current, respectively. The line A-A' is parallel to the line B-B' and distance between them is v .

magnetostatic waves and to avoid other electromagnetic couplings between CNTs. Fig. 2 shows a cross-sectional view of the device model with a single-wall CNT, where r is radius of the CNT, and t is the thickness of YIG. We can grow CNTs in various processes. One of the processes provides good selectivity to control the single-walled CNT average diameter within angstrom accuracy. In the future, we will be able to grow CNTs not only with the selectivity but also in good accuracy of the growing position [4,5] to fabricate this kind of devices.

When a bias magnetic field H_0 is applied obliquely from x -axis of the angle ϕ (Fig. 1), magnetic permeability is expressed in the following tensor form (see Appendix B):

$$\hat{\mu} = \begin{pmatrix} \bar{c}^2 + \mu\bar{s}^2 & (1-\mu)\bar{s}\bar{c} & -j\kappa\bar{s} \\ (1-\mu)\bar{s}\bar{c} & \bar{s}^2 + \mu\bar{c}^2 & j\kappa\bar{s} \\ j\kappa\bar{s} & -j\kappa\bar{c} & \mu \end{pmatrix}, \quad (1)$$

where

$$\bar{c} \equiv \cos \phi, \quad \bar{s} \equiv \sin \phi, \quad (2)$$

$$\mu = \frac{[\omega_h + \omega_{he}(\beta)][\omega_h + \omega_j + \omega_{he}(\beta)] - \omega^2}{[\omega_h + \omega_{he}(\beta)]^2 - \omega^2}, \quad (3)$$

$$\kappa = \frac{\omega\omega_j}{[\omega_h + \omega_{he}(\beta)]^2 - \omega^2}, \quad (4)$$

$$\omega_{he}(\beta) = 2\omega_e(1 - \cos \beta a), \quad (5)$$

$$\omega_j = \gamma\mu_0 M_0, \quad \omega_h = \gamma\mu_0 H_0, \quad \omega_e = \gamma\mu_0 H_e. \quad (6)$$

β is the propagation constant of magnetostatic waves, ω is angular frequency, γ is called the gyromagnetic ratio which is 1.759×10^{11} m²/Wbs, H_0 is the bias magnetic field, M_0 is the saturation magnetization, a is the lattice constant of YIG which is 1.238nm, and H_e corresponds to Weiss's molecular field [6], respectively.

In the present simulation, current flow and displacement current are negligibly small compared to $|\nabla \times \mathbf{H}|$, where \mathbf{H} is the magnetic field. Therefore we can adopt the magnetostatic approximation [2, 7, 8]. In the magnetostatic approximation, \mathbf{H} is represented as the gradient of a magnetostatic potential ψ , namely

$$\mathbf{H} = -\nabla\psi$$

The magnetic flux density \mathbf{B} is $\mu_0 \hat{\mu} \mathbf{H}$. From

$$\nabla \cdot \mathbf{B} = 0$$

we can obtain an equation for ψ .

$$\begin{aligned} & (\bar{c}^2 + \mu\bar{s}^2) \frac{\partial^2 \psi}{\partial x^2} + 2(1 - \mu)\bar{c}\bar{s} \frac{\partial^2 \psi}{\partial x \partial y} \\ & + (\bar{s}^2 + \mu\bar{c}^2) \frac{\partial^2 \psi}{\partial y^2} = 0. \end{aligned} \quad (7)$$

To solve this equation for our device configuration, we have sliced the region under consideration into $2N$ pieces parallel to the y -axis as shown in Fig. 2. Then we can obtain ψ as follows:

$$\psi_{2N} = \int_{-\infty}^{\infty} A_{2N} e^{-|\beta|(x-r)} e^{-j\beta y} d\beta, \quad (8a)$$

$$\psi_i = \int_{-\infty}^{\infty} (A_i e^{-|\beta|\bar{x}_i} + B_i e^{|\beta|\bar{x}_i}) e^{-j\beta y} d\beta, \quad (8b)$$

$$\bar{x}_i = x - x_i, \quad (i = 0, 1, 2, \dots, 2N - 1), \quad (8c)$$

$$x_i = r \cos \frac{\pi i}{2N}, \quad (8d)$$

$$\psi_{\bar{x}} = \int_{-\infty}^{\infty} (C e^{jk_1^x \bar{x}} + D e^{jk_2^x \bar{x}}) e^{-j\beta y} d\beta, \quad (8e)$$

$$\bar{x} = x + r, \quad (8f)$$

$$k_l^x = |\beta| \frac{(1 - \mu)\bar{s}\bar{c}s \mp \sqrt{-\mu}}{\bar{c}^2 + \mu\bar{s}^2}, \quad (l = 1, 2), \quad (8g)$$

$$s = \frac{\beta}{|\beta|}, \quad (8h)$$

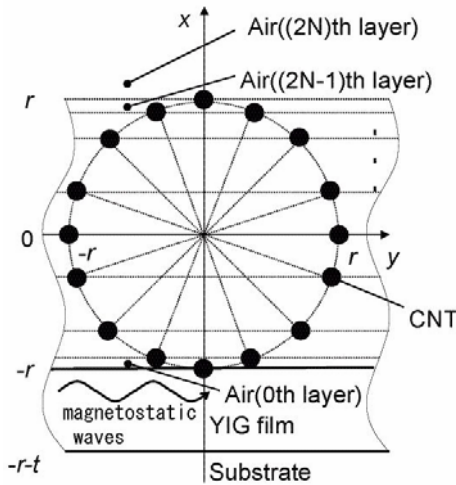


Fig. 2. A cross-sectional view of the schematic device model with a single-wall CNT centering around the line A-A' or B-B'. The magnetostatic wave is excited by the CNT (A-A') and received by B-B' as shown in Fig. 1. In the cross section, we apply the Boundary Conditions at the infinite current points, normal (x) component of magnetic flux density is continuous and tangential (y) components of magnetic field and current are continuous. The closed circles are current points arranged at equal interval on a circle centered at the origin of x and y coordinates.

$$\psi_{\text{sub}} = \int_{-\infty}^{\infty} E e^{|\beta|(x+r+t)} e^{-j\beta y} d\beta, \quad (8i)$$

where the index of each ψ represents to be each region along the x -axis and t is the thickness of the YIG film as shown in Fig. 2. The subscript f stands for the YIG film and sub is the substrate. A_i and B_i ($i=0, 1, \dots, 2N$) are amplitudes in i th air layer decaying toward + and - x directions, respectively. C and D are amplitudes in the YIG film propagating toward + and - x directions, respectively. E is amplitude in the substrate decaying toward - x direction.

Applying the continuity conditions of the normal (x) components of the magnetic flux density (B_i^x , $i=0, 1, \dots, 2N$, B_f^x, B_{sub}^x), tangential y components of the magnetic field (H_i^y , $i=0, 1, \dots, 2N$, H_f^y, H_{sub}^y) and current density J_i^z , $i=0, 1, \dots, 2N$ as

$$\begin{aligned} H_{2N}^y - H_{2N-1}^y &= J_{2N}^z \Big|_{x=r}, \\ B_{2N}^x - B_{2N-1}^x &= 0 \Big|_{x=r}, \\ H_i^y - H_{i-1}^y &= J_i^z \Big|_{x=x_i}, \\ B_i^x - B_{i-1}^x &= 0 \Big|_{x=x_i}, \quad (i = 0, 1, \dots, 2N - 1) \\ H_0^y - H_{\bar{x}}^y &= J_{\bar{x}}^z \Big|_{x=-r}, \\ B_0^x - B_{\bar{x}}^x &= 0 \Big|_{x=-r}, \\ H_{\bar{x}}^y - H_{\text{sub}}^y &= 0 \Big|_{x=-r-t}, \\ B_{\bar{x}}^x - B_{\text{sub}}^x &= 0 \Big|_{x=-r-t}. \end{aligned} \quad (9)$$

The continuity conditions (9) are valid for the magnetostatic waves [2]. Substituting Eqs.(8) into Eqs.(9), we obtain the amplitude D in Eq.(8e) as

$$D = - \frac{\sum_{k=0}^{2N} e^{|\beta|(-r+x_k)} \tilde{J}_k^z(\beta)}{4\pi j \beta F(\omega, \beta) p(\omega, \beta)}, \quad (10)$$

where

$$\tilde{J}_k^z(\beta) \equiv \int_{-\infty}^{\infty} J_k^z e^{j\beta y} dy, \quad (11)$$

F and p will be shown in Eq. (13). All other amplitudes can be expressed in terms of D . For example, the amplitude C can be expressed as

$$C = \frac{jk_2^x - |\beta|}{-jk_1^x + |\beta|} e^{j(k_1^x - k_2^x)t} D. \quad (12)$$

When we take $F(\omega, \beta)$ as a zero, it should be calculated for the next two cases.

i) $k_3^x > 0$ or, for example, $\phi = 0$ (see Fig. 1),

$$\begin{aligned} F(\omega, \beta) &= \tan \frac{k_3^x t}{2} - \frac{1}{\sqrt{-\mu}}, \\ P(\omega, \beta) &= \frac{2 \cos^2 \frac{k_3^x t}{2}}{(\frac{\mu}{\sqrt{-\mu}} - 1)} e^{-\mu k_3^x t} (\tan \frac{k_3^x t}{2} + \sqrt{-\mu}). \end{aligned} \quad (13a)$$

ii) $k_3^x < 0$,

$$\begin{aligned} F(\omega, \beta) &= \tan \frac{k_3^x t}{2} + \sqrt{-\mu}, \\ P(\omega, \beta) &= \frac{2 \cos^2 \frac{k_3^x t}{2}}{(\frac{\mu}{\sqrt{-\mu}} - 1)} e^{-\mu k_3^x t} (\tan \frac{k_3^x t}{2} - \frac{1}{\sqrt{-\mu}}); \end{aligned} \quad (13b)$$

where $k_3^x = \frac{1}{2}(k_2^x - k_1^x)$. Although ϕ can be set any

value, we set ϕ is zero throughout the paper for simplicity. CNTs with chiralities $(n, 0)$ and (n, n) are called *zig-zag* and *armchair* types, respectively [9]. Since the current density is generally constant around the circumference of the single-wall CNT [10], it can be written as

$$J_i^z = \begin{cases} \frac{I_0}{4N} \delta(y), & i=0 \\ \frac{I_0}{4N} \sum_{\pm} \delta(y \pm y_i), & i=1, \dots, 2N-1 \\ \frac{I_0}{4N} \delta(y), & i=2N \end{cases} \quad (14a)$$

$$y_i = r \sin \left(\frac{\pi i}{2N} \right), \quad i=0, 1, 2, \dots, 2N-1, \quad (14b)$$

where I_0 is the amplitude of the total current flowing through the CNT, $\delta(y)$ is the Dirac delta function. Then the amplitude D is expressed as follows using Bessel's integration formalism (see Appendix):

$$D = -\frac{I_0 e^{-l\beta r}}{4\pi j \beta F(\omega, \beta) P(\omega, \beta)}. \quad (15)$$

From Eqs. (8) and (15), the magnetostatic potential ψ can be determined as a residue with the pole of $F(\omega, \beta)$.

The electromagnetic power flowing different regions has been obtained using Poynting's theorem as

$$P^y = \frac{1}{2} \text{Re} \left[\int_{-\infty}^{\infty} (-j\omega \psi^* B^y) dx \right], \quad (16)$$

where ψ^* is the complex conjugate of ψ . From this power, the radiation resistance R^\pm is defined as

$$R^\pm(\omega) = \frac{2P^y w}{I_0^2} \Big|_{s=\pm 1}, \quad (17)$$

where w is the length of the CNT electrodes. The insertion loss IL is basically defined as the ratio of

the input power and the output one of the device. It is a figure of merit of the device which is expressed as

$$IL = 10 \log \frac{[R_g + R^+(\omega) + R^-(\omega) + R_c]^2}{4R_g R^+(\omega)}. \quad (18)$$

In Eq. (18), R_g is the source resistance (50Ω). From the analysis of quantum transport in CNT [10], R_c is obtained as $1/2G_0$, where G_0 is the quantum

conductance $2e^2/h$. $R^\pm(\omega)$ in Eq. (18) includes only the 1st order standing wave along the thickness of the YIG film, respectively. Note that the quantum conductance is included in Eq. (18), since we have used CNT as excitation electrodes. The propagation loss, and the reactance of the CNTs are neglected for simplicity. We evaluate insertion loss as one of the characteristic values of the device.

B. Numerical results

Figure 3 shows the simulated dispersion curves of magnetostatic waves propagating in y -direction of the device. In Fig. 3, the angle ϕ is set to 0, the thickness of YIG is 10nm, $\mu_0 M_0$ is 0.17T, and $\mu_0 H_0$ is 0.1T, respectively. The upper limit of the dispersion curves can be determined by the condition where the phase shift among each magnetization must be less than π . Then the operating frequency is limited less than 5THz. As the wavelength becomes 2.5nm, the operating frequency is 10^3 times as high as that in the present magnetostatic wave devices [1,2]. This high frequency operation can be achieved because Weiss's molecular field H_e strongly enhances the bias magnetic field. The solid line in Fig. 3 is a dispersion curve when $\mu_0 H_e$ is 46T [6]. The dotted dashed line and the broken line in Fig. 3 are the dispersion curves when $\mu_0 H_e$ is $\pm 10\%$ larger than 46T, respectively.

Figure 4 shows the evidence in support of the validity of our calculation. We have applied our simulation model to a ferromagnetic material (nickel) and obtained the dispersion curves shown in Fig. 4. The solid line is obtained for the Weiss's molecular field of 317T [11], and the other two curves are for $\pm 10\%$ larger field, respectively. The closed circles are reported experimental dispersion relation of the magnetostatic waves propagating in Ni [12]. Our results agree with the experimental results, although both the theoretical and experimental data are for Ni. Since our simulation

is based on the same theory ([11] and Appendix B) for spin magnetization that can be equally applied to ferromagnetic materials, the magnetostatic waves can be also excited in YIG in the frequency range obeying the dispersion curves predicted in Fig. 3. In order to excite magnetostatic waves effectively in the device configuration shown in Fig. 1, the width or diameter of the excitation electrode must be precisely designed and fabricated shorter than the wavelength of the magnetostatic waves [7]. In our case, since the wavelengths are ranging from several to a hundred nm, CNT electrodes are suitable for the excitation of the magnetostatic waves in the similar way as realized in the conventional devices [2,7].

Figure 5 is the simulated frequency dependence of the insertion loss (IL). In this figure, we have assumed zig-zag type CNTs for the electrodes with the metallic chirality $(n,0)$, where $n=30, 45, 90,$ and $120,$ respectively, and w is $1\mu\text{m}$. As seen, this device works as a high-frequency band-pass filter

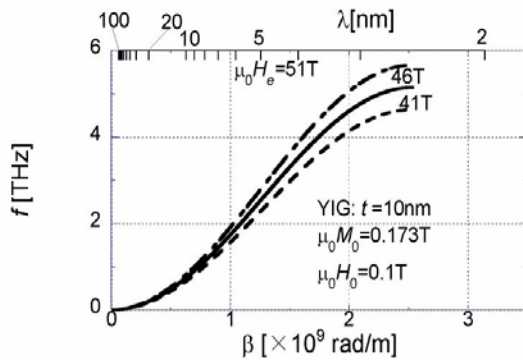


Fig. 3. Dispersion curves of the magnetostatic waves in THz domain excited in the YIG: Three dispersion curves are plotted. The solid line is obtained for Weiss's molecular field $\mu_0 H_e$ of 46T, and the other two curves are for $\pm 10\%$ larger field, respectively.

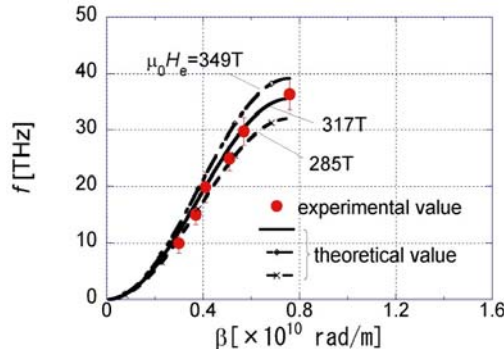


Fig. 4. Comparison of experimental dispersion curves with those obtained from the present simulation in Ni.

(BPF) in THz domain. Three characteristic values can be defined to specify the characteristics of this device: the minimum insertion loss IL_{\min} , the center frequency f_0 , and the bandwidth BW where IL is less than $IL_{\min} + 3\text{dB}$. When n is 30, we obtain $IL_{\min}=24.1\text{dB}$, $f_0=5.14\text{THz}$, and $BW=0.02\text{THz}$ (solid line), respectively. On the other hand, when n is 120, these values become $IL_{\min}=24.1\text{dB}$, $f_0=0.61\text{THz}$, and $BW=0.19\text{THz}$ (broken line), respectively.

Figure 6 shows the dependence of f_0 and BW on the chirality n of the CNTs. From this figure, it is found that when n , in other words, the diameter of the CNT increases, operating wavelength becomes longer and f_0 decreases. Taking the relationship between n and f_0 into account, we can design the characteristics of the BPF by means of the diameter of the CNT. However, since the IL is too large for practical application, we will analyze the characteristics of the BPF with bundle CNTs in the next section to improve the IL characteristics.

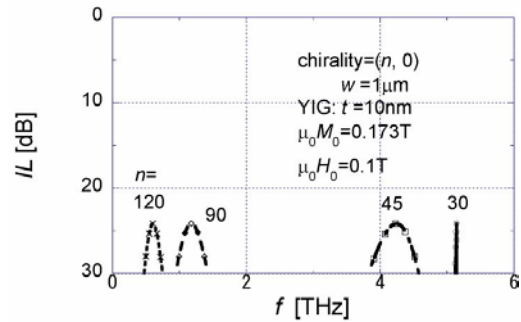


Fig. 5. The frequency dependence of the insertion loss IL for various n : When $n=120$, it is found that $f_0=0.60\text{THz}$ and $BW=0.19\text{THz}$, respectively. When $n=90, 45,$ and 30 , we can find f_0 and BW in the same way.

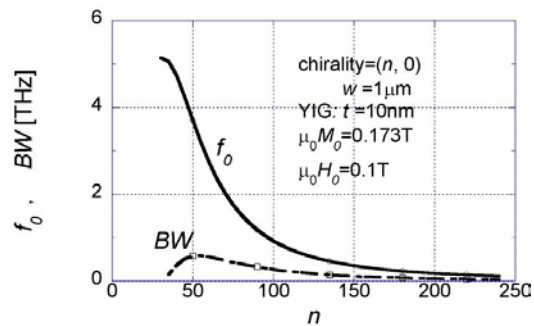


Fig. 6. The chirality (n)-dependence of the center frequency f_0 and bandwidth BW of the device: The f_0 monotonously decreases as n increases, whereas the BW becomes the maximum value as n is near 50.

III. A FERRITE DEVICE WITH BUNDLE CARBON NANOTUBES

A. Theoretical analysis of bundle carbon nanotubes

We consider the schematic structure of the device with the bundle CNTs instead of single-wall CNTs for electrodes of the HF filter as shown in Fig. 7 in order to improve the performance. Figure 8 shows a cross-sectional view of the device model with a bundle CNT, where r is the radius of each single-wall CNT, m is the numbers of CNTs along x and y -axes, respectively.

Same as the previous section, to solve Eq. (7) for the device configuration, we have sliced the region into $2mN$ pieces parallel to the y -axis as shown in Fig. 8. Then we can obtain ψ in each slice as follows:

$$\psi_{2mN} = \int_{-\infty}^{\infty} A_{2mN} e^{-|\beta|[x-(2m-1)r]} e^{-j\beta y} d\beta \quad (19a)$$

$$\psi_i = \int_{-\infty}^{\infty} (A_i e^{-|\beta|(x-x_i)} + B_i e^{|\beta|(x-x_i)}) e^{-j\beta y} d\beta \quad (19b)$$

$$i = 0, 1, 2, \dots, 2mN - 1, 2mN \quad (19c)$$

$$x_i = -r \cos \frac{\pi i}{2N} (-1)^{int(\frac{i-1}{2N})} + 2r \cdot int(\frac{i-1}{2N}), \quad (19d)$$

$$\psi_{\pm} = \int_{-\infty}^{\infty} (C e^{jk_1^{\pm}(x+r)} + D e^{jk_2^{\pm}(x+r)}) e^{-j\beta y} d\beta \quad (19e)$$

$$k_l^{\pm} = |\beta| \frac{(1-\mu)\sqrt{\epsilon} s \mp \sqrt{-\mu}}{\epsilon^2 + \mu s^2}, \quad (l=1,2) \quad (19f)$$

$$s = \frac{\beta}{|\beta|}, \quad (19g)$$

$$\psi_{\text{sub}} = \int_{-\infty}^{\infty} E e^{|\beta|(x+r+t)} e^{-j\beta y} d\beta, \quad (19h)$$

where the index of each ψ represents each region along the x -axis in Fig. 8.

Applying the same continuity conditions as in Eq. (9), we determine the amplitude D in Eq. (19e) as

$$D = - \frac{\sum_{i=0}^{2mN} e^{|\beta|(x_0-x_i)} \tilde{J}_i^z(\beta)}{4\pi j \beta F(\omega, \beta) p(\omega, \beta)}, \quad (20)$$

where J_i^z is given by the following equation instead of Eq. (14a).

$$J_i^z = \begin{cases} I_0 \sum_{j=1}^m \frac{\delta(y-y_{i,j,1})}{4m^2 N}, & i = 0, 2mN \\ I_0 \sum_{j=1}^m \frac{\delta(y-y_{i,j,1})}{2m^2 N}, & i = 2N, \dots, 2(m-1)N \\ I_0 \sum_{j=1}^m \sum_{k=1}^2 \frac{\delta(y-y_{i,j,k})}{4m^2 N}, & i = \text{others} \end{cases} \quad (21)$$

where

$$y_{i,j,k} = r \left[2(j-1) - (-1)^k \sin \frac{\pi i}{2N} \right]. \quad (22)$$

The amplitude D is expressed as follows using Bessel's integration formalism same as the derivation of Eq. (15):

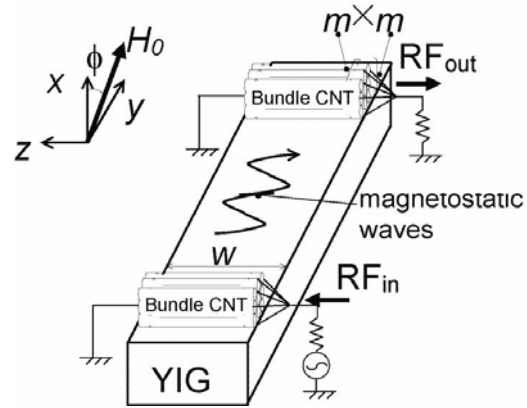


Fig. 7. The schematic structure of the device: The high-frequency current flowing through one bundle CNT excites directly magnetostatic waves in a ferrite film and the other bundle CNT receives them. Each bundle CNT consists of the m^2 parts of the single-wall CNTs arranged along x and y directions, respectively.

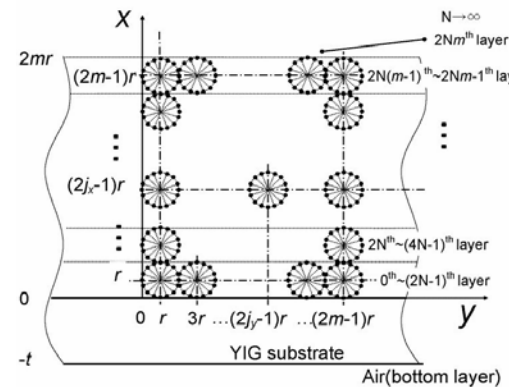


Fig. 8. A cross-sectional view of the schematic device model with a bundle multi-wall CNT: The m^2 CNTs, each of which is same as shown in Fig. 2, are aligned along x and y directions, respectively.

$$D = -\frac{I_0 \sum_{l'=1}^m e^{2j(l'-1)\beta r} \sum_{l=1}^m e^{-2(l-1)\beta r} e^{-l\beta r}}{4\pi m^2 j \beta F(\omega, \beta) p(\omega, \beta)}. \quad (23)$$

All other amplitudes can be expressed in terms of D . From Eqs. (19), and (23), the magnetostatic potential ψ can be obtained as a residue with the pole of $F(\omega, \beta)$. The electromagnetic power flowing in different regions, the radiation resistance R_c^\pm , and the insertion loss IL are given by Eqs. (16), (17), and (18), respectively. In Eq. (18), R_c is given by $1/2m^2G_0$ for the bundle CNT. R_g and other conditions are same as the case of single-wall CNT electrodes as shown in previous section.

B. Numerical results

Figure 9 shows the frequency dependence of the IL . In Fig. 9, the product of the chirality n and the numbers of the CNTs m is kept to be constant, that is $nm=300$. We assume the bundle zig-zag type CNTs have the metallic chirality $(300/m, 0)$ with the parameter $m=1, 10, 20, 50$, respectively. When $m=1$, we have found $IL_{\min}=27.5\text{dB}$ and $f_0=4.4\text{THz}$

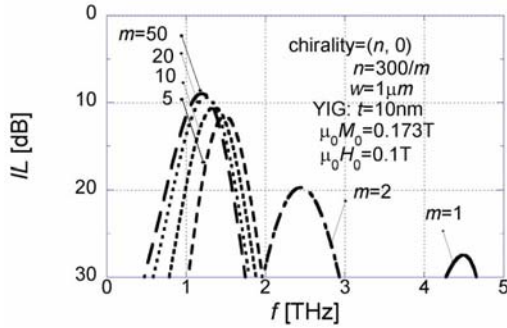


Fig. 9. The frequency dependence of the insertion loss IL for various m : When $m=50$, it is found that $IL_{\min}=9.0\text{dB}$, $f_0=1.2\text{THz}$ and $BW=0.4\text{THz}$, respectively. When $m=20, 10, 5, 2$, and 1 , we can find IL_{\min}, f_0 , and BW in the same way.

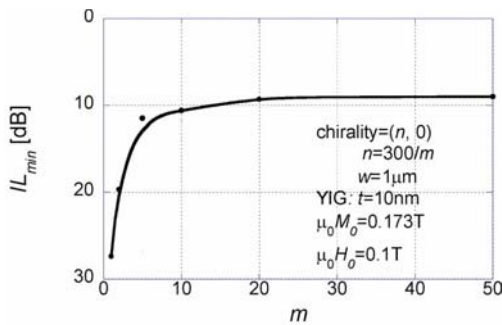


Fig. 10: The m -dependence of the minimum insertion loss IL_{\min} : The IL_{\min} monotonously increases as m increases.

(solid line in Fig. 9). On the other hand, when $m=50$, it is found that $IL_{\min}=9.0\text{dB}$ and $f_0=1.2\text{THz}$

(broken line in Fig. 9). Note that the insertion loss IL is significantly improved with the use of the bundle CNTs compared with the case of the single-wall CNT electrodes.

Figure 10 shows the m -dependence of the IL_{\min} . From this figure, it is found that when m and the dimension of the bundle CNT increase, IL_{\min} becomes smaller. Because there is a relation between IL_{\min} and impedance matching and the matching condition is improved by R_c in Eq. (18), we can improve both the IL and the impedance matching condition by using the bundle CNTs instead of single-wall CNTs. Figure 11 shows the m -dependence of f_0 . When m or the dimension of the bundle CNT increases, operation wavelength becomes longer and f_0 decreases. But f_0 is almost independent of m when m becomes larger than 20.

Since we have kept the product nm to be constant ($nm=300$), the main reason of this m -dependence is that only CNTs on the surface of the YIG substrate efficiently excite the magnetostatic

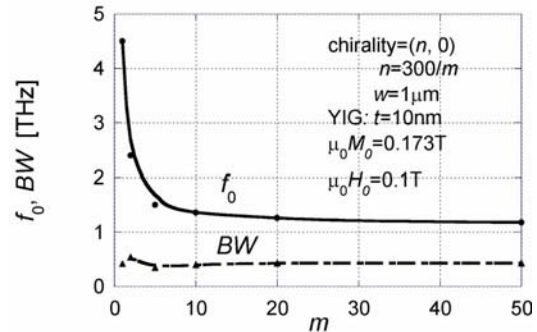


Fig. 11. The m -dependence of the f_0 and BW : The f_0 monotonously decreases as m increases, whereas the BW is almost independent of m .

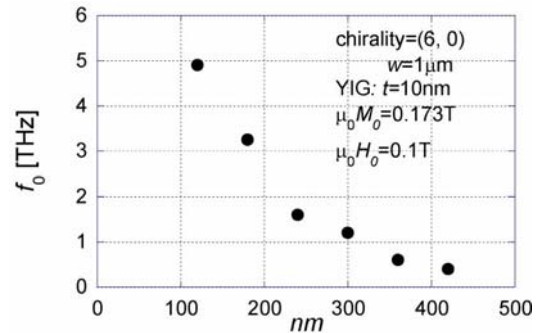


Fig. 12. The nm -dependence of the f_0 : The f_0 monotonously decreases as the product nm increases.

waves, but on the other hand, CNTs far from the surface are less effective for the excitation. When the numbers m is less than 20, f_0 strongly depends on m since each CNT has a large diameter and the excitation mainly occurs at the point of contact between each CNT and the YIG surface. On the other hand, as the number m becomes larger, the diameter of each CNT becomes smaller and the distance between each contact point becomes smaller. When m exceeds 20, the excitation occurs almost everywhere on the YIG surface because the distance between each contact point is less than 1.2nm. Therefore, even when m becomes larger than 20, the characteristics do not change drastically.

On the contrary, the product nm significantly affects the performance of the device. Figure 12 shows the nm dependence of the f_0 . The product nm has the obvious relations with the f_0 and we can design the characteristics of the BPF by means of dimension of the bundle CNT. Reversely, these characteristics enable us to discriminate nm by measuring the IL_{\min} , f_0 , and BW of the BPF. The BPF with the bundle CNTs has the relationship between n and f_0 due to the same reason as the single-wall CNTs, the characteristics of the BPF can be determined by means of the dimension of the bundle CNT. That is, this device may work as a discriminator of the number of CNTs and diameter of the each CNT in the bundle, respectively.

From Figs. 10 and 11, operating frequency f_0 reaches nearly 1 THz but the minimum insertion loss IL_{\min} is about 9dB when m is 50. We may then realize an oscillator with operating frequency up to one THz if we could use a circuit made of an amplifier and a feedback loop whose total gain is more than 9dB.

IV. CONCLUSION

We have analyzed dispersion curves of magnetostatic waves in YIG excited by CNT electrodes based upon the magnetostatic approximation method. It is found that such magnetostatic waves have the wavelength as small as several nanometers and operate at the frequency in THz domain. We have verified our calculation by comparing with experimental data in Ni. We have studied the band-pass filter characteristics of the YIG device where the high-frequency current flowing on single-wall CNTs. The characteristics

of IL -frequency, IL_{\min} , f_0 and BW have been evaluated varying the diameter or the chirality of the CNT. As a result, it is found that we can design the BPF by means of diameter of the CNT and improve the operation frequency into THz region.

To reduce the IL for practical application, we have proposed a BPF with bundle CNTs as electrodes. IL_{\min} is found to be improved from 27.5dB to 9.0dB by using bundle CNTs with $m=50$ instead of single-wall CNTs.

On these results, we have proposed a novel ferrite device which will operate as a discriminator of the chirality of CNTs and the number of CNTs in a bundle CNT. In this device, the chirality and the number of CNTs in a bundle CNT may be measured by means of the band-pass characteristics via operating wavelength.

From the m -dependence of the IL_{\min} , f_0 , and BW , we have proposed feasibility to realize an oscillator up to one THz, where we need a circuit consisting of an amplifier and a feedback loop whose total gain is more than 9dB.

ACKNOWLEDGEMENT

The author would like to acknowledge Drs. S. Uemura in Noritake Co., Limited and M. Kusunoki in Japan Fine Ceramics Center for their helpful discussion.

APPENDIX A: DERIVATION OF AMPLITUDE D

The right hand side of Eq.(10) can be expressed as the integrated form when N goes to infinity:

$$\begin{aligned} & \lim_{N \rightarrow \infty} \sum_{i=0}^{2N} e^{|\beta|(-r+x_i)} \tilde{J}_i^z(\beta) \\ &= \frac{I_0}{\pi} \int_0^\pi e^{|\beta|r(-1+\cos x)} \cos(\beta r \sin x) dx \end{aligned} \quad (A1)$$

Applying the Bessel's integration formalism to the R.H.S. of Eq. (A1), we obtain

$$\begin{aligned} & \frac{I_0}{\pi} \int_0^\pi e^{|\beta|r(-1+\cos x)} \cos(\beta r \sin x) dx \\ &= I_0 e^{-|\beta|r} J_0(0) \end{aligned} \quad (A2)$$

where $J_0(0)$ is the 0-th Bessel function. Noting $J_0(0) = 1$, Eq.(A2) can be expressed as

$$w \lim_{N \rightarrow \infty} \sum_{k=0}^{2N} e^{i\beta(-r+x_k)} \tilde{J}_k^z(\beta) = I_0 e^{-|\beta|r}. \quad (\text{A3})$$

Finally the amplitude D can be expressed as

$$D = -\frac{I_0 e^{-|\beta|r}}{4\pi j\beta F(\omega, \beta) p(\omega, \beta)}. \quad (\text{A4})$$

APPENDIX B: DERIVATION OF THE ADDITIONAL FREQUENCY DUE TO THE SPIN INTERACTION

Consider a schematic model with an array of 1-dimensional electronic spins as shown in Figure 13. The motion of equation for the magnetization \mathbf{M} of the spin can be described as follows similar to Eq. (16) in [11]:

$$\frac{d\mathbf{M}_i}{dt} = -\gamma\mu_0 \mathbf{M}_i \times \mathbf{H}_i, \quad (\text{B1})$$

where i implies the site of the spin. The exchange magnetic field which acts on the i -th spin is

$$\mathbf{H}_i = \lambda(\mathbf{M}_{i-1} + \mathbf{M}_{i+1}), \quad (\text{B2})$$

where λ corresponds to the Weiss's molecular field. In general, the magnetization \mathbf{M}_i can be represented in the polar coordinate as

$$\mathbf{M}_i = M_s(\sin\theta_i \cos\psi_i, \sin\theta_i \sin\psi_i, \cos\theta_i). \quad (\text{B3})$$

Assuming that the motion of electronic spins is in the equilibrium, θ_i is nearly equal 0 when the high-frequency magnetization is quite smaller than the bias magnetization, and the phase-difference between neighboring electrons $\Delta\psi$ is constant, we can obtain the followings, respectively:

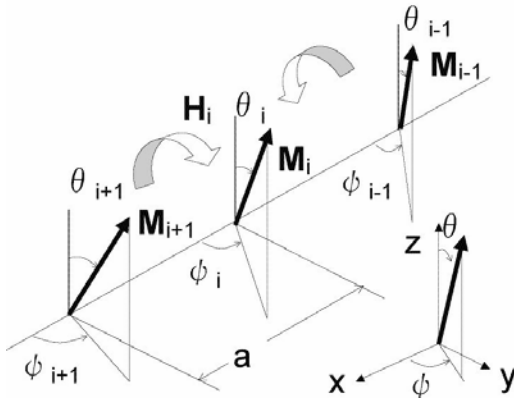


Fig. 13: Schematic model of the spin-exchange's addition to the resonance frequency of the ferrite in bias magnetic field with z-direction.

$$\frac{d\theta_i}{dt} = 0, \quad (\text{B4a})$$

$$\theta_i = \theta_{i+1} = \theta_{i-1} \cong 0, \quad (\text{B4b})$$

$$\Delta\psi \equiv \psi_{i+1} - \psi_i \cong \psi_i - \psi_{i-1} \equiv k_x a, \quad (\text{B4c})$$

where k_x is the wave number of magnetostatic wave, a is the distance between neighboring electronic spins in Figure 13. These assumptions are similar to those adopted in the derivation of spin waves in the literature [11]. Substituting Eqs. (B2), (B3) and (B4) into Eq. (B1), we can obtain

$$\frac{d\psi_i}{dt} = 2\gamma\mu_0 \lambda M_s (1 - \cos k_x a). \quad (\text{B5})$$

When $H_e = \lambda M_s$ and $\omega_{he}(\beta) \equiv d\psi/dt$, Eq. (B5) becomes

$$\omega_{he}(\beta) = 2\gamma\mu_0 H_e (1 - \cos k_x a), \quad (\text{B6})$$

which is added to the magnetic resonance frequency ω_h of conventional permeability and the permeability becomes as shown in Eqns. (3) and (4).

REFERENCES

- [1] P. C. Fletcher, C. Kittel, "Consideration on the Propagation and Generation of Magnetostatic Waves and Spin Waves," *Phys. Rev.*, vol. 120, pp. 2004-2006 (1960); M. Nakajima, "The microwave engineering," *Morikita publishing*, 1989 (in Japanese).
- [2] S. N. Bajpai, R. L. Carter, and J. M. Owens, "Insertion Loss of Magnetostatic Surface Wave Delay Lines," *IEEE Trans.* vol. MTT-36, pp. 132-136, 1988.
- [3] S. Iijima, "Helical Microtubules of Graphitic Carbon," *Nature (London)*, vol. 354, pp.56-58, 1991.
- [4] S. Lim, D. Ciuparu, C. Pak, F. Dobek, Y. Chen, D. Harding, L.D. Pfefferle, and G. Haller, "Synthesis and Characterization of Highly Ordered Co-MCM-41 for Production of Aligned Single Walled Carbon Nanotubes (SWNT)," *J. Phys. Chem. B*, vol. 107, no. 40, pp. 11048-11056, 2003.
- [5] Xu-Hui Sun, Chi-Pui Li, Wing-Kwong Wong, Ning-Bew Wong, Chun-Sing Lee, Shuit-Tong Lee, and Boon-Keng Teo, "Formation of Silicon Carbide Nanotubes and Nanowires via Reaction of Silicon (from Disproportionation of Silicon Monoxide) with Carbon Nanotubes," *J. Am. Chem. Soc.*, vol. 124, pp. 14464-14471, 2002.
- [6] R. Bauminger, S. G. Cohen, A. Marinov, and S. Ofer, "Study of the Internal Fields Acting on Iron Nuclei in Iron Garnets, Using the

- Recoil-Free Absorption in Fe57 of the 14.4-keV Gamma Radiation from Fe57," Phys. Rev., vol. 122, pp. 743-748, 1961.
- [7] Y. Ishikawa, T. Nomoto, T. Okada, S. Shinmura, F. Kanaya, S. Ichiguchi and T. Umegaki, "A Signal-to-Noise Enhancer with Extended Bandwidth Using Two MSSW Filters and Two 90° Hybrids," IEICE Trans. Electron., vol. E78-C, no. 8, pp. 1026-1032, 1995.
- [8] P. R. Emtage, "Interaction of magnetostatic waves with a current," J. Appl. Phys., vol. 49, pp. 4475-4484, 1978.
- [9] R. Saito, G. Dresselhaus and M. S. Dresselhaus, "Trigonal warping effect of carbon nanotubes," Phys. Rev., vol. B61, pp. 2981-2990, 2000.
- [10] T. Umegaki, M. Ogawa, Y. Makino, and T. Miyoshi, "Quantum Transport in Carbon Nanotubes with Arbitrary Chirality," Memoirs Graduate School Science & Technology, Kobe University, vol. 22-A, pp. 103-114, 2004.
- [11] C. Kittel, "Introduction to Solid State Physics (seventh edition)," John Wiley and Sons, Inc., 1996.
- [12] H. A. Mook and D. McK. Paul, "Neutron-Scattering Measurement of the Spin-Wave Spectra for Nickel," Phys. Rev. Lett., vol. 54, no. 3, pp. 227-229, 1985.



T. Umegaki received the B.E. and M.E. degrees from Kyoto Institute of Technology, Japan, in 1991 and 1993, respectively. He joined Murata Manufacturing Co., Ltd., Kyoto, Japan, in 1993 and had engaged in development of radio-frequency devices until 2001. He is currently pursuing the Ph.D. degree in graduate school of science and technology, Kobe University, Japan.



M. Ogawa received the B.E., M.E., and Dr. of Eng. degrees in electronic engineering from the University of Tokyo, Tokyo, Japan, in 1980, 1982, and 1985, respectively. In that year, he became a research associate at the Department of Electronics, Kobe University. From 1992 to the end of 1993, he was on leave at IBM T.J. Watson Research Center in New York as a Visiting Scientist. He is now a full Professor at Kobe University. He has been engaged in research on nano-scale MOS devices, quantum devices, and photo-electronic devices. He is a member of the IEEE and the Japan Society of Applied Physics.



T. Miyoshi received the B.S. in electrical engineering from the University of Tokyo, Tokyo, Japan, in 1967, and the M.S. and Ph.D. degree in electronics engineering from the University of Tokyo, Tokyo, Japan in 1969 and 1972, respectively. In 1972 he was appointed Lecturer, and from 1974 to 1987, he was an Associate Professor in the Department of Electronics Engineering, Kobe University, Kobe, Japan, where he is presently a Professor. He has been engaged in research of electromagnetic-wave theory, microwave integrated circuits, and light-wave electronics. His current research includes quantum transport modeling in nanostructures. In 1976 he was a Visiting Scholar at McGill University, Montreal, Que., Canada. From 1982 to 1984, he was a Visiting Scientist at Bell Laboratories, Holmdel, NJ. He is a member of the IEEE and the Japan Society of Applied Physics. He received a Yonezawa Award in 1974 and an Outstanding Book Award in 1977 both from the Institute of Electronics, Information and Communication Engineers in Japan.

An Alternative Method for Determining the Antenna Factor of a Monopole

Bahattin TÜRETKEN

The Scientific and Technical Research Council of Turkey (TUBITAK)
National Research Institute of Electronics and Cryptology , EMC & TEMPEST Test Center
P.O. Box.74, 41470 Gebze, Kocaeli, TURKEY)
e-mail:bahattin@uekae.tubitak.gov.tr

Abstract - In this study, the standard methods of monopole antenna calibration are interrogated and the use of alternative methods is investigated. For this purpose, the GTEM cell has been used for two standard identical monopole antenna calibrations. The dummy antenna ($\approx 10\text{pF}$ by ANSI, $\approx 12\text{pF}$ by CISPR), which is suggested as standard methods in ANSI C.63.5 and CISPR 16.1.4 are not appropriate to simulate the actual monopole. So Manufacture Antenna Simulator (MAS) has been used as an alternative equivalent circuit substitution method (ECISM) of the rod. Good agreement between GTEM measurement and ECISM is observed. Calibrations with standard and alternative methods are performed and the reliability of these methods is discussed in the frame of the measurement results.

Keywords - Antenna calibration, GTEM cell, monopole antenna, equivalent circuit substitution method.

I. INTRODUCTION

Monopole antennas are commonly used for radiated emission measurements in the frequency range 10 kHz to 30 MHz. In EMC compliance testing, the accuracy of calibration plays an important role in the rod antenna range. Determining the antenna factor (AF) is a major step in making accurate field strength measurements for EMC compliance. There are well-established antenna calibration methods [1] (ANSI C.63.5/1998) to calculate these antenna factors at open area test sites (OATS). However, alternative methods utilizing different test setup and sites, like GTEM Cell (Gigahertz Transverse ElectroMagnetic) [2, 3] and Full Anechoic Chamber (FAC), (SAE ARP 958,1999) are also brought forth in recent years [4].

The most common method of calibrating rod antennas is the Equivalent Capacitance Substitution Method (ECSM). In this method, a dummy antenna consisting of a capacitor equal to the self-capacitance of the rod or monopole is used instead of the actual rod. The value of the capacitor should be calculated according to the CISPR 16-1-4 [5]. It is not possible to simulate the right interaction of the rod antenna (including monopole, ground plane, coupling/amplifier unit) with the site ground using the dummy antenna. The insertion loss of capacitor decreases as the value of capacitor decreases. That is the point that the correct value of capacitor plays important key role on the antenna factor. In practice, calibration procedure of the radiated emission test (RE102) according to MIL-STD-461E [6] requires the substitution of the rod element of the monopole antenna with 10 pF capacitor and

application of a signal at a level 6 dB below the limit. The measured signal level in the receiver should, in this method, be between ± 3 dB amplitude range of the applied signal level. However, this is not the case in many calibration measurements performed. That is, calibration with 10 pF capacitor does not fit the manufacture data. In most cases the capacitor method is accurate to within $\pm 2\text{dB}$, but breaks down above about 10 MHz [7].

Other method of monopole calibrations given by at the National Institute of Standards and Technology (NIST) at open area test site is based on using a transmitting monopole to generate a known electromagnetic field at the site of the antenna under test (AUT). If the separation distance is not large enough, the incident field is not constant along the length of the AUT; this introduces the non-planarity error in the determination of the antenna factor. There is also another effect known as mutual impedance coupling of the antenna [8].

Once upon a time, TEM cells have been used for determining antenna factors for low frequency antennas, monopoles, loops and higher frequency probes. This calibration method has some limitations because of the upper cut-off frequency of the Cell indeed.

II. ALTERNATE CALIBRATION PROCEDURES AND MEASUREMENTS

With deficiencies of these methods in mind one has to take other methods should in to account. These methods are GTEM cell and Equivalent Circuit Substitution Method (ECISM) The aim of this work is to investigate the possibility of alternative calibration methods for monopole. This paper shows an alternate method determining antenna factor of a monopole in GTEM cell, and gives consistent comparative data.

As an alternative test site, GTEM cells have been proposed for small antenna measurements [9]. Since the field strength inside the GTEM cell is well correlated to the input power, the antenna factor can be measured accurately provided that the antenna size is not bigger than the test volume, at a point where the field strength is uniform and can be precisely determined. The procedures of antenna calibration for monopole in GTEM 1750 cell (MEB GTEM 1750, the height of maximum test volume is 1.75 m, DC to 1 GHz, nominal impedance is 50 ohm, VSWR is 1:1.5, field uniformity; $< \pm 4$ dB) is to place the monopole antenna at the center of the test

volume, aligned in such a way that the linearly polarized antenna is oriented vertically (perpendicular to the septum) in the linearly polarized test volume between the septum and the floor of the GTEM cell (Fig. 1).

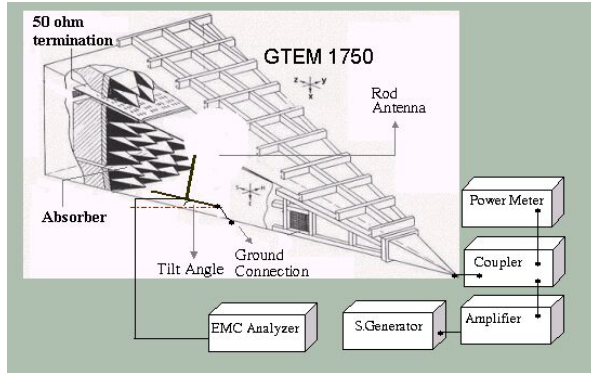


Fig. 1. Test setup for determining the antenna factor in GTEM cell.

The field strength inside GTEM Cell is given by

$$E = \frac{V_i}{h} \tag{1}$$

where

- E : Electric Field Strength (Volts/meter),
 - V_i : Input RF Voltage (Volts),
 - h : Septum Height (meter),
- and the definition of antenna factor is

$$AF = 20 \log\left(\frac{E}{V_0}\right) \tag{2}$$

where

- AF : Antenna Factor (m^{-1}),
- V_0 : Antenna output voltage (Volts).

Combining (1) and (2) yields

$$AF = 20 \log(V_i) - 20 \log(V_0) + 20 \log(1/h) . \tag{3}$$

Whereby equation (3) gives the antenna factor of the rod. An EMC Analyzer (Agilent 7405), a signal generator (R&S SMY01), a power meter (R&S NRVD), a power amplifier (AR), a directional coupler and MEB GTEM 1750 were used in calibration process. Two identical 41 inch R&S antennas (Rod#1, Rod#2) have been calibrated in the frequency range 10 kHz to 30 MHz. For the verification of the antenna factor obtained using GTEM cell and ECISM Measurements, the same antennas were also calibrated using standard methods (Fig. 2).

We also checked the dummy antenna consisting of a capacitor equal to the self-capacitance of the rod or monopole used in place of the actual rod by using SNEC (Super Numerical Electromagnetic Code Ver. 2.55) for the reliability of ECISM Method (Fig. 3). We observe good agreement between SNEC data and CISPR data. ANSI data is approximately 2 dB lower than other data in this frequency range.



Fig. 2. Test setup of ECISM calibration method.

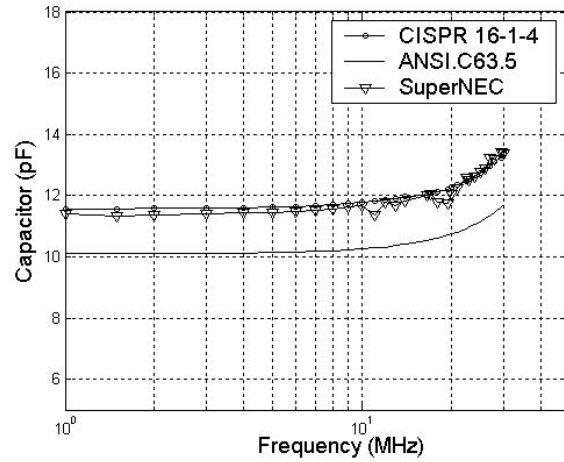


Fig. 3. Capacitance of dummy antenna (calculated - simulated).

It is observed that the capacitor value increases with the frequency. The results yield 2 dB uncertainty above 15 MHz. Another uncertainty comes from the variation of the effective length of the rod with the frequency.

ECISM is based on the insertion loss measurement of antenna matching network (AMN) with antenna simulator used instead of the actual rod. Using Manufacture Antenna Simulator (MAS) (Fig. 4) instead of dummy capacitor in order to make another effective check on the GTEM cell data. In addition, s-parameters of MAS circuit have been calculated using Microwave Office V. 2.66. A Network Analyzer was used to measure the related parameters. Measurement and calculation results were found to be very close (0.1 dB) (Fig. 5.) It has been understood that this circuit is very well matched at 50 ohm.

We measured insertion loss of the Antenna Matching Network (AMN) with MAS The resulting data gives the rod antenna factor.

In all measurements, traceable devices have been used and all cable attenuations have been taken into account.

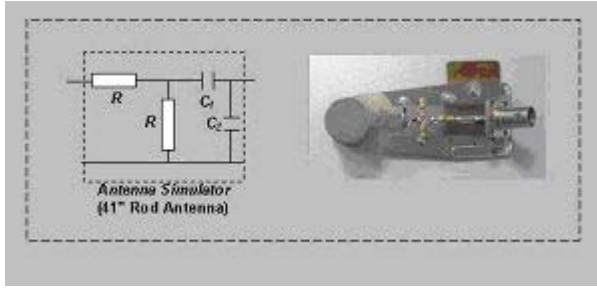


Fig. 4. Manufacture antenna simulator (MAS).

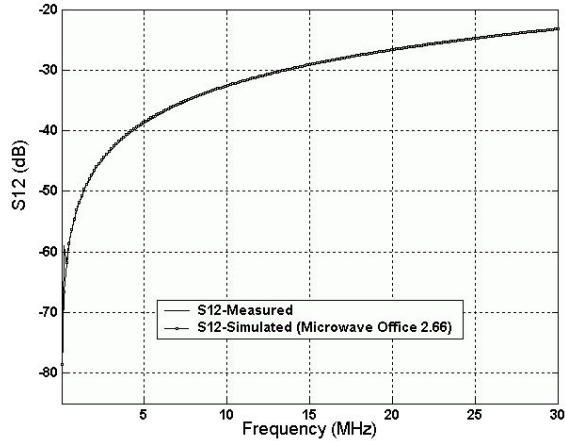


Fig. 5. S_{12} of MAS.

In order to make better comparison of the results, and also to check the general curve of AMN response we have obtained the insertion loss (IL) curve of the AMN and then calculated antenna factor by adding contribution of effective length of the rod .

Antenna factors of Rod#1 and Rod#2 are obtained by using AF-ECSM, AF-ECISM (Equivalent Circuit Substitution Method), AF-IL (Insertion Loss of AMN) and AF-GTEM (measured and calculated).

It has been observed that antenna factor values obtained using GTEM and ECISM methods were very close in the frequency range 10 kHz – 25 MHz (Fig. 6 and Fig. 7). However, it has been also observed that results obtained using these methods are approximately 2 dB different from the ECSM and IL results (2.6 dB above 25 MHz). The difference between GTEM calculated and GTEM measured data may come from the raised location of feed point on the floor of GTEM and the tilt angle. In high frequency range (above 25 MHz), IL curve of antenna matching circuit is similar in GTEM and ECISM methods. The difference between GTEM and ECSM may come from the instability of the 10-pF capacitance (it should be 12.5 pF as given in Fig. 3) values through the frequency range, the high production tolerance of the capacitor and effective length of the antenna. Small changes on the effective length of the antenna may result large error to the antenna factor. For example the 5cm change is gives approximately 1 dB error.

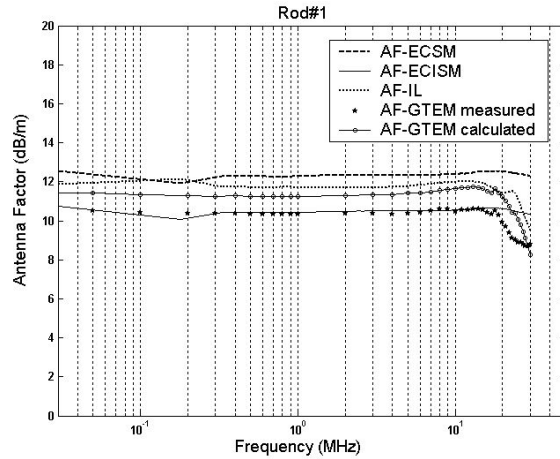


Fig. 6. Antenna factor (Rod#1).

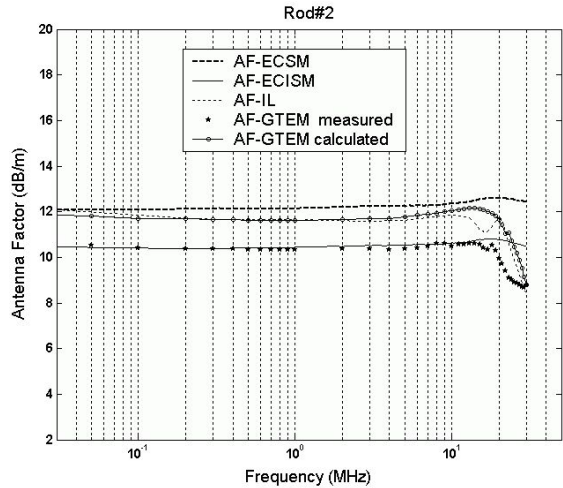


Fig. 7. Antenna factor (Rod#2).

III. FEASIBILITY CONSIDERATIONS AND UNCERTAINTIES

The obvious error sources in GTEM cell are reflections from the termination section. Since the antenna is placed in the testing volume it will receive signal directly from the port of the cell and another signal from termination section where there is reflection with a power reflection coefficient of typically -25 dB for the TEM mode. Another source of error is higher order GTEM wave-guide modes, which cause unwanted field fluctuations in the test volume inside GTEM cell [10]. This error can be cancelled at the low frequency measurements.

We present the uncertainty of antenna calibrations in the frame of the conventional uncertainty estimation where partial derivatives of the fundamental formula constitute the basis of uncertainty budget [11]. Parameters acting in this budget are impedance discontinuity (antenna-cable, GTEM cable), signal generator/EMC analyzer specifications, cable attenuation, direction coupler and repeatability. The overall expanded

uncertainty is calculated to be ± 1.01 dB in the frame of these parameters. The uncertainty of GTEM 1750 field uniformity has not been added in the uncertainty budget.

IV. CONCLUSIONS

- Two identical monopole antennas covering the frequency range 10 kHz-30 MHz were calibrated by using GTEM cell and ECISM.
- Good agreement between the GTEM and ECISM was observed.
- Capacitance and effective length of the dummy antenna varies with frequency. This variation brings an additional 2 dB uncertainty above 10 MHz. This uncertainty does not include the tolerance of 10-pF capacitor.
- Antenna is an element that converts electric field to voltage and AF identifies the rate of this conversion. In GTEM calibration AF is determined by making measurements, hence precluding uncertainties arising from dummy antenna. Note that capacitor used instead of the antenna in ECISM method cannot fully simulate the antenna.
- If the separation distance is not large enough in NIST method, the incident field is not constant along the length of the AUT, this introduces the non-planarity error in the determination of the antenna factor. And NIST calibration method gives free space antenna factor of monopole antenna. Practically monopole antennas are used in EMC compliance measurements, in which there is a 1-meter distance (especially for Military Standards) from EUT (Equipment Under Test). It is well-known free space antenna factor and 1m-antenna factor are different at each other so we suggest the GTEM results to be used reliably for 1m EMC measurements.
- In the previous works, GTEM cell has been used for antenna calibration in the frequency range 300 MHz to higher frequency [2,3] This works shows to assure the suitability of the GTEM for antenna calibration in the lower frequency range.
- Additional work is performed to determine transmit antenna factor of the passive rod antenna, using the reciprocity property of the GTEM.

REFERENCES

- [1] ANSI C63.5 American National Standard for Electromagnetic Compatibility-Radiated Emission Measurements in Electromagnetic Interference (EMI) Control-Calibration of Antennas (9 kHz-40 GHz), *The Institute of Electrical and Electronics Engineers, Inc*, New York, USA, 1998.
- [2] Branaugh E.L., Osburn J.D.M., "Measuring EMC Antenna Factors in The GHz Transverse Electromagnetic Cell," *IEEE Symposium Records*, pp.229-231, Anaheim, California, USA, 1992.
- [3] Türetken B., Yürekli A.İ., and M.Yazici, "Determining Antenna Factors for EMC Measurements," *Turkish Journal of Telecommunication*, vol. 1, no. 2, pp.59-66, 2002.
- [4] SAE ARP 958, Electromagnetic Interference Measurement Antennas, Standard Calibration

Requirements and Methods, Society of Automotive Engineers (SAE), 1999.

- [5] CISPR 16-1-4: Specification for radio disturbance and immunity measuring apparatus and methods, Edition 1.1. 2004-05, IEC, 2004.
- [6] MIL-STD 461 E, Requirement for the Control of Electromagnetic Interference Characteristics of Subsystems and Equipment, Department of Defence, USA, 1999.
- [7] Alexander M.J., "Calibration and Use of EMC Antennas," NPL, April 1977.
- [8] Randa J., "Correction Factor for Nonplanar Incident Field in Monopole Calibrations" *IEEE Transactions on Electromagnetic Compatibility*, vol. 35, no. 1, 1993.
- [9] Hui P., "Small Antenna Measurements Using a GTEM Cell" *IEEE Antennas and Propagation Society International Symposium*, vol. 4, pp. 715 - 718, pp. 22-27, June 2003.
- [10] Icheln C., Vainikainen P., and Haapala P., "Application of GTEM Cell to Small Antenna Measurements," *Antennas and Propagation Society* vol.1, pp. 546 - 549, pp. 13-18, July 1997.
- [11] Foegelle M.D., "A statistical Approach to Measurement Uncertainty," *Antenna Catalog Essential Equipment for EMC Testing- EMCO*, 1998.



Bahattin Türetken was born in Erzurum, in 1974. He has received B.Sc. from Yildiz Technical University in 1995. He received M.Sc. and PhD. degrees from Istanbul Technical University, Istanbul, Turkey in 1998 and 2002 respectively.

He has been working as a senior researcher at TUBITAK-UEKAE (National Research Institute of Electronics and Cryptology) EMC & TEMPEST Test Center. He was awarded "Young Scientist Award" by URSI in 1999. He has been involved in civilian and military EMC testing, Computational Electromagnetics, Diffraction & Scattering EM Problems, Antenna Design and Application, Wiener-Hopf Technique.

A Second-Order Symplectic Partitioned Runge-Kutta Scheme for Maxwell's Equations

Huang Zhi-Xiang and Wu Xian-Liang
 Key Lab of Intelligent Computing & Signal Processing,
 Anhui University, Ministry of Education
 Hefei 230039, China

Abstract: In this paper, we construct a new scheme for approximating the solution to infinite dimensional non-separable Hamiltonian systems of Maxwell's equations using the symplectic partitioned Runge-Kutta (PRK) method. The scheme is obtained by discretizing the Maxwell's equations in the time direction based on symplectic PRK method, and then evaluating the equation in the spatial direction with a suitable finite difference approximation. The scheme preserves the symplectic structure in the time direction and shows substantial benefits in numerical computation for Hamiltonian system, especially in long-term simulations. Also several numerical examples are presented to verify the efficiency of the scheme.

I. INTRODUCTION

Symplectic schemes include a variety of different time discretization schemes designed to preserve the global symplectic structure of the phase space for a Hamiltonian system. They show substantial benefits in numerical computation for Hamiltonian system, especially in long-term simulations. Since the Maxwell's equations can be written as a system of infinite-dimensional Hamiltonian equations, the proper solution should be obtained using the symplectic schemes, which preserve the symplectic structure in the time direction. The conservation of symplecticness must be considered for solving Maxwell's equations. Recently, the symplectic schemes have been adapted in computational electromagnetic (CEM). The advantages of the symplectic schemes have been verified in [1]-[6]. These schemes are almost constructed under the assumption that the Hamiltonian system of Maxwell's equations is separable [1,4,6]. In fact, when the scattering objects are presented the corresponding Hamiltonian system is non-separable [7]. Thus the assumption limits the application of the symplectic in the area of CEM.

In this paper, we will explore the application of the symplectic scheme for non-separable Hamiltonian system of Maxwell's equations, i.e. the scattering object is presented, using a symplectic PRK scheme [7-8] for the first time. For convenience we will discuss details of the scheme only for second-order explicit method,

however, the high order explicit scheme could be obtained using similar symplectic PRK scheme for infinite dimensional non-separable Hamiltonian system of Maxwell's Equations. We will also present several numerical examples to confirm the accuracy of our scheme.

II. HAMILTONION SYSTEM AND SYMPLECTICSCHEMES

Maxwell's Equations as Hamiltonian System

Within linear isotropic material, the basic equations can be written as

$$\frac{\partial \mathbf{B}}{\partial t} = -\nabla \times \mathbf{E} \tag{1}$$

$$\frac{\partial \mathbf{E}}{\partial t} = \frac{1}{\mu\epsilon} \nabla \times \mathbf{B} - \frac{1}{\epsilon} \mathbf{J} \tag{2}$$

where \mathbf{B} , \mathbf{E} , \mathbf{J} and μ , ϵ are magnetic flux density, electric flux density, current density and permeability, permittivity, respectively. In this paper, μ and ϵ are assumed to be constant.

Under the Hamiltonian framework, (1) and (2) can be rewritten in a form of an infinite dimensional Hamiltonian system. By introducing two temporary variables \mathbf{Y} and \mathbf{A} such that

$$\mathbf{Y} = -\mathbf{E} \tag{3}$$

$$\mathbf{B} = \nabla \times \mathbf{A} \tag{4}$$

We now can write Maxwell's Equations with (3) and (4) into the following infinite dimensional Hamiltonian system

$$\frac{\partial \mathbf{A}}{\partial t} = \frac{\partial \mathbf{H}}{\partial \mathbf{Y}} \tag{5}$$

$$\frac{\partial \mathbf{Y}}{\partial t} = -\frac{\partial \mathbf{H}}{\partial \mathbf{A}} \tag{6}$$

where \mathbf{H} is a Hamiltonian energy function given by

$$\mathbf{H}(\mathbf{A}, \mathbf{Y}) = \int \left(\frac{1}{2} |\mathbf{Y}|^2 + \frac{1}{2\mu\epsilon} |\nabla \times \mathbf{A}|^2 - \frac{1}{\epsilon} \mathbf{J} \cdot \mathbf{A} \right) dV \tag{7}$$

For simplicity we will focus our discussion on the Maxwell's equations in two-dimensional (2-D) TM case, where \mathbf{A} and \mathbf{Y} denote the z -component of the vector potential and the electric displacement, respectively [9]. Thus combined with eqn. (7), eqn. (5) and eqn. (6) can be rewritten as follows

$$\frac{\partial A_z}{\partial t} = Y_z \quad (8)$$

$$\frac{\partial Y_z}{\partial t} = \frac{\nabla^2 A_z}{\mu\epsilon} + \frac{J_z}{\epsilon} \quad (9)$$

field components are derived from A_z and Y_z as follows:

$$E_z = -Y_z \quad (10)$$

$$H_x = \frac{1}{\mu} \frac{\partial A_z}{\partial y} \quad (11)$$

$$H_y = -\frac{1}{\mu} \frac{\partial A_z}{\partial x} \quad (12)$$

Symplectic Schemes for Hamiltonian System

Here we assume that all Hamiltonian systems considered are autonomous, i.e. they are time-independent. As for time-dependent the schemes are similar [6].

Often the case that J_z acts as independent sources of \mathbf{E} -field, i.e. $J_z = J_{source}$, the corresponding Hamiltonian system (7) is called separable [1,7]. There exists little difficulty in solving eqn. (8) and eqn. (9) using explicit symplectic schemes [10–11].

When allowing for general cases where materials with electric losses that attenuate \mathbf{E} -field, this yields:

$$J_z = J_{source} + \sigma E_z \quad (13)$$

where σ is the electric conductivity. The Hamiltonian system (7) is non-separable, how to handle this situation, to the authors knowledge, has not given rise to a thoroughly answer up to now. Fortunately, in this case we can also obtain high order explicit symplectic schemes for eqn. (8) and eqn. (9) with composite symplectic partitioned Runge-Kutta (PRK) method [7–8].

In this paper particular, we only consider the 2-stag symplectic PRK Lobatto III A- III B method of second-order with the temporal error of $O(dt^3)$ (see [7]). When applied in eqn. (8) and eqn. (9) with $J_z = \sigma E_z$, the scheme has the following forms,

$$A_z^1(i, j) = A_z^n(i, j) + \frac{dt}{2} Y_z^n(i, j) \quad (14)$$

$$Y_z^{n+1}(i, j) = \frac{2\epsilon - dt\sigma}{2\epsilon + dt\sigma} Y_z^n(i, j) + \frac{2\epsilon dt}{\mu\epsilon \cdot (2\epsilon + dt\sigma)} L[A_z^1(i, j)] \quad (15)$$

$$A_z^{n+1}(i, j) = A_z^1(i, j) + \frac{dt}{2} Y_z^{n+1}(i, j) \quad (16)$$

where $A_z^n(i, j)$ and $Y_z^n(i, j)$ are respectively for the discrete value of A_z and Y_z at mesh point (i, j) and the n -th time step, $A_z^1(i, j)$ are the intermediate value, dt is the time increment, L is a difference operator approximating the ∇^2 operator and it allows flexibility during the selection of the spatial discretizations. Here we select the most commonly used central discretizations to approximate ∇^2 operator in our examples. Given appropriate absorbing boundary conditions (ABC) in computation domain, we can solve Maxwell's equations using the symplectic PRK scheme.

III. NUMERICAL RESULTS

A TEM wave propagation in one dimension

We first consider a one-dimensional TEM wave propagation problem within a finite domain $[0, 2\pi]$ along the x -axis. We discretize the problem using a uniform grid with $N = 200$ subintervals and choose the time step $dt = 0.1dx$. We set both μ and ϵ be one and take $E_y(x, 0) = \cos x$, $H_z(x, 0) = \cos x$ as the initial conditions. In addition, the boundary conditions are the periodic boundary conditions. Compared with exact solution and the second-order symplectic PRK scheme (S-PRK2o), the x -axis variation of the electric flux density E_y at 10,000 and 15,000 time steps is displayed in figure 1. The electric flux density profile propagates without any changes in the profile. The results clearly show that the present scheme is pretty good for long-term simulations.

Wave propagation in two dimensions

Next we consider a two-dimensional TM case involving a sinusoidal source of frequency 30GHz. The source is generated in the middle of the problem domain. We use Mur's ABC [12] to truncate the computational domain $[0, 1] \times [0, 1]$. We also discretized the problem on the domain with $N_x = N_y = 100$ grid points in each direction and with $dt = \frac{dx}{2\sqrt{\mu\epsilon}}$. Figure

2 demonstrates a simulation for the electric flux density

E_z after the 5,000 time steps. As comparison, we simulate the problem using standard FDTD under the same conditions. The results show the efficiency of the present scheme.

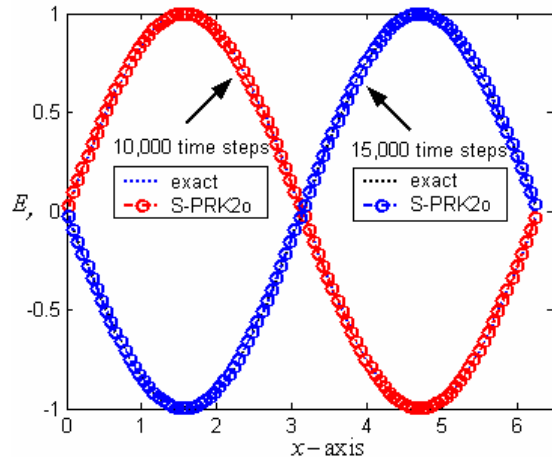
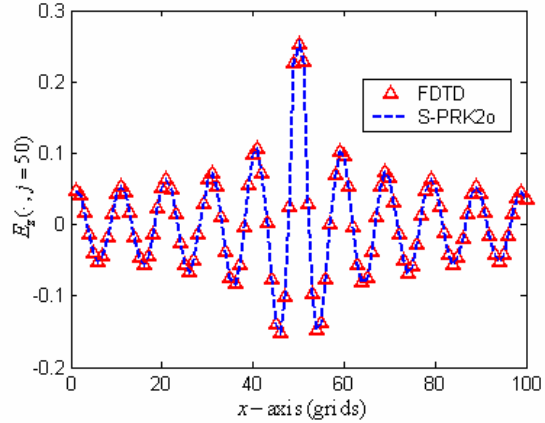
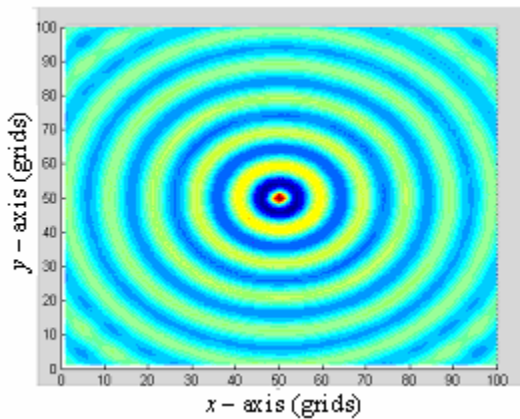


Fig. 1. Comparison of E_y calculated by S-PRK2o and exact solution after 10,000 and 15,000 time steps.

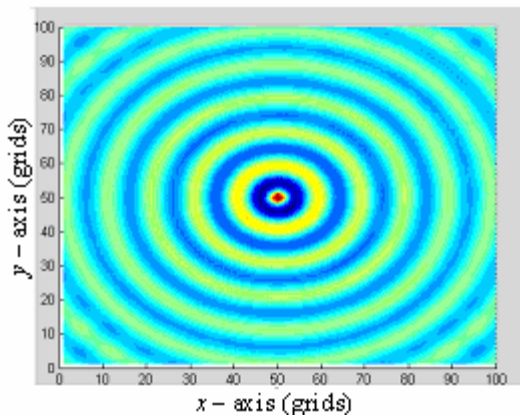


(c) The electric flux density E_z at grid $j = 50$

Fig. 2. The drawings of electric flux density E_z after 5,000 time steps. The source is sinusoidal source and generated in the middle of the problem domain. The absorbing boundary conditions are the Mur's ABC. (a), (b) The phase of E_z in the x - y plane. (c) The amplitude of E_z at y -grid $j = 50$.



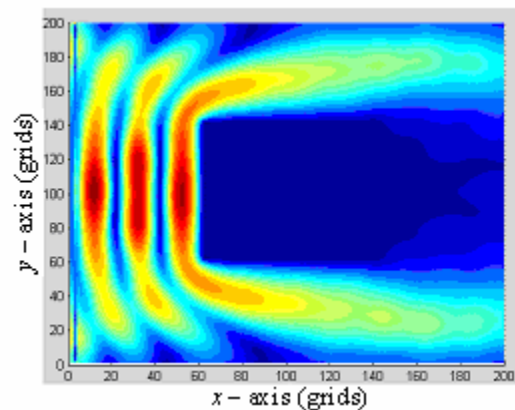
(a) Symplectic PRK scheme (S-PRK2o)



(b) Standard FDTD

Plane wave impinging on a infinite square cylinder

In this example, we consider the scattering of a plane wave impinging on a infinite square cylinder with side length $a = 2\lambda$ ($\lambda = 1 \times 10^{-2} m$), where λ is wavelength. The incident plane wave is a TM case and propagates from the left. We discretize the problem on the domain with $N_x = N_y = 100$ grid points in each direction and with $dx = dy = \lambda/40$, $dt = dx/2(\mu\epsilon)^{1/2}$ independently. Here we also use Mur's ABC to truncate the computational domain. The numerical solution after 1,000 time steps using present scheme and the standard FDTD method under the same conditions are presented in Fig. 3. Figure 3 (a) and (b) demonstrate the distributions of the electric flux density E_z after the



(a) Symplectic PRK scheme (S-PRK2o)

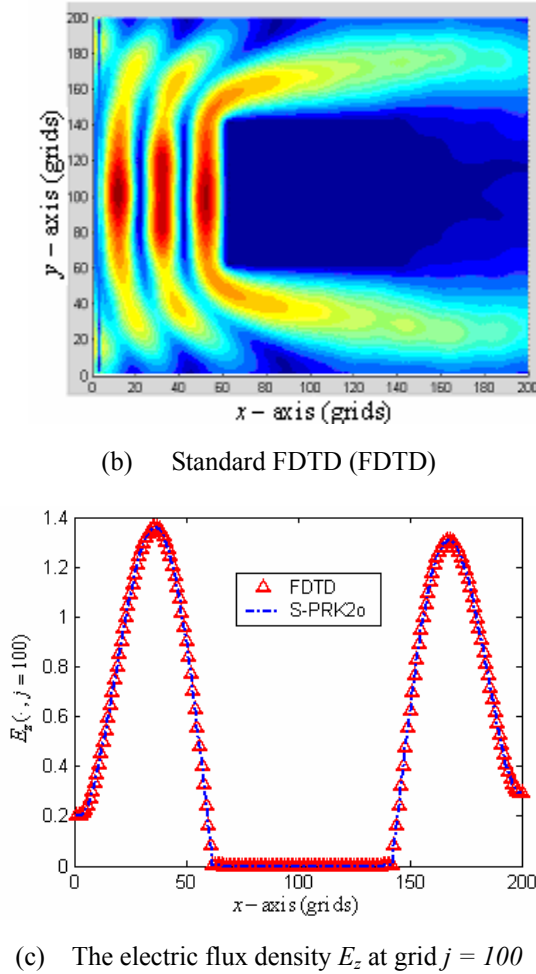


Fig. 3. The distributions of the electric flux density E_z after the 1,000 time steps. The incident plane wave is a TM case and propagates from the left. The absorbing boundary conditions are the Mur's ABC. (a), (b) The amplitude of the E_z in the x - y plane. (c) The amplitude of E_z at y -grid $j = 100$.

1,000 time steps. Figure 3 (c) shows the electric flux density E_z at point $j = 100$ grid. The results indicate that the performance of symplectic PRK scheme (S-PRK2o) are as at least efficient as the standard FDTD.

IV. CONCLUSION

We construct and present a symplectic PRK scheme (S-PRK2o) for the non-separable Hamiltonian system of Maxwell's Equations. The scheme is second-order explicit and has the temporal error of $O(dt^3)$. Our numerical examples demonstrate that the scheme is very effective in computing different types of wave

propagations and scattering for the Maxwell's Equations.

Although the scheme is second-order explicit method, the high order explicit scheme could be obtained using similar symplectic PRK scheme for non-separable Hamiltonian system of Maxwell's Equations. Our numerical tests are running on the regular domain using square mesh, but the scheme could be adopted to compute the problem on any irregular domain.

ACKNOWLEDGEMENTS

This work was partially supported by the China "The national natural science foundation of China (No.6037104)".

REFERENCES

- [1] T. Hirono, W. W. Lui, and K. Yokoyama, "Time-domain simulation of electromagnetic field using a symplectic integrator," *IEEE Microwave Guided Wave Lett.*, vol. 7, pp. 279–281, Sept. 1997.
- [2] T. Hirono, W. W. Lui, K. Yokoyama, and S. Seki, "Stability and dispersion of the symplectic fourth-order time-domain schemes for optical field simulation," *J. Lightwave Technol.*, vol. 16, pp. 1915–1920, Oct. 1998.
- [3] T. Hirono, W. Lui, S. Seki, and Y. Yoshikuni, "A three-dimensional fourth-order finite-difference time-domain scheme using a symplectic integrator propagator," *IEEE Trans. Microwave Theory Tech.*, vol. 49, pp. 1640–1647, Sept. 2001.
- [4] I. Saitoh, Y. Suzuki, and N. Takahashi, "The symplectic finite difference time domain method," *IEEE Trans. Magn.*, vol. 37, pp. 3251–3254, Sept. 2001.
- [5] I. Saitoh and N. Takahashi, "Stability of symplectic finite-difference time-domain methods," *IEEE Trans. Magn.*, vol. 38, pp. 665–668, Mar. 2002.
- [6] R. Rieben, D. White, and G. Rodrigue, "High-order symplectic integration methods for finite element solutions to time dependent Maxwell equations," *IEEE Trans. Antennas Propagat.*, vol. 52, no. 8, pp. 2190–2195, Aug. 2004.

- [7] S. Geng, "Construction of high order Symplectic PRK methods," J.Comput, Math, vol. 13, no.1, pp. 40-50, 1995.
- [8] S. Geng, "Symplectic partitioned Runge-Kutta method," J.Comput, Math., vol. 11, no. 4, pp. 365-372, 1993.
- [9] L.I. Schiff, Quantum Mechanics. London, U.K., McGraw-Hill, 1968,ch.14.
- [10] R.D. Ruth, "A canonical integration technique," IEEE Trans. Nucl. Science, vol. NS-30, pp. 2669-2671, Aug. 1983.
- [11] E. Forest and R.D.Ruth, "Four-order symplectic integration," Physica D., vol. 43, pp. 105-117, 1990.
- [12] G. Mur, "Absorbing boundary conditions for the finite-difference approximation of the time-domain electromagnetic field equations." IEEE Trans. Electromagn. Compt., EMC-23 (4), pp. 377-382, Nov. 1981.



Huang Zhi-Xiang was born in Anhui, China, on December 23, 1979. He is currently pursuing a Ph.D. degree in Anhui University. His research interests include high frequency method and symplectic scheme for time domain electromagnetics.



Wu Xian-Liang was born in 1958. He is currently a professor of Anhui University, doctor supervisor. His research interests include signal processing, target tracking and numerical method for electromagnetics.

2005 INSTITUTIONAL MEMBERS

AUSTRALIAN DEFENCE LIBRARY
Northcott Drive
Campbell, A.C.T. 2600 AUSTRALIA

BEIJING BOOK COMPANY, INC
701 E Lindon Ave.
Linden, NJ 07036-2495

BRITISH LIBRARY
Boston SPA, Wetherby
West Yorkshire, UK LS23 7BQ

DARMSTADT U. OF TECHNOLOGY
Schlossgartenstrasse 8
Darmstadt, Hessen
GERMANY D-64289

DARTMOUTH COLL-FELDBERG LIB
6193 Murdough Center
Hanover, NH 03755-3560

DEFENCE RESEARCH ESTAB. LIB.
3701 Carling Avenue
Ottawa, ON, K1A 0Z4 CANADA

DLR-STANDORTBIBLIOTEK
Muenchnerstrasse 20
Wessling, Germany 82234

DPS/LIBRARY (EABV)
Alion Science & Technology
185 Admiral Cochrane Drive
Annapolis, MD 214017307

DSTO-DSTORL EDINBURGH
Jets AU/33851-99, PO Box 562
Milsons Point, NSW
AUSTRALIA 1565

DTIC-OCP/LIBRARY
8725 John J. Kingman Rd. Ste 0944
Ft. Belvoir, VA 22060-6218

ELLEDIEMME SRL
Via Baccina 30
Roma, Italy 00184

ELSEVIER
Bibliographic Databases
PO Box 2227
Amsterdam, Netherlands 1000 CE

ENGINEERING INFORMATION, INC
PO Box 543
Amsterdam, Netherlands 1000 Am

ETSE TELECOMUNICACION
Biblioteca, Campus Lagoas
Vigo, 36200 SPAIN

FGAN-FHR
Neuenahrerstrasse 20
Wachtberg, Germany 53343

FLORIDA INTERNATIONAL UNIV.
ECE Dept./EAS-3983
10555 W. Flagler St
Miami, FL 33174

GEORGIA TECH LIBRARY
225 North Avenue, NW
Atlanta, GA 30332-0001

HRL LABS, RESEARCH LIBRARY
3011 Malibu Canyon
Malibu, CA 90265

IEE INSPEC/Acquisitions Section
Michael Faraday House
6 Hills Way
Stevenage, Herts UK SG1 2AY

IND CANTABRIA
PO Box 830470
Birmingham, AL 35283

INSTITUTE FOR SCIENTIFIC INFO.
Publication Processing Dept.
3501 Market St.
Philadelphia, PA 19104-3302

LIBRARY OF CONGRESS
Reg. Of Copyrights
Attn: 40T Deposits
Washington DC, 20559

LINDA HALL LIBRARY
5109 Cherry Street
Kansas City, MO 64110-2498

MISSISSIPPI STATE UNIV LIBRARY
PO Box 9570
Mississippi State, MS 39762

MIT LINCOLN LABORATORY
Periodicals Library
244 Wood Street
Lexington, MA 02420

NA KANSAI KINOKUNNA CO.
Attn: M. MIYOSHI
PO Box 36 (NDLA KANSAI)
Hongo, Tokyo, JAPAN 113-8688

NATL. CTR. FOR HIGH-
PERFORMANCE COMPUTING LIB.
PO Box 117-00930
Taipei City, Taiwan (ROC) 10699

NATL. GROUND INTELL. CENTER
2055 Boulders Road
Charlottesville, VA 22911-8318

NAVAL POSTGRADUATE SCHOOL
Attn: J. Rozdal/411 Dyer Rd./ Rm 111
Monterey, CA 93943-5101

NAVAL RESEARCH LABORATORY
C. Office, 4555 Overlook Avenue, SW
Washington, DC 20375

OHIO STATE UNIVERSITY
1320 Kinnear Road
Columbus, OH 43212

OVIEDO LIBRARY
PO BOX 830679
Birmingham, AL 35283

PAIKNAM ACAD. INFO CTR LIB.
Hanyang U/17 Haengdang-Dong
Seongdong-ki, Seoul, S Korea 133-
791

PENN STATE UNIVERSITY
126 Paterno Library
University Park, PA 16802-1808

PHILIPS RESEARCH LAB
Cross Oak Lane, Stella Cox, Salfords
Red Hill, UK RH1 5HA

RENTON TECH LIBRARY/BOEING
PO BOX 3707
SEATTLE, WA 98124-2207

SOUTHWEST RESEARCH INST.
6220 Culebra Road
San Antonio, TX 78238

SWEDISH DEFENCE RES.
AGENCY (FOI)
PO Box 1165
Linkoping, Sweden S-58111

SWETS INFORMATION SERVICES
160 Ninth Avenue, Suite A
Runnemede, NJ 08078

SYRACUSE UNIVERSITY
EECS, 121 Link Hall
Syracuse, NY 13244

TECHNISCHE UNIV. DELFT
Mekelweg 4, Delft, Holland, 2628 CD
NETHERLANDS

TIB & UNIV. BIB. HANNOVER
DE/5100/G1/0001
Welfengarten 1B
Hannover, GERMANY 30167

TOKYO KOKA UNIVERSITY
1404-1 Katakura-Cho
Hachioji, Tokyo, JAPAN 192-0914

UNIV OF CENTRAL FLORIDA LIB.
4000 Central Florida Boulevard
Orlando, FL 32816-8005

UNIV OF COLORADO LIBRARY
Campus Box 184
Boulder, CO 80309-0184

UNIVERSITY OF MISSISSIPPI
John Davis Williams Library
PO Box 1848
University, MS 38677-1848

UNIV OF MISSOURI-ROLLA LIB.
1870 Miner Circle
Rolla, MO 65409-0001

USAE ENG. RES. & DEV. CENTER
Attn: Library/Journals
72 Lyme Road
Hanover, NH 03755-1290

USP POLI
Av: Elmira Martins Moreira, 455
Jacarei, Sao Paulo, Brazil 12306-730

ACES COPYRIGHT FORM

This form is intended for original, previously unpublished manuscripts submitted to ACES periodicals and conference publications. The signed form, appropriately completed, MUST ACCOMPANY any paper in order to be published by ACES. PLEASE READ REVERSE SIDE OF THIS FORM FOR FURTHER DETAILS.

TITLE OF PAPER:

RETURN FORM TO:

Dr. Atef Z. Elsherbeni
University of Mississippi
Dept. of Electrical Engineering
Anderson Hall Box 13
University, MS 38677 USA

AUTHORS(S)

PUBLICATION TITLE/DATE:

PART A - COPYRIGHT TRANSFER FORM

(NOTE: Company or other forms may not be substituted for this form. U.S. Government employees whose work is not subject to copyright may so certify by signing Part B below. Authors whose work is subject to Crown Copyright may sign Part C overleaf).

The undersigned, desiring to publish the above paper in a publication of ACES, hereby transfer their copyrights in the above paper to The Applied Computational Electromagnetics Society (ACES). The undersigned hereby represents and warrants that the paper is original and that he/she is the author of the paper or otherwise has the power and authority to make and execute this assignment.

Returned Rights: In return for these rights, ACES hereby grants to the above authors, and the employers for whom the work was performed, royalty-free permission to:

1. Retain all proprietary rights other than copyright, such as patent rights.
2. Reuse all or portions of the above paper in other works.

3. Reproduce, or have reproduced, the above paper for the author's personal use or for internal company use provided that (a) the source and ACES copyright are indicated, (b) the copies are not used in a way that implies ACES endorsement of a product or service of an employer, and (c) the copies per se are not offered for sale.

4. Make limited distribution of all or portions of the above paper prior to publication.

5. In the case of work performed under U.S. Government contract, ACES grants the U.S. Government royalty-free permission to reproduce all or portions of the above paper, and to authorize others to do so, for U.S. Government purposes only.

ACES Obligations: In exercising its rights under copyright, ACES will make all reasonable efforts to act in the interests of the authors and employers as well as in its own interest. In particular, ACES REQUIRES that:

1. The consent of the first-named author be sought as a condition in granting re-publication permission to others.
2. The consent of the undersigned employer be obtained as a condition in granting permission to others to reuse all or portions of the paper for promotion or marketing purposes.

In the event the above paper is not accepted and published by ACES or is withdrawn by the author(s) before acceptance by ACES, this agreement becomes null and void.

AUTHORIZED SIGNATURE

TITLE (IF NOT AUTHOR)

EMPLOYER FOR WHOM WORK WAS PERFORMED

DATE FORM SIGNED

Part B - U.S. GOVERNMENT EMPLOYEE CERTIFICATION

(NOTE: if your work was performed under Government contract but you are not a Government employee, sign transfer form above and see item 5 under Returned Rights).

This certifies that all authors of the above paper are employees of the U.S. Government and performed this work as part of their employment and that the paper is therefor not subject to U.S. copyright protection.

AUTHORIZED SIGNATURE

TITLE (IF NOT AUTHOR)

NAME OF GOVERNMENT ORGANIZATION

DATE FORM SIGNED

PART C - CROWN COPYRIGHT

(NOTE: ACES recognizes and will honor Crown Copyright as it does U.S. Copyright. It is understood that, in asserting Crown Copyright, ACES in no way diminishes its rights as publisher. Sign only if ALL authors are subject to Crown Copyright).

This certifies that all authors of the above Paper are subject to Crown Copyright. (Appropriate documentation and instructions regarding form of Crown Copyright notice may be attached).

AUTHORIZED SIGNATURE

TITLE OF SIGNEE

NAME OF GOVERNMENT BRANCH

DATE FORM SIGNED

Information to Authors

ACES POLICY

ACES distributes its technical publications throughout the world, and it may be necessary to translate and abstract its publications, and articles contained therein, for inclusion in various compendiums and similar publications, etc. When an article is submitted for publication by ACES, acceptance of the article implies that ACES has the rights to do all of the things it normally does with such an article.

In connection with its publishing activities, it is the policy of ACES to own the copyrights in its technical publications, and to the contributions contained therein, in order to protect the interests of ACES, its authors and their employers, and at the same time to facilitate the appropriate re-use of this material by others.

The new United States copyright law requires that the transfer of copyrights in each contribution from the author to ACES be confirmed in writing. It is therefore necessary that you execute either Part A-Copyright Transfer Form or Part B-U.S. Government Employee Certification or Part C-Crown Copyright on this sheet and return it to the Managing Editor (or person who supplied this sheet) as promptly as possible.

CLEARANCE OF PAPERS

ACES must of necessity assume that materials presented at its meetings or submitted to its publications is properly available for general dissemination to the audiences these activities are organized to serve. It is the responsibility of the authors, not ACES, to determine whether disclosure of their material requires the prior consent of other parties and if so, to obtain it. Furthermore, ACES must assume that, if an author uses within his/her article previously published and/or copyrighted material that permission has been obtained for such use and that any required credit lines, copyright notices, etc. are duly noted.

AUTHOR/COMPANY RIGHTS

If you are employed and you prepared your paper as a part of your job, the rights to your paper initially rest with your employer. In that case, when you sign the copyright form, we assume you are authorized to do so by your employer and that your employer has consented to all of the terms and conditions of this form. If not, it should be signed by someone so authorized.

NOTE RE RETURNED RIGHTS: Just as ACES now requires a signed copyright transfer form in order to do "business as usual", it is the intent of this form to return rights to the author and employer so that they too may do "business as usual". If further clarification is required, please contact: The Managing Editor, R. W. Adler, Naval Postgraduate School, Code EC/AB, Monterey, CA, 93943, USA (408)656-2352.

Please note that, although authors are permitted to re-use all or portions of their ACES copyrighted material in other works, this does not include granting third party requests for reprinting, republishing, or other types of re-use.

JOINT AUTHORSHIP

For jointly authored papers, only one signature is required, but we assume all authors have been advised and have consented to the terms of this form.

U.S. GOVERNMENT EMPLOYEES

Authors who are U.S. Government employees are not required to sign the Copyright Transfer Form (Part A), but any co-authors outside the Government are.

Part B of the form is to be used instead of Part A only if all authors are U.S. Government employees and prepared the paper as part of their job.

NOTE RE GOVERNMENT CONTRACT WORK: Authors whose work was performed under a U.S. Government contract but who are not Government employees are required so sign Part A-Copyright Transfer Form. However, item 5 of the form returns reproduction rights to the U. S. Government when required, even though ACES copyright policy is in effect with respect to the reuse of material by the general public.

January 2002

INFORMATION FOR AUTHORS

PUBLICATION CRITERIA

Each paper is required to manifest some relation to applied computational electromagnetics. **Papers may address general issues in applied computational electromagnetics, or they may focus on specific applications, techniques, codes, or computational issues.** While the following list is not exhaustive, each paper will generally relate to at least one of these areas:

1. **Code validation.** This is done using internal checks or experimental, analytical or other computational data. Measured data of potential utility to code validation efforts will also be considered for publication.
2. **Code performance analysis.** This usually involves identification of numerical accuracy or other limitations, solution convergence, numerical and physical modeling error, and parameter tradeoffs. However, it is also permissible to address issues such as ease-of-use, set-up time, run time, special outputs, or other special features.
3. **Computational studies of basic physics.** This involves using a code, algorithm, or computational technique to simulate reality in such a way that better, or new physical insight or understanding, is achieved.
4. **New computational techniques,** or new applications for existing computational techniques or codes.
5. **“Tricks of the trade”** in selecting and applying codes and techniques.
6. **New codes, algorithms, code enhancement, and code fixes.** This category is self-explanatory, but includes significant changes to existing codes, such as applicability extensions, algorithm optimization, problem correction, limitation removal, or other performance improvement. **Note: Code (or algorithm) capability descriptions are not acceptable, unless they contain sufficient technical material to justify consideration.**
7. **Code input/output issues.** This normally involves innovations in input (such as input geometry standardization, automatic mesh generation, or computer-aided design) or in output (whether it be tabular, graphical, statistical, Fourier-transformed, or otherwise signal-processed). Material dealing with input/output database management, output interpretation, or other input/output issues will also be considered for publication.
8. **Computer hardware issues.** This is the category for analysis of hardware capabilities and limitations of various types of electromagnetics computational requirements. Vector and parallel computational techniques and implementation are of particular interest.

Applications of interest include, but are not limited to, antennas (and their electromagnetic environments), networks, static fields, radar cross section, shielding, radiation hazards, biological effects, electromagnetic pulse (EMP), electromagnetic interference (EMI), electromagnetic compatibility (EMC), power transmission, charge transport, dielectric, magnetic and nonlinear materials, microwave components, MEMS technology, MMIC technology, remote sensing and geometrical and physical optics, radar and communications systems, fiber optics, plasmas, particle accelerators, generators and motors, electromagnetic wave propagation, non-destructive evaluation, eddy currents, and inverse scattering.

Techniques of interest include frequency-domain and time-domain techniques, integral equation and differential equation techniques, diffraction theories, physical optics, moment methods, finite differences and finite element techniques, modal expansions, perturbation methods, and hybrid methods. This list is not exhaustive.

A unique feature of the Journal is the publication of unsuccessful efforts in applied computational electromagnetics. Publication of such material provides a means to discuss problem areas in electromagnetic modeling. Material representing an unsuccessful application or negative results in computational electromagnetics will be considered for publication only if a reasonable expectation of success (and a reasonable effort) are reflected. Moreover, such material must represent a problem area of potential interest to the ACES membership.

Where possible and appropriate, authors are required to provide statements of quantitative accuracy for measured and/or computed data. This issue is discussed in “Accuracy & Publication: Requiring quantitative accuracy statements to accompany data,” by E. K. Miller, *ACES Newsletter*, Vol. 9, No. 3, pp. 23-29, 1994, ISBN 1056-9170.

EDITORIAL REVIEW

In order to ensure an appropriate level of quality control, papers are peer reviewed. They are reviewed both for technical correctness and for adherence to the listed guidelines regarding information content.

JOURNAL CAMERA-READY SUBMISSION DATES

March issue	deadline 8 January
July issue	deadline 20 May
November issue	deadline 20 September

Uploading an acceptable camera-ready article after the deadlines will result in a delay in publishing this article.

STYLE FOR CAMERA-READY COPY

The ACES Journal is flexible, within reason, in regard to style. However, certain requirements are in effect:

1. The paper title should NOT be placed on a separate page. The title, author(s), abstract, and (space permitting) beginning of the paper itself should all be on the first page. The title, author(s), and author affiliations should be centered (center-justified) on the first page.
2. An abstract is REQUIRED. The abstract should be a brief summary of the work described in the paper. It should state the computer codes, computational techniques, and applications discussed in the paper (as applicable) and should otherwise be usable by technical abstracting and indexing services.
3. Either British English or American English spellings may be used, provided that each word is spelled consistently throughout the paper.
4. Any commonly-accepted format for referencing is permitted, provided that internal consistency of format is maintained. As a guideline for authors who have no other preference, we recommend that references be given by author(s) name and year in the body of the paper (with alphabetical listing of all references at the end of the paper). Titles of Journals, monographs, and similar publications should be in italic font or should be underlined. Titles of papers or articles should be in quotation marks.
5. Internal consistency shall also be maintained for other elements of style, such as equation numbering. As a guideline for authors who have no other preference, we suggest that equation numbers be placed in parentheses at the right column margin.
6. The intent and meaning of all text must be clear. For authors who are NOT masters of the English language, the ACES Editorial Staff will provide assistance with grammar (subject to clarity of intent and meaning).
7. Unused space should be minimized. Sections and subsections should not normally begin on a new page.

PAPER FORMAT

The preferred format for initial submission and camera-ready manuscripts is 12 point Times Roman font, single line spacing and double column format, similar to that used here, with top, bottom, left, and right 1 inch margins. Manuscripts should be prepared on standard 8.5x11 inch paper.

Only camera-ready electronic files are accepted for publication. The term “**camera-ready**” means that the material is neat, legible, and reproducible. Full details can be found on ACES site, Journal section.

ACES reserves the right to edit any uploaded material, however, this is not generally done. It is the author(s)

responsibility to provide acceptable camera-ready pdf files. Incompatible or incomplete pdf files will not be processed, and authors will be requested to re-upload a revised acceptable version.

SUBMITTAL PROCEDURE

All submissions should be uploaded to ACES server through ACES web site (<http://aces.ee.olemiss.edu>) by using the upload button, journal section. Only pdf files are accepted for submission. The file size should not be larger than 5MB, otherwise permission from the Editor-in-Chief should be obtained first. The Editor-in-Chief will acknowledge the electronic submission after the upload process is successfully completed.

COPYRIGHTS AND RELEASES

Each primary author must sign a copyright form and obtain a release from his/her organization vesting the copyright with ACES. Copyright forms are available at ACES, web site (<http://aces.ee.olemiss.edu>). To shorten the review process time, the executed copyright form should be forwarded to the Editor-in-Chief immediately after the completion of the upload (electronic submission) process. Both the author and his/her organization are allowed to use the copyrighted material freely for their own private purposes.

Permission is granted to quote short passages and reproduce figures and tables from and ACES Journal issue provided the source is cited. Copies of ACES Journal articles may be made in accordance with usage permitted by Sections 107 or 108 of the U.S. Copyright Law. This consent does not extend to other kinds of copying, such as for general distribution, for advertising or promotional purposes, for creating new collective works, or for resale. The reproduction of multiple copies and the use of articles or extracts for commercial purposes require the consent of the author and specific permission from ACES. Institutional members are allowed to copy any ACES Journal issue for their internal distribution only.

PUBLICATION CHARGES

ACES members are allowed 12 printed pages per paper without charge; non-members are allowed 8 printed pages per paper without charge. Mandatory page charges of \$75 a page apply to all pages in excess of 12 for members or 8 for non-members. Voluntary page charges are requested for the free (12 or 8) pages, but are NOT mandatory or required for publication. A priority courtesy guideline, which favors members, applies to paper backlogs. Authors are entitled to 15 free reprints of their articles and must request these from the Managing Editor. Additional reprints are available to authors, and reprints available to non-authors, for a nominal fee.

ACES Journal is abstracted in INSPEC, in Engineering Index, and in DTIC.